EXPERIMENTAL AND COMPUTATIONAL INVESTIGATION OF CRACK GROWTH ALONG CURVED INTERFACES

A THESIS SUBMITTED TO
THE GRADUATE SCHOOL OF NATURAL AND APPLIED SCIENCES
OF
MIDDLE EAST TECHNICAL UNIVERSITY

BY

DENİZHAN YAVAŞ

IN PARTIAL FULLFILLMENT OF THE REQUIREMENTS
FOR
THE DEGREE OF MASTER OF SCIENCE
IN
AEROSPACE ENGINEERING

JULY 2013

Approval of the thesis:

EXPERIMENTAL AND COMPUTATIONAL INVESTIGATION OF CRACK GROWTH ALONG CURVED INTERFACES

submitted by **DENİZHAN YAVAŞ** in partial fulfillment of the requirements for the degree of **Master of Science in Aerospace Engineering Department, Middle East Technical University** by,

Prof. Dr. Canan Özgen
Dean, Graduate School of **Natural and Applied Sciences** ________________

Prof. Dr. Ozan Tekinalp
Head of Department, **Aerospace Engineering** ________________

Assoc. Prof. Dr. Demirkan Çöker
Supervisor, **Aerospace Engineering Dept., METU** ________________

Examining Committee Members

Prof. Dr. Altan Kayran
Aerospace Engineering Department, METU ________________

Assoc. Prof. Dr. Demirkan Çöker
Aerospace Engineering Department, METU ________________

Prof. Dr. Levent Parnas
Mechanical Engineering Department, METU ________________

Assoc. Prof. Dr. Melin Şahin
Aerospace Engineering Department, METU ________________

Asst. Prof. Dr. Ercan Gürses
Aerospace Engineering Department, METU ________________

Date: 17.07.2013

I hereby declare that all information in this document has been obtained and presented in accordance with academic rules and ethical conduct. I also declare that, as required by these rules and conduct, I have fully cited and referenced all material and results that are not original to this work.

Name, Last name : Denizhan Yavaş
Signature :

ABSTRACT

EXPERIMENTAL AND COMPUTATIONAL INVESTIGATION OF CRACK GROWTH ALONG CURVED INTERFACES

Yavaş, Denizhan
M.S., Department of Aerospace Engineering
Supervisor: Assoc. Prof. Dr. Demirkan Çöker

July 2013, 83 pages

In this study, crack growth along curved weak interfaces is investigated experimentally and computationally. First, delamination of curved composite laminates subjected to axial load is studied computationally. Delamination in curved laminates is modeled using explicit finite element analysis in conjunction with cohesive zone method. It is observed that delamination is highly dynamic and that as the initial crack grows, the crack tip speed reaches the Rayleigh wave speed of the composite material with increasing laminate thickness and decreasing initial crack length. A second observation is that a secondary delamination in the arm region nucleates depending on the initial crack length and laminate thickness. Second, delamination of curved composite laminates subjected to shear loading is studied experimentally. Dynamic delamination growth is captured using high speed camera. It is observed that crack growth speed reachs the shear wave speed and an increase in the length of initial crack changes the crack growth from unstable to stable. Finally, crack growth along curved interface in polycarbonate beams subjected to shear loading is studied experimentally and computationally. In experiments, the full-field technique of photoelasticity is used in order to visualize isochromatic fringe pattern around the crack tip. In computational study, debonding at the curved interface is modeled using dynamic (explicit) finite element analysis in conjunction with cohesive zone methods. Stable and unstable crack growth regimes, depending on the initial crack length, are identified in agreement with energy release rate calculations. It is also observed that crack propagation speed can reach the shear wave speed.

Keywords : delamination, curved interfaces, interfacial crack, curved composite beams.

ÖZ

EĞİMLİ ARAYÜZLERDEKİ ÇATLAK İLERLEMESİNİN DENEYSEL VE SAYISAL İNCELENMESİ

Yavaş, Denizhan
Yüksek Lisans, Havacılık ve Uzay Mühendisliği Bölümü
Tez Yöneticisi: Doç. Dr. Demirkan Çöker

Haziran 2013, 83 sayfa

Bu çalışmada eğimli zayıf arayüzlerdeki çatlak ilerlemesi deneysel ve sayısal olarak incelenmiştir. İlk olarak, eğimli kompozit katmanlarında eksenel yükleme altında meydana gelen katmanların ayrılması sayısal olarak çalışılmıştır. Eğimli kompozit katmanlarda katmanların ayrılması yapışkan alan metodu ile birlikte açık sonlu elemanlar analizi kullanılarak modellenmiştir. Katman ayrılması ilerlemesinin yüksek derecede dinamik olduğu ve ilk ayrılmasının ilerlemesi ile çatlak ilerleme hızının katman kalınğının artması ve ilk çatlak uzunluğunun kısalmasıyla kompozit malzemedeki Rayleigh dalga hızına ulaştığı gözlenmiştir. İkinci gözlem ise ilk çatlak uzunluğuna ve katman kalınlığına bağlı olarak ikinci katman ayrılmasının kol bölgesinde gözlenmesidir. İkinci olarak, eğimli kompozit katmanlarda kesme yükü altında meydana gelen katman ayrılması deneysel olarak çalışılmıştır. Dinamik katman ayrılması ilerlemesi yüksek hızlı kamera kullanılarak görüntülenmiştir. Çatlak ilerleme hızının kesme dalgası hızına ulaştığı ve ilk çatlak uzunluğundaki artışın çatlak ilerleme kararlılığını kararsızdan kararlıya çevirdiği gözlemlenmiştir. Son olarak, polikarbon kirişlerde eğimli zayıf arayüzün dinamik arızası deneysel ve sayısal olarak çalışılmıştır. Deneylerde çatlak etrafındaki izokromatik çizgileri görüntülemek için tam alan tekniği olan fotoelastisite kullanılmıştır. Sayısal çalışmada eğimli arayüzdeki ayrılma yapışkan alan metodu ile birlikte açık sonlu elemanlar analizi kullanılarak modellenmiştir. İlk çatlak uzunluğuna bağlı olarak kararlı ve kararsız çatlak ilerleme rejimleri erk salınım hızı hesaplarına da uygun olacak şekilde tespit edilmiştir. Ek olarak, çatlak ilerleme hızı kesme dalgası hızına ulaşabildiği gözlemlenmiştir.

Anahtar Kelimeler: delaminasyon, eğimli arayüzler, arayüz çatlağı, eğimli kompozit laminalar

To my family

ACKNOWLEDGEMENTS

First and foremost, I would like to thank my research advisor Demirkan Coker for his support, optimism and positive reinforcement during my research and study at Middle East Technical University. I have been amazingly fortunate to have an advisor who gave me the chance to experience freedom of scientific research at the very beginning of my research career. He has been filled me with full of excitement at the toughest times of my graduate study. This thesis would not come into existence without his guidance and inspiring motivation.

I would like to give my gratitude to my fellow graduate students Burak Gözlüklü, İmren Uyar, Başar Kütükoğlu, Miray Arca and Aydın Amireghbali who are members of the Coker lab where I studied and conducted research for three years. I appreciate their friendship and I would like to mention that it was a great experience to work with them.

I would also like to thank Kubilay Demiralan, Muhittin Kaplan, and Ahmet Uyar for their effort during experimental fixture and specimen manufacturing.

Finally, I would like to thank my family for their unconditional support throughout my life. I thank my mother, Cavide, for always encouraging me to pursue a career in science. I thank my father, Osman, his endless love and care. I thank to my brother, Gökhan, for being a good role model in terms of his outstanding academic career and excellent personality. Finally I thank to my wife, Seval, for her endless love and support.

Financial support for this work was provided by the Ministry of Science, Industry and Technology (Grant# 00785.STZ.2011–1).

TABLE OF CONTENTS

CHAPTERS

LIST OF TABLES

TABLES

LIST OF FIGURES

FIGURES

CHAPTER 1

INTRODUCTION

1.1 Definition of the Problem

Composite materials have been in increasing demand most recently in modern commercial aircraft and wind turbine industries (Figure 1.1 (a) and (d)) because of their high stiffness and strength properties. With recent advances in manufacturing technologies, metal aircraft parts such as curved composite flange have been replaced by composite correspondents. One of the widely used metallic structures that are being converted to composite laminate is the curved flanges of ribs and spars in aircraft wings or the corner of the wind turbine box structure (Figure 1.1 (b), (c) and (e)).

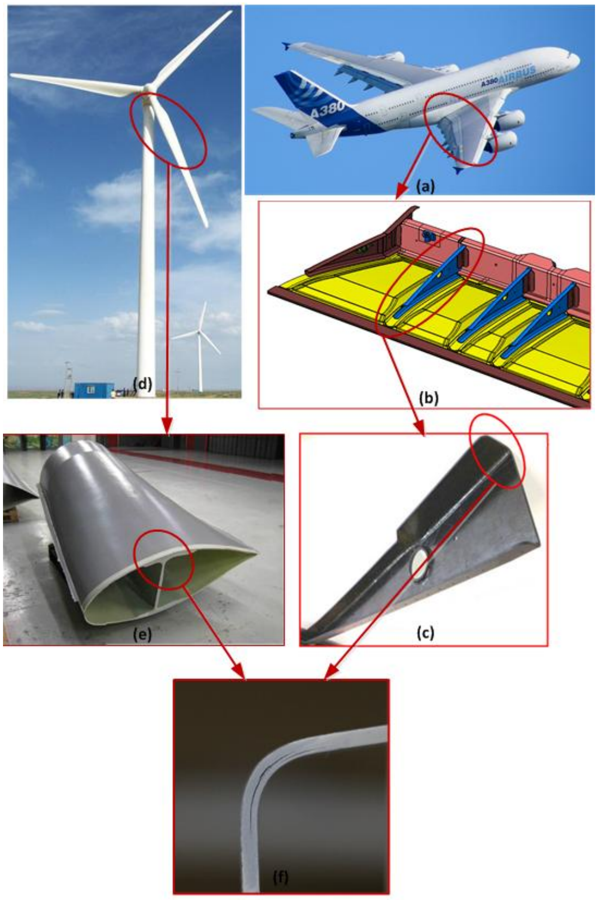

Figure 1.1 (a) A modern civil aircraft, (b) Cut-out view of a typical wing structures (yellow colored parts represents skin of the wing and blue colored parts represents ribs), (c) composite rib structure having curved region, (d) a typical wind turbine, (e) cross section of wind turbine blade (composite spar having curved flanges shown in red circle) (f) delamination observed in curved region.

Figure 1.2 illustrates different types of loads applied on a typical rib structure [1]. Although the direction and magnitude of the loading may vary depending of the flight conditions, the origins of the loads exerted on a typical rib structure can be listed as the following:

- Load-1: distributed pressure load due to air and fuel pressure.
- Load-2: chord-wise tension and compression loads due to Poisson's ratio effect in skins and end loads caused by spars.
- Load-3: concentrated load caused by attachment of flap track.
- Load-4: distributed out of plane load fuel pressure.
- Load-5: in-plane moment due to air pressure distribution.

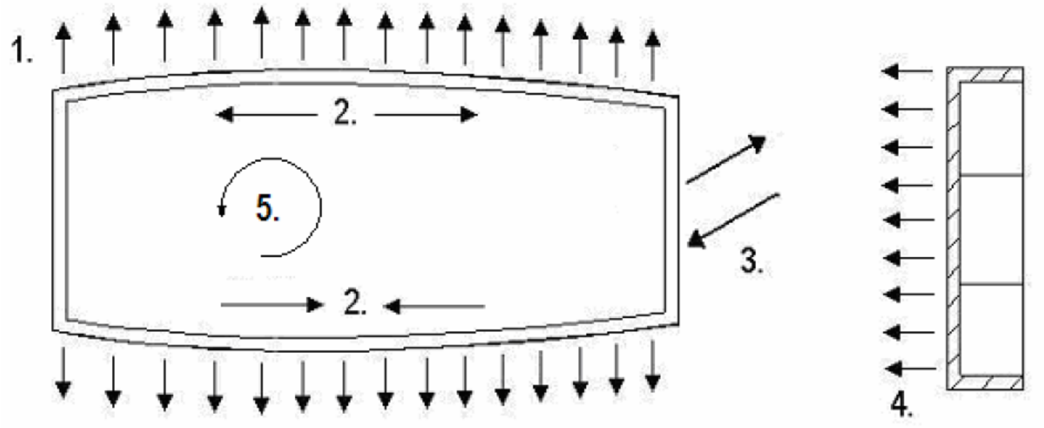

Figure 1.2 Loading state in a typical rib [1]

Despite of complex loading on the rib structure, the loading in a typical curved composite flange can be reduced to three simple loading cases namely axial load, (P) the force parallel to the arm; shear load, (V) the force perpendicular to the arm; and the moment (M) shown as Figure.1.3 (a), (b), and (c). The analytical solution of an anisotropic curved structure developed by Lekhnitskii [2], shows that all types of these loading cases create high interlaminar tensile (opening) stresses, which is undesirable for composite structures, in addition to the shear stresses on the curved region of the composite flanges. Consequently these opening stresses cause delamination on the curved region [3, 4, and 5] of the composite flanges (Figure 1.1 (c)).

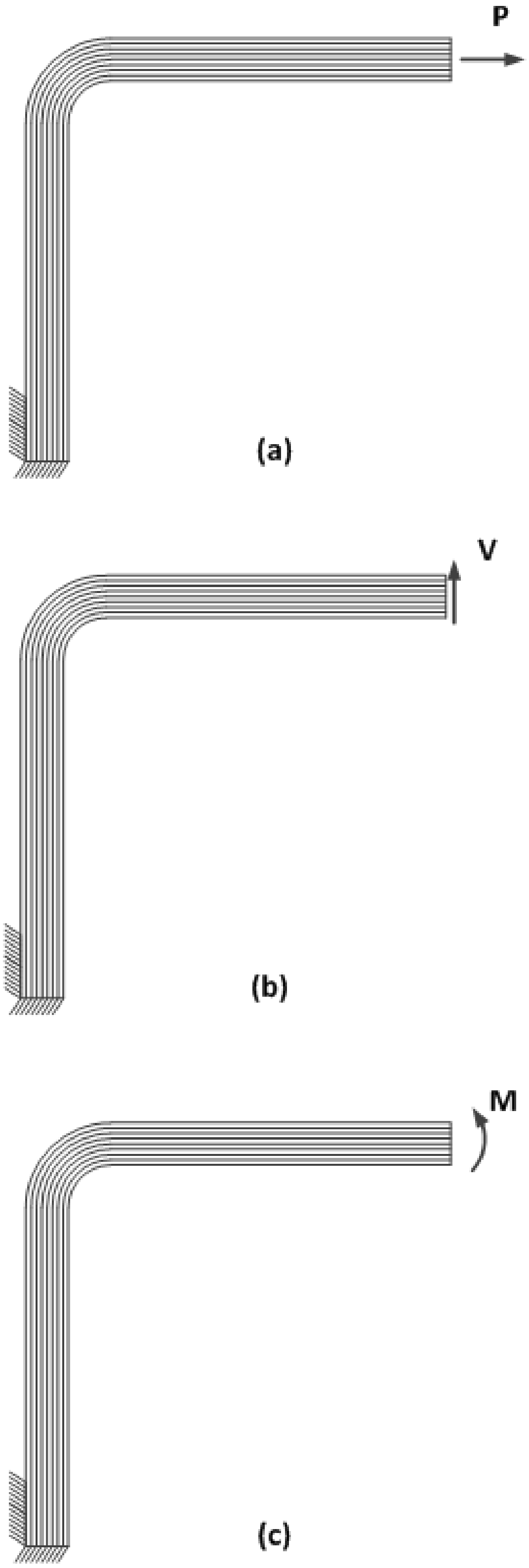

Figure 1.3 Boundary conditions for a typical curved composite flange (a) axial load case, (b) shear load case, (c) moment case.

1.2 Review of Previous Studies

1.2.1 Delamination of Composite Structures

Delamination, which is defined as separation of the laminated layers, is one of the major failure modes of composite structures. Delamination can be seen as an interfacial crack between two anisotropic materials. The delamination in composite structures is observed as a result of high interlaminar tension and shear stresses. The sources creating interlaminar tension and compression stresses are the material and structural discontinuities. Some of the sources are shown in Figure 1.4. Delamination occurs usually as a result of mixed mode fracture in which all three failure modes of fracture, namely Mode-I, II and, III, exist. In other words, delamination growth can be perceived as a mixed-mode crack growth because of the fact that the delaminations have to grow between layers of composite [8].

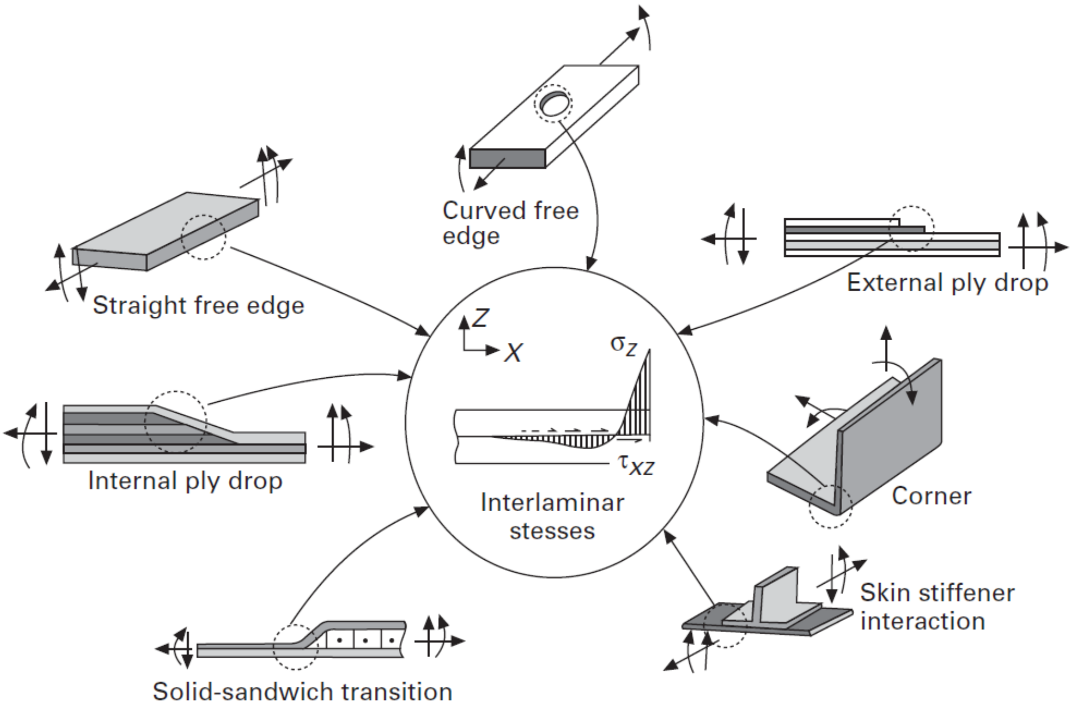

Figure 1.4 Common sources of delamination [8]

Delaminations in layered composite structures were classified into two types according to their locations in the structural parts by Bolotin [9]. The first type is the internal delamination which exists within the composite part (Figure 1.5 (a)). This type of delamination may result in a catastrophic failure of a structural component since it is hard to inspect internal delaminations using visual inspection techniques. The second type is near-surface delamination which exists on the surface on the composite part (Figure 1.5 (b)). The stability issue for the near-surface delaminations is important since the local instability for the near-surface delaminations may results in global instability of the structural components under compression loading .Although it is not the separation of the laminas, multiple cracking with in the composite part can be considered as a delamination type. The multiple cracking also affects the load carrying capacity of the composite part.

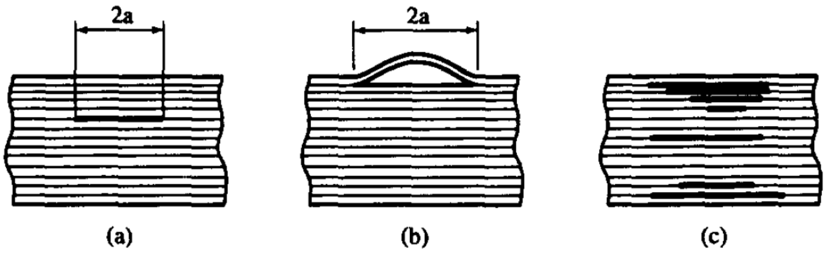

Figure 1.5 Three types of delaminations (a) internal delamination, (b) near-surface delamination, (c) multiple cracking. [9]

1.2.2 Delamination of Curved Composite Beams

Although delamination at the curved region of composite laminates is an important problem, there has been limited literature on the failure of curved composite laminates. In the literature the delamination due to the force perpendicular to the arm namely shear load (V) was mostly studied since it was found to be more critical in terms of opening stresses. Martin et al. [3, 4] studied the delamination of curved composite laminates in 1990s. They investigated analytically, computationally, and experimentally the delamination failure in a unidirectional curved composite laminate under the shear loading (V). They used a closed form curved beam elasticity solution and 2-D finite element analysis to determine the location of highest radial stress in curved region where the delamination is assumed to initiate. They showed that delamination propagates in to the arms of the laminate predominantly in Mode-I using energy release rate analysis. Their main experimental observations on the phenomena were that the major delamination initiates dynamically near the mid laminate of curved region and after the initiation, delamination propagates unstably towards arms. Dynamic initiation and propagation of the major delamination is followed by subsequent delaminations that initiate and propagate inner and outer layers of the curved region. Figure 1.6 (a) illustrates the loading mechanics used in their experimental study and Figure 1.6 (b) illustrates the major delamination observed at the mid-layer of the curved region and sequential delaminations.

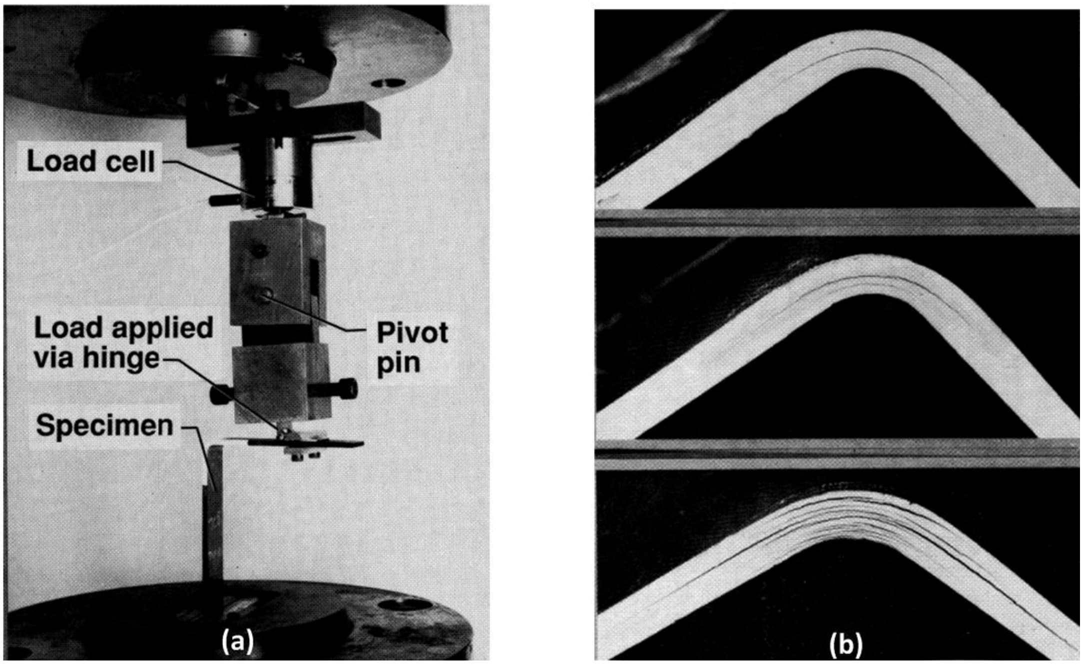

Figure 1.6 (a) Loading Mechanism used by Martin et.al (b) Delamination observed at the mid-plane of the curved region [3, 4]

After almost twenty years, the same problem was revisited by Wimmer et al. [5, 6, and 7]. They studied the formation of delamination and growth of existing delamination in [0/90] lay-up curved composite laminates under loading perpendicular to the arm (V) experimentally and computationally. For this purpose, they conducted experiments and finite element analyses for specimens with and without initial delamination. They carried out finite element analyses using Virtual Crack Closure Technique (VCCT) method, in which the initiation and propagation of delamination are analyzed in two separate stages and found that crack propagation in curved composite laminates is unstable for small initial delaminations existing on curved region. In their load displacement behavior obtained from both experiments and finite element analyses, after an initial elastic increase a large sudden load drop is observed that corresponds to delamination initiation followed by unstable delamination propagation (Figure 1.7 (a)). They also computationally observed that the length of initial delamination existing at the curved region affects the delamination growth stability. When the initial delamination length is increased the crack growth becomes stable and the large sudden drop in load displacement curve is not observed (Figure 1.7 (b)). Although they predicted the effect of initial delamination length on crack growth stability computationally, they were not able to observe the same stability characteristic experimentally. In their experimental study, they conducted all experiments for composite laminates without initial delamination under shear loading using the loading mechanism shown in Figure 1.8 (a). The load displacement curves obtained from experiments and finite element analysis are presented in Figure 1.8 (b). There is a large variance between their experimental and predicted load displacement results in terms of stiffness and maximum failure load according to Figure 1.8 (b).

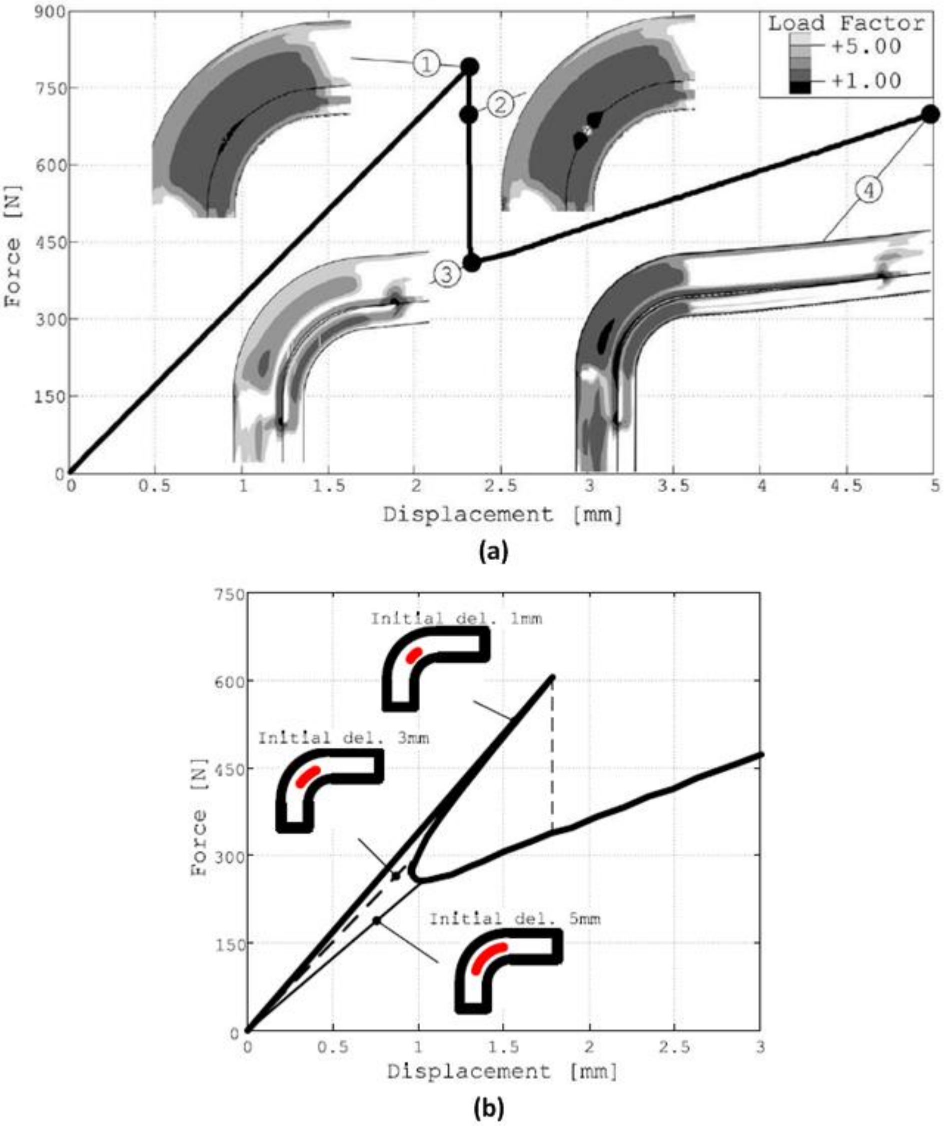

(a)

(b)

Figure 1.7 (a) Load displacement curve showing a large sudden load drop, (b) Effect of initial delamination length on the delamination growth stability [5]

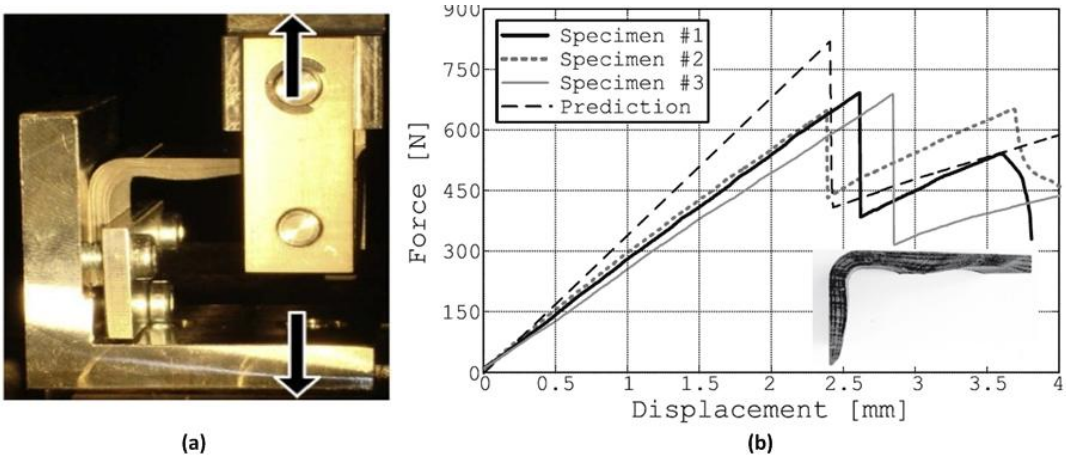

Figure 1.8 (a) Loading Mechanism used by Wimmer et.al., (b) Load displacement curves obtained from FEA and experiments [5]

Delamination of unidirectional curved L-shaped composite laminates under axial loading (P) were studied computationally by Gozluklu and Coker [10]. They carried out explicit finite element analysis with cohesive elements to model delamination in composite L-beams subjected to axial loading (P) instead of perpendicular loading (V). They carried out simulations of dynamic delamination propagation using a sequential implicit/explicit finite element analysis in conjunction with cohesive zone method along the central interface for a unidirectional L-shaped composite laminate. They observed that the delamination growth is unstable, which is defined as sudden and large load drop in load displacement curved shown as Figure 1.9. The crack tip positions corresponding to A, B, C, and D points in load displacement curve and opening stresses are presented in Figure 1.10. Crack completes its propagation during this sudden load drop according to Figure1.9 and Figure 1.10. They showed delamination growth with very high crack tip speeds and elastodynamic effects under shear dominated stresses near the crack tip. They also noted the existence of a possible second delamination failure mode that is the nucleation of a secondary delamination in the arm region.

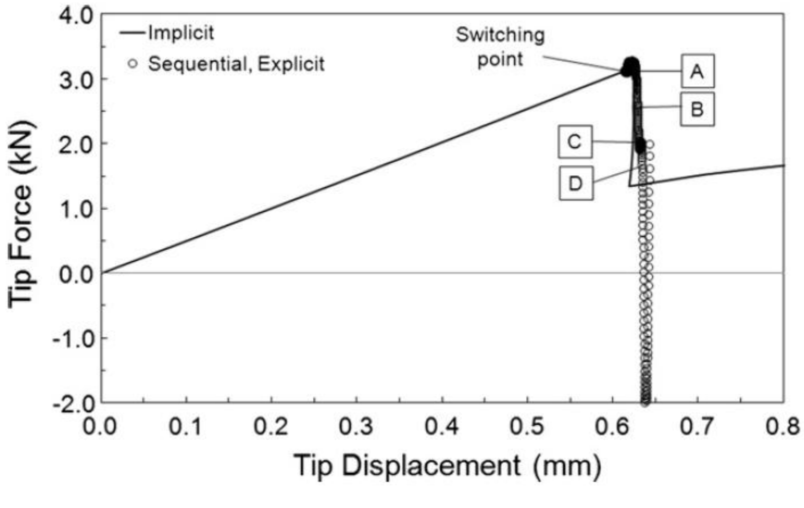

Figure 1.9 Load displacement curve [10]

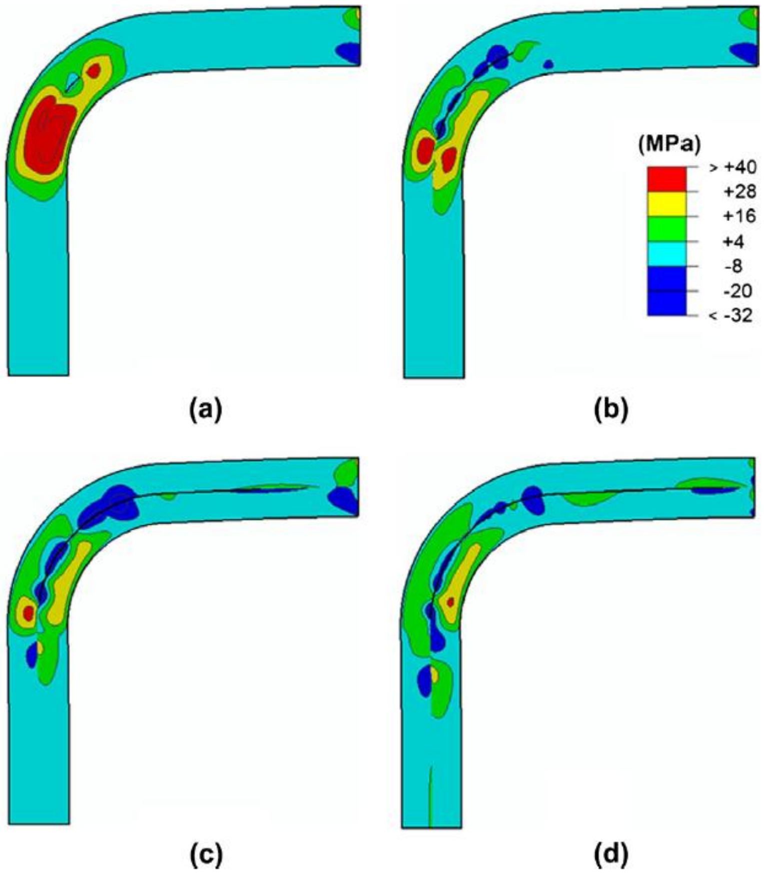

Figure 1.10 crack tip positions that correspond A, B, C, and D points in load displacement curve and opening stresses [10]

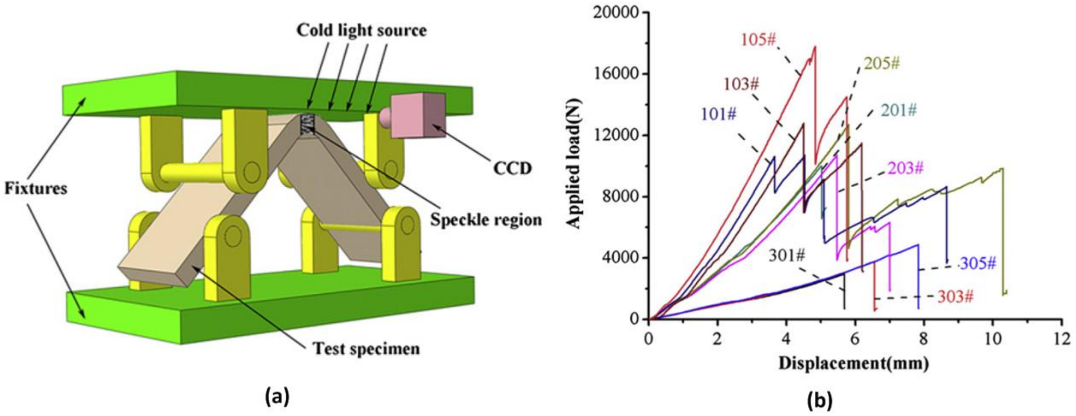

Figure 1.11 (a) Four point bending loading fixture, (b) load displacement curved obtained for different thicknesses [11]

The failure of carbon/epoxy laminated curved beams under moment loading was studied experimentally by Hao et. al. [11]. They conducted experiments using four pint bending loading fixture to simulate pure bending moment loading on the curved composite beam (Figure 1.11 (a)). In their experimental study optical method of Digital Speckle Correlation Method (DSCM) and strain gages were employed. They obtained failure strength and the maximum failure radial stress of the curved composite beams for different thicknesses and different radius-thickness ratios. The load displacement curves obtained for specimens in different thicknesses are presented in Figure 1.11 (b). A sudden and large load drop in load displacement curves is observed for all specimens. They observed the same unstable single delamination behavior in cross-ply laminates under moment loading. They were not able to capture the progress of the single delamination since the delamination growth is very dynamic. The strain distributions on the curved region obtained by using DSCM are presented in Figure 1.12 for before and after the failure. It is shown that before the failure opening strains (Y-strain in Figure 1.12) have their maximum values in the mid-layer of the curved region where the delamination initiates.

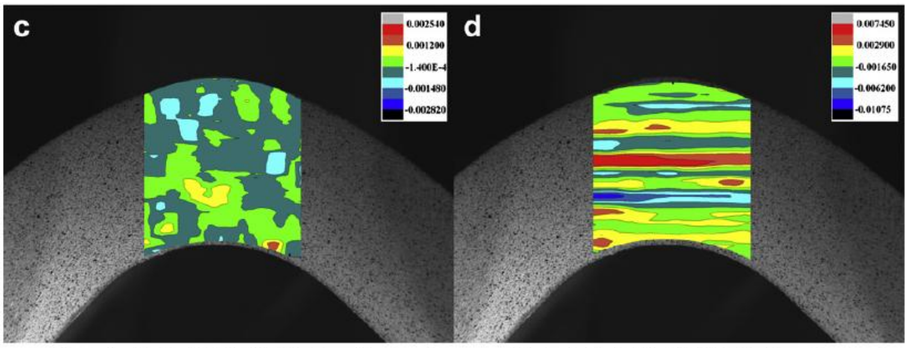

X-strain field (0-17800N before fracture) Y-strain field (0-17800N before fracture)

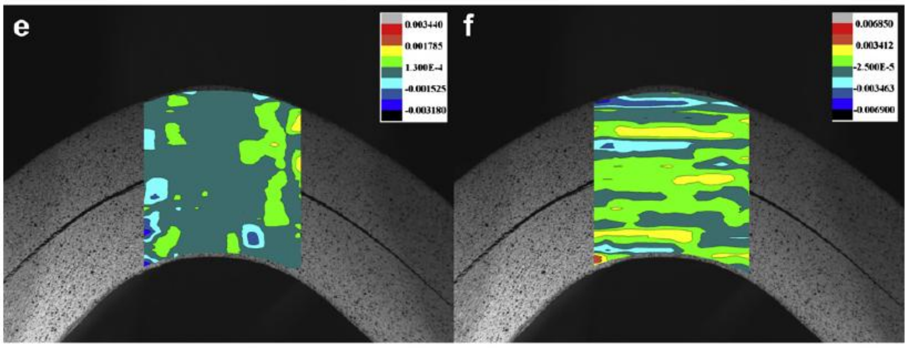

X-strain field (0-17800N after fracture) Y-strain field (0-17800N after fracture)

Figure 1.12 Strain field for unstable delamination before and after fracture [11]

Lu et. al. [12] computationally studied the delamination problem in curved composite beams under moment loading (Figure 1.13 (a)). They conducted finite element analysis in ABAQUS® to investigate the delamination in curved orthotropic beams. They presented the dependence of energy release rate on the crack length for three different location of the crack along radial direction (Figure 1.13 (b)). According to Figure 1.13 (b) non-dimensionless energy release rate is increasing with increasing crack length up to a certain crack length. After the crack length reaches this certain value non-dimensionless energy release rate decreases with increasing crack length. This observation shows that crack in curved beams under moment loading experience unstable crack growth if the crack length is sufficiently small. If the crack length is larger enough, the crack growth could be stable.

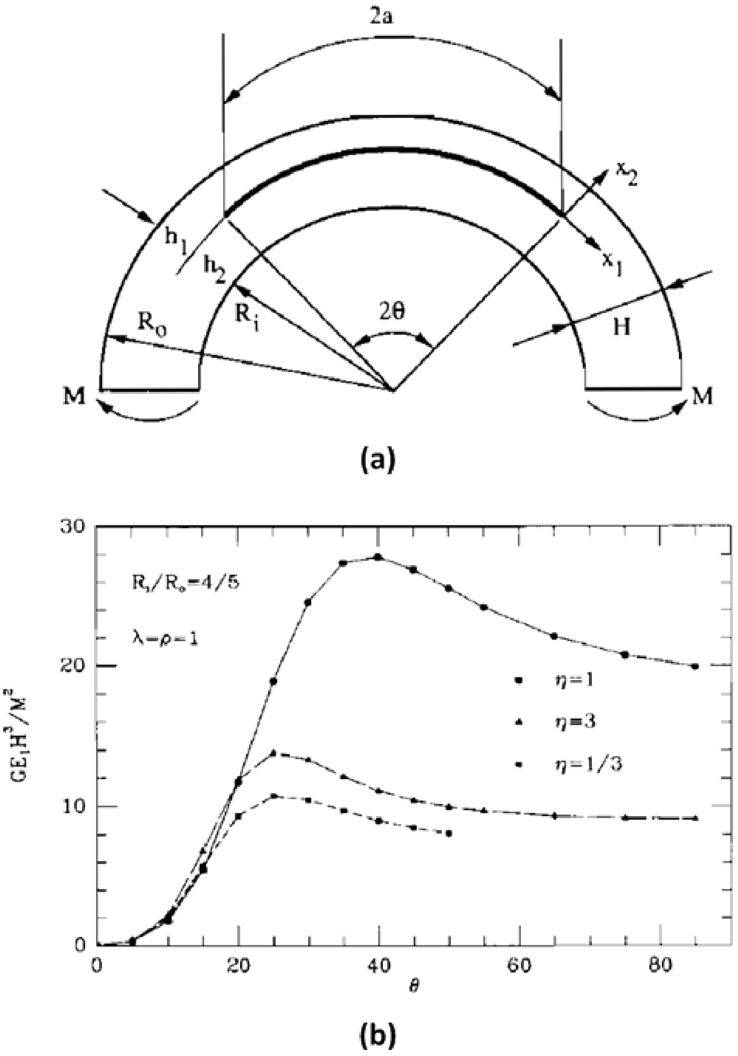

Figure 1.13 (a) Geometry and the loading for the problem, (b) non-dimensional energy release rate as a function of crack length for three different positions of the crack along the radial direction [12]

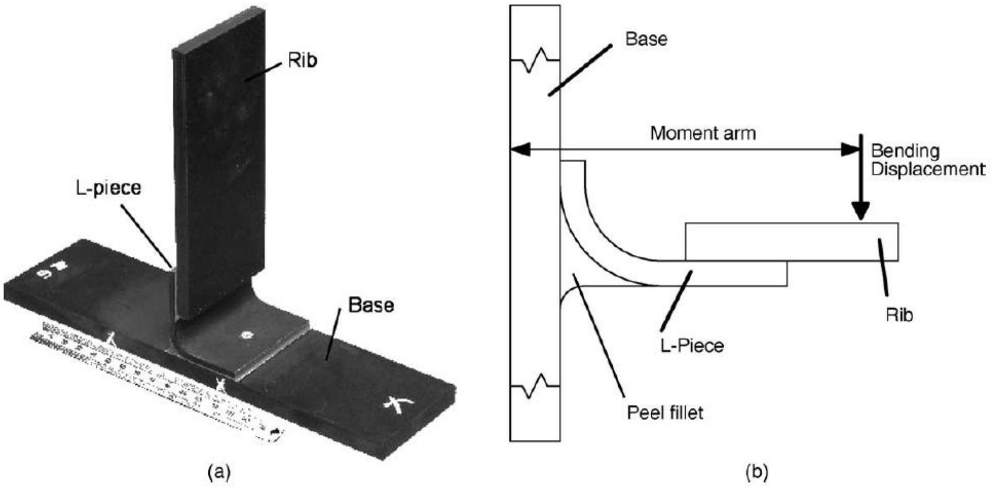

Figure 1.14 (a) Angled L-shaped composite joint connecting rib and base structures, (b) bending displacement loading that creates failure [13]

Feih et. al. [13] studied the delamination failure modes of angled L-shaped composite joints under bending deformation. Figure 1.14 (a) shows the angled L-shaped composite joints, which are used as a connecting part in the wing structures and Figure 1.14 (b) shows the bending displacement loading that creates delamination failure in the curved region. They conducted experiments and also finite element analyses in ABAQUS®. They observed different failure modes before delamination failure. Figure 1.15 (a) shows load-displacement curves obtained from finite element analysis and experiments. Their analysis and experiments are in a good agreement in terms of stiffness. The sudden and large load drops in load displacement curves show the delamination failure mode. However they also observed that matrix cracking due to tensile and compressive stresses exist in the inner and outer surfaces of the curved region respectively.

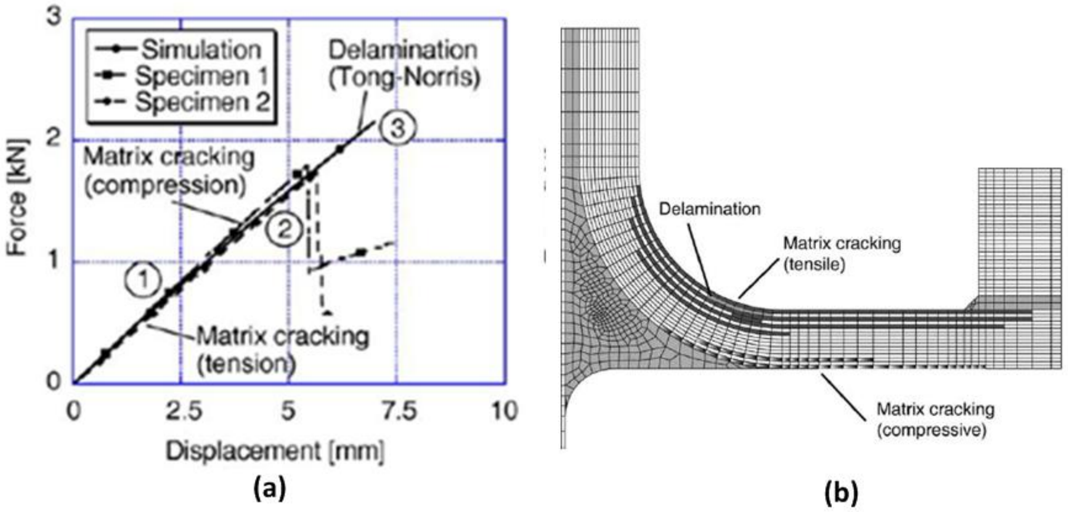

Figure 1.15 Load displacement curved obtained from finite element analysis and experiments (b) Different types of failure [13]

1.2.3 Dynamic Failure of Interfaces

Coker et. al. [14] conducted experimental work on dynamic failure of thick unidirectional graphite-epoxy composite plates. As shown in Figure 1.16 (a), they used specimens having an edge pre-notch machined in the fiber direction and specimens were loaded by impact projectile either symmetrically (Mode-I) or asymmetrically (Mode-II). They used optical technique of Coherent Gradient Sensing (CGS) in conjunction with high speed photography to capture the failure process (Figure 1.16(b)).

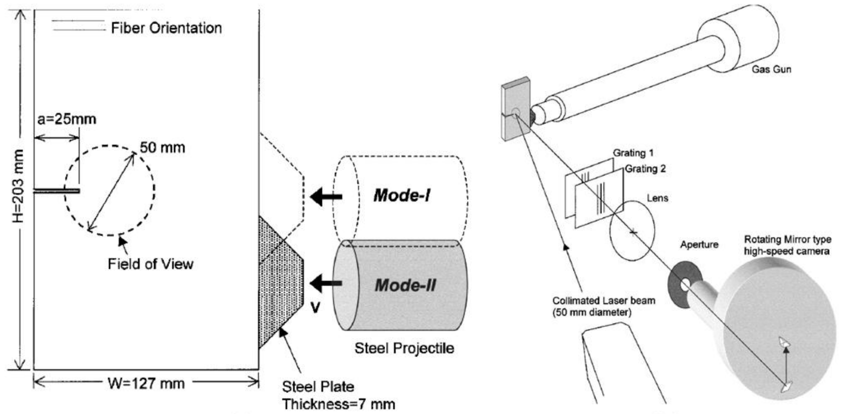

(a) (b)

Figure 1.16 (a) Specimen geometry and Mode-I and Mode-II loadings, (b) Experimental setup used by Coker et. al. [14]

Coker et. al. [14] showed that Mode-I crack s may only propagate sub-sonically along the fibers with respect to the homogenized anisotropic material properties with an upper bound of Rayleigh wave speed as shown in Figure 1.17. However, for Mode-II cracks it is observed that they propagate in the direction of fiber intersonically. Mode-II cracks start to accelerate from the shear wave speed and their speeds can reach the critical intersonic speed, obtained using homogenized anisotropic material properties.

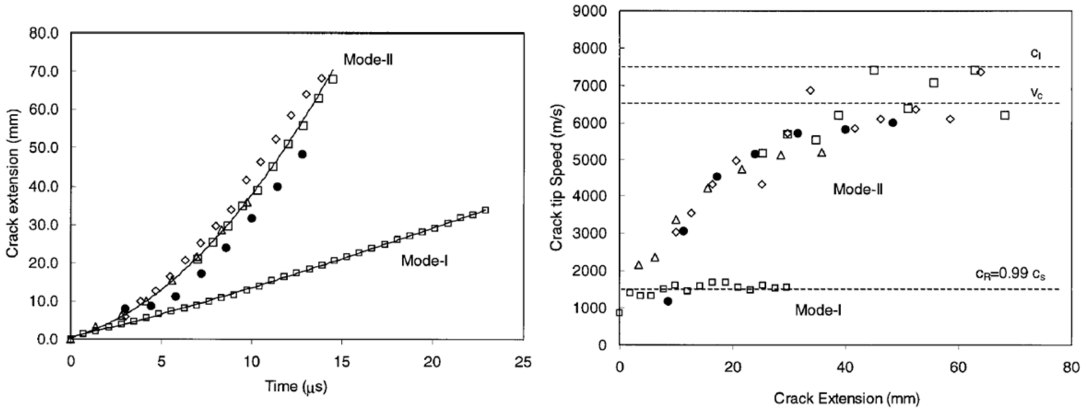

(a) (b)

Figure 1.17 (a) Crack tip positions as a function of time, (b) crack tip speed as a function of crack tip position for Mode-I and Mode-II cracks [14]

After their study, Rosakis et. al. showed the same intersonic crack propagation behavior along the weak interface in Homalite-100 under asymmetric impact (Mode-II) loading. They conducted experiments using bonded Homolatie-100 plates having a pre-notch at the bonding interface. The specimen is subjected to asymmetric impact by a projectile fired form a high speed gas gun. They used full field technique of photoelasticity in conjunction with high speed imaging for capturing the stress field near the propagating crack tip.

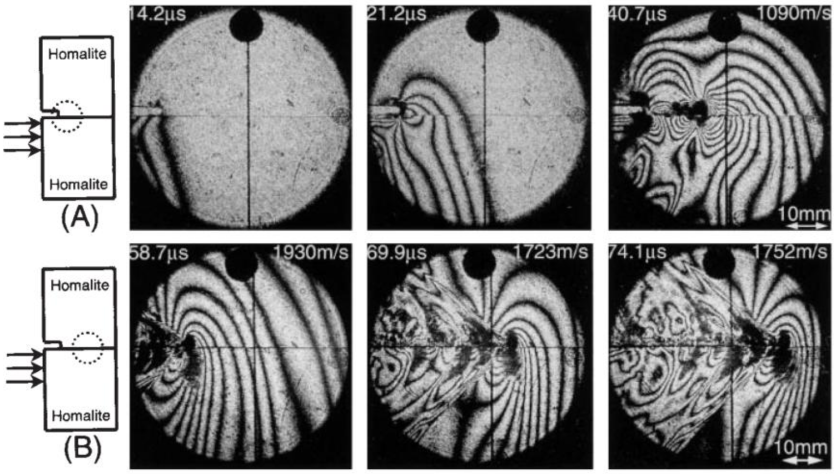

Figure 1.18 High speed images showing the isochromatic fringe pattern around propagating shear dominated crack along a weak plane in Homalite-100 [15]

They observed that shock wave, which refers crack tip speed slightly higher than $\sqrt{2}c_S$ (shear wave speed), in isochromatic stress field obtained from dynamic photoelasticity experiments as shown in Figure 1.18. Figure 1.19 shows the crack tip speed calculated using different methods as a function of crack tip location. Crack starts to propagate with a speed of shear wave speed, and then its speed reaches value of $\sqrt{2}c_S$, which corresponds to the critical intersonic speed for unidirectional composites. Thus Coker and Rosakis showed that dynamic failure of heterogonous composite material can be modeled using homogenous material with a weak interface.

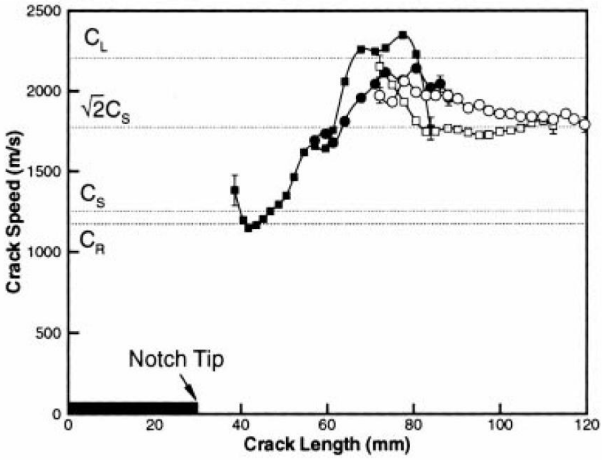

Figure 1.19 Crack tip speed as a function of crack length [15]

1.2.4 Fracture Mechanics Background

The assumption of continuous material and averaging methods to predict to material failure do not work no longer when micro-cracks and voids in the material grow in size and become localized. This localization results in macroscopic crack, and it may cause global failure of the material unexpectedly. Hence, discontinuities in the material must be taken into account to predict the failure correctly. As a result of this fact fracture mechanics was born. Griffith [16] has shown in 1921 that attention should be given to the behavior of an existing crack. Fracture mechanics assumes that there is a single crack within the materials and tries to get answers theoretically and experimentally for the following questions:

- Will a crack grow under the given load?
- When a crack grows, what is its speed and direction?
- Will crack growth stop?
- Will crack growth be stable or unstable?

One of the widely used fields of fracture mechanics is Linear Elastic Fracture Mechanics (LEFM). LEFM assumes the material obeys linear elastic material behavior.

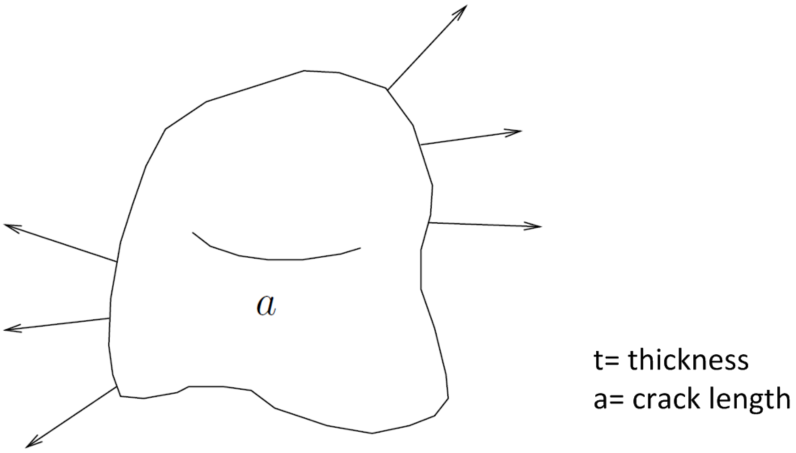

Figure 1.20 Plate with a line crack [17]

One of the methods to predict the crack growth is based on an energy balance. Griffith [16] postulated that crack growth will occur, when there is enough energy available to generate new crack surface. Energy release rate, which is the change of potential energy per unit crack area, an important term for Griffith energy balance criterion. If a line crack in a plate with a thickness of t is considered (Figure 1.20), energy release rate is mathematically defined as in equation (1.1), where U_e is the total amount of energy that is supplied externally to the material, U_i is the internal energy of the material, and a is the crack length [17].

$$G = \frac{1}{t}\left(\frac{dU_e}{da} - \frac{dU_i}{da}\right) \tag{1.1}$$

According to Griffith's energy balance criterion if the energy release rate equals to the crack resistance force, a crack will grow. Equation (1.2) is the mathematical presentation of this criterion, where G is the energy release rate and γ is the surface energy of the material.

$$G = 2\gamma \tag{1.2}$$

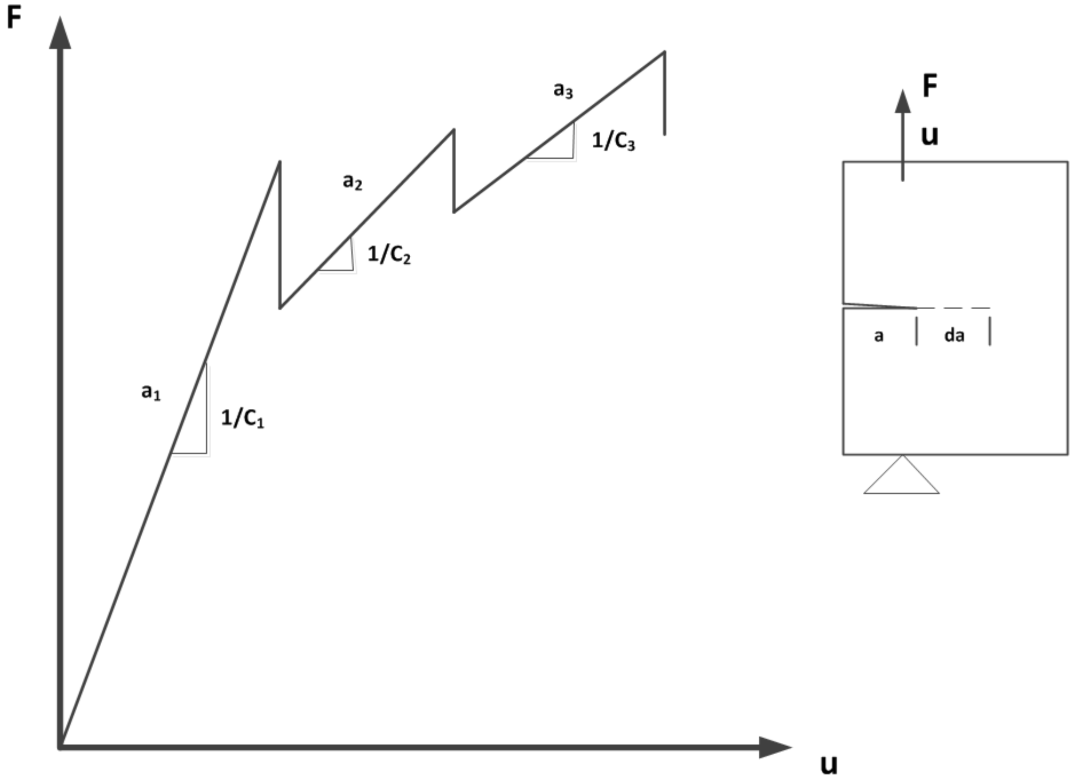

Figure 1.21 Load displacement curved obtained from a displacement controlled experiment

Energy release rate can be calculated using load displacement curve obtained from an experiment. Fixed grip approach is used for experimental data obtained using displacement controlled testing machine (Figure 1.21). For this approach, the external energy (U_e) equals to zero and the change of the internally stored elastic energy (dU_i) can be expressed in terms of displacement (u) and the change in applied force (dF) as expressed in Equation (1.4).

$$dU_e = 0 \tag{1.3}$$

$$dU_i = \frac{1}{2}\, u\, dF \tag{1.4}$$

The energy release rate can be expressed as Equation (1.5) by using Equations (1.1), (1.2), and (1.3). In this expression C is compliance and can be calculated as C=u/F for different crack length values.

$$G = \frac{1}{2t}\, F^2\, \frac{dC}{da} \tag{1.5}$$

The change in energy release rate with respect to the change in crack growth length determines the crack growth stability. As shown in Equation (1.6), for brittle fracture if dG/da is greater than 0 crack growth will occur unstably, otherwise the crack growth will occur stably.

$$\frac{dG}{da} = \begin{cases} > 0 & Unstable \\ < 0 & Stable \end{cases} \tag{1.6}$$

Irwin [18] introduced three different loading modes for fracture mechanics. At the crack tip the stress field can be divided into three components, namely Mode-I, Mode-II, and Mode-III as shown in Figure 1.22. Mode-I causes the crack to open orthogonal to the local fracture surface. Mode-II causes the crack surfaces to slide relative to each other in the x_1 direction. Mode-III causes the crack surfaces to slide relative to each other in the x_2 direction.

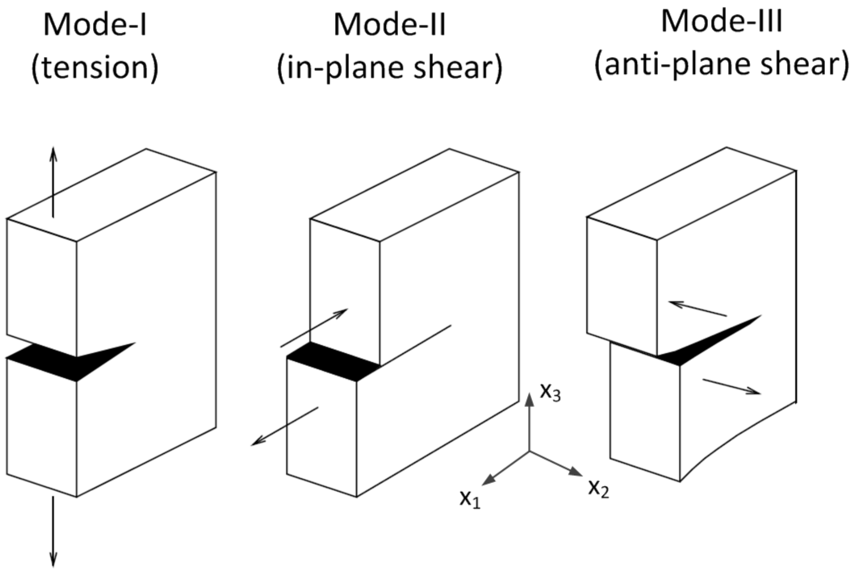

Figure 1.22 Modes of fracture [17]

1.2.5 Cohesive Zone Method (CZM)

Cohesive Zone Method (CZM) is one of widely used methods to model the interfacial crack in finite element analysis. The concept of cohesive zone theory was firstly proposed by Barenblatt [19, 20] for brittle fracture. At the same time, Dugdale [21] independently developed the concept of cohesive stress. As a result of their studies basics of CZM was established. According to their studies, the existence of the process zone in front of the physical crack tip was showed (Figure 1.23 (a) and (b)). The fracture energy is dissipated by the process zone while the crack growth occurs. A typical distribution for cohesive stresses existing on the process zone as a function of separation distance between mating surfaces is given in Figure 1.24. The cohesive stress at the mathematical crack tip, which is the end of the process zone, is zero, and it increases and reaches its maximum value with increasing separation distance (δ). After it reaches its maximum value, it decreases and reaches zero while separation distance increases.

CZM has variety of advantages compared to other methods to model the crack growth in materials. The other methods may require an initial crack and a described direction for the crack propagation. In CZM, however, a crack can easily initiate without an initial crack and propagate toward to an arbitrary direction where cohesive elements exist. CZM can create new surfaces while maintaining continuity condition mathematically. In addition, CZM uses interface parameters including critical traction and energy release rate of the interface material which can be obtained from fracture experiments.

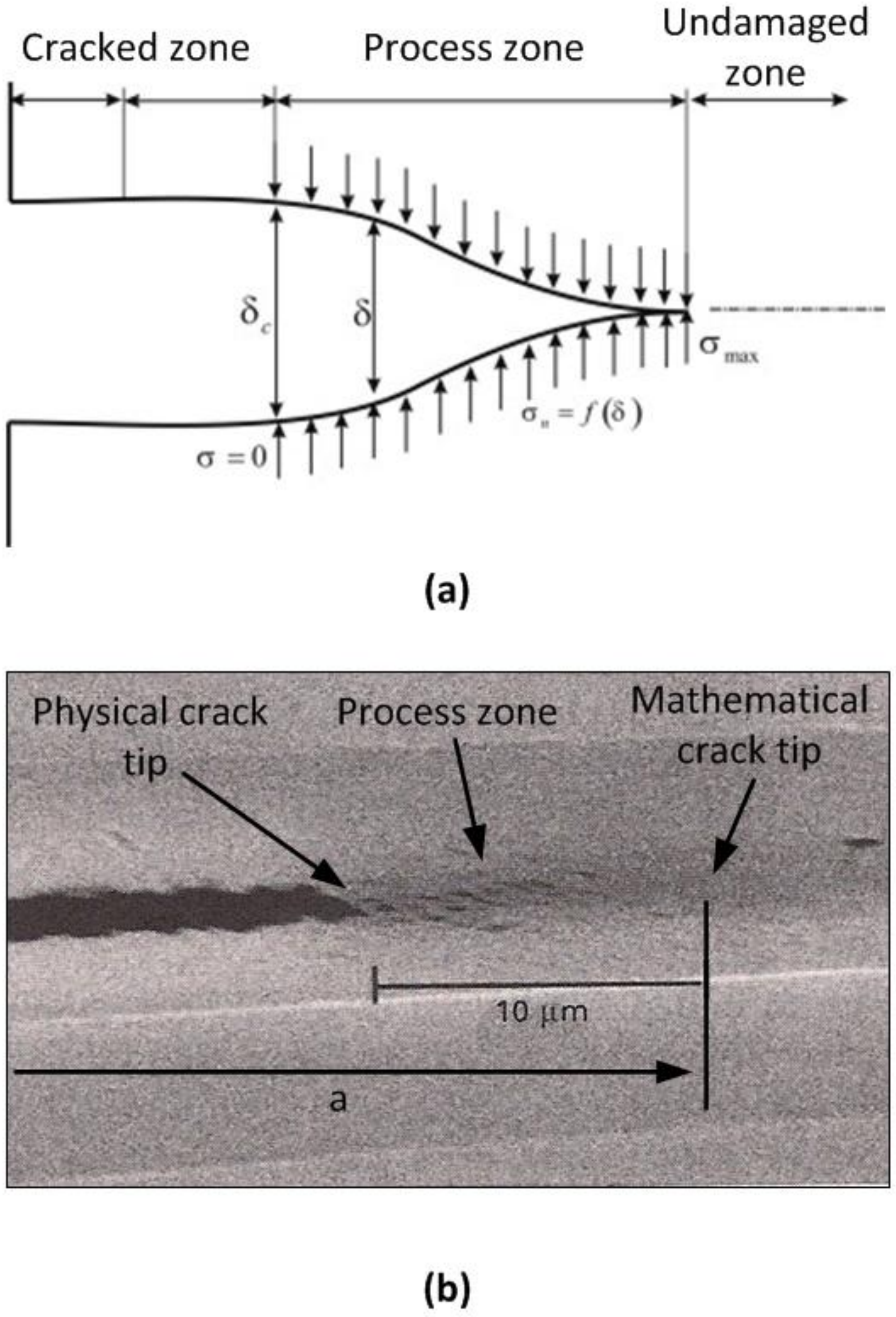

Figure 1.23 (a) Schematic of a crack, (b) Existence of process zone in front of a physical crack tip

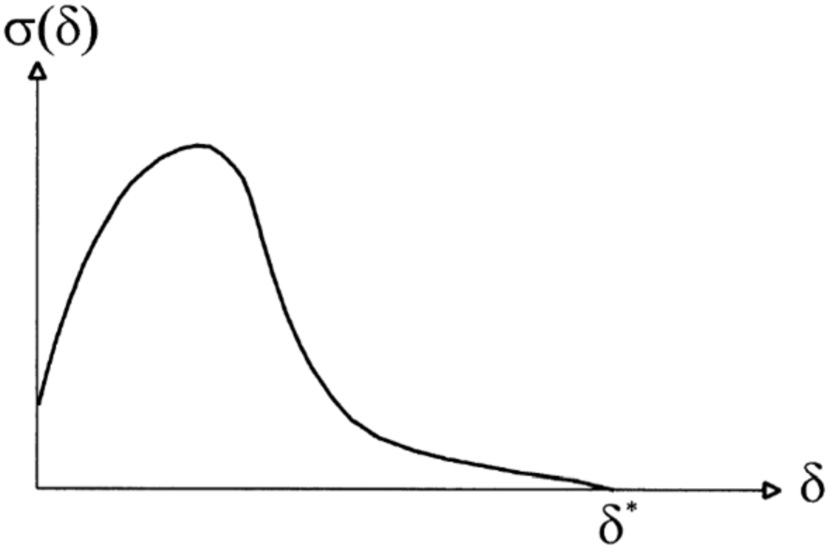

Figure 1.24 Cohesive stress and displacement curve.

1.3 Scope of the Study

This study aims to investigate experimentally and computationally dynamic failure of curved interfaces existing between composite laminates and polycarbonate beams. For this purpose, dynamic failure of curved composite beams subjected to quasi-static axial loading is studied computationally in Chapter 3, dynamic failure of curved composite beams subjected to quasi-static shear loading is studied experimentally in Chapter 4, and dynamic failure of curved interfaces of polycarbonate beams subjected to quasi-static shear loading is studied in Chapter 5 (Figure 1.25).

In chapter 3, delamination in unidirectional curved composite beams under quasi-static axial loading is modeled using dynamic (explicit) finite element analysis in conjunction with cohesive zone methods. Loading is applied parallel to one arm quasi-statically while delamination occurs dynamically. It is observed that delamination is highly dynamic and that as the initial crack grows, the crack tip speed reaches the Rayleigh wave speed of the composite material with increasing laminate thickness and decreasing initial crack length. A second observation is that a secondary delamination crack in the arm region nucleates depending on the initial crack length and thickness values. Thus, structural assessment based on the initial crack length may lead to a conservative approach in design applications.

In chapter 4, the delamination failure in unidirectional curved composite beams under quasi-static shear loading is experimentally investigated. A unique experimental loading fixture is designed and manufactured in order to apply shear loading to the specimens. The dynamic delamination propagation is captured using Photron© Fastcam SA5 ultra high speed system. The effect of initial crack length on the crack growth stability is investigated and it is shown that the small initial crack results in unstable crack growth whereas the larger initial crack results in stable crack growth. In addition crack propagation speed is found to be in the order of the shear wave speed.

In chapter 5, delamination in unidirectional curved composite beams is modeled with two curved polycarbonate beams bonded to each other where the effect of pre-crack length on the stability of the crack growth and crack propagation speed are investigated experimentally and computationally. In the experimental study, a unique testing fixture with a sliding platform is designed to create a pure shear loading. The full-field technique of photoelasticity in conjunction with high speed imaging is used in order to visualize isochromatic fringe pattern around the crack tip located at the bonded interface of the curved polycarbonate plates. In the computational study, debonding at the interface of curved polycarbonate beams is modeled using dynamic (explicit) finite element analysis in conjunction with cohesive zone methods. In numerical analysis, pure vertical displacement is applied to one of the arms to reflect the same loading condition as the experiment. Experimental and finite element analysis results are in agreement in terms of load-displacement behavior and stress distribution, which indicate a successful use of cohesive zone method in modeling of crack growth. Stable and unstable crack growth regimes, depending on the initial crack length, are identified in agreement with energy release rate calculations. In addition, the crack propagation speed is in the order of the shear wave speed according to both finite element analysis and experimental results similar to results obtained for unidirectional curved composite experiments.

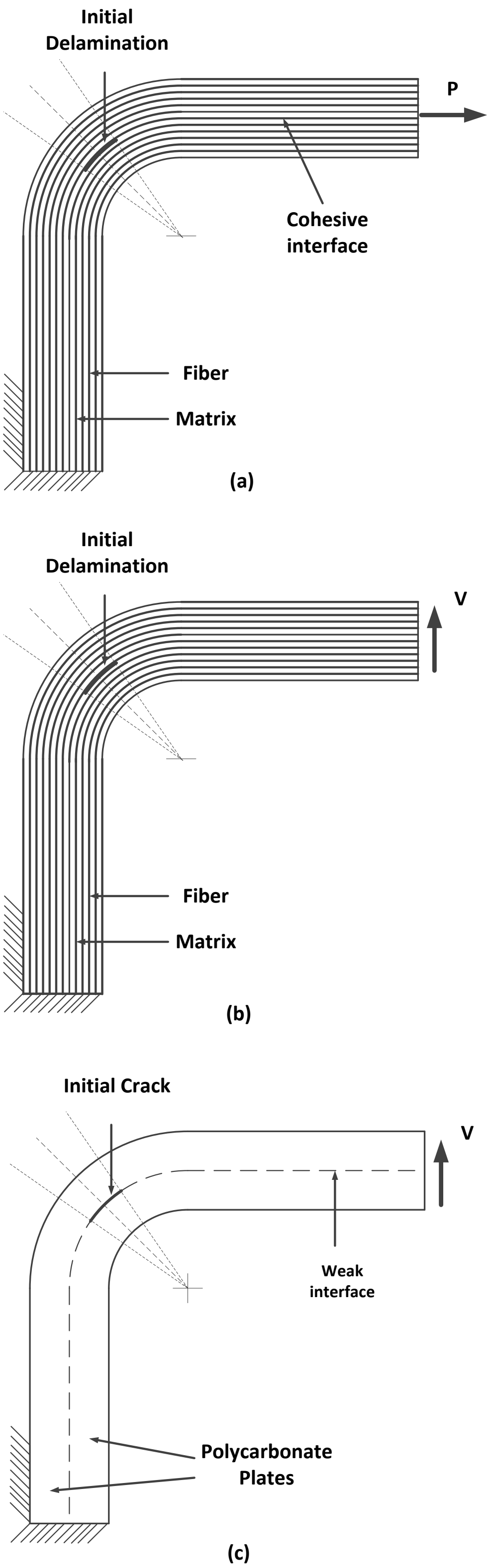

Figure 1.25 (a) Chapter 3: Dynamic failure of curved composite laminates subjected to axial loading, (b) Chapter 4: Dynamic failure of curved composite laminates subjected to shear loading, (c) Chapter 5: Dynamic failure of curved interface of polycarbonate plates subjected to shear loading.

CHAPTER 2

METHOD

2.1 Computational Framework

2.1.1 Crack Initiation and Propagation Criteria

The most frequently encountered damage in the composite structures of civil aircrafts is delamination [8, 9]. Once a thick composite laminate takes a sharply curved shape such as seen in the curved flanges of the spars, ribs and boxes, radial normal stresses are induced under the sectional forces at the bend. As a result, inter-laminar normal stress (t_I) is developed at the bend in addition to inter-laminar shear shear stress (t_{II}). Recalling the laminated structure of the composites, the laminate is more sensitive to interfacial normal stresses than inter-laminar shear stresses in terms of delamination initiation and propagation.

Delamination can be initiated as soon as the point-wise interface strength is exceeded at the interface. An elliptical initiation criterion based on the normal and shear tractions is proposed by Ye [22] as follows in Equation (2.1);

$$\left(\frac{t_I}{t_{Ic}}\right)^2 + \left(\frac{t_{II}}{t_{IIc}}\right)^2 = 1 \tag{2.1}$$

where t_{Ic} and t_{IIc} are critical interface strengths for inter-laminar normal stress and inter-laminar shear stress, respectively. For this criterion, the interfacial strength is reduced if both inter-laminar normal stress (t_I) and inter-laminar shear stress (t_{II}) are acting. Moreover, since in general t_{IIc} is greater than t_{Ic}, the normal strength of the interface is more dominant for the determination of the mixed-mode interfacial strength.

In the case of an initially existing delamination, the interfacial normal loading would also promote the propagation of delamination. Fracture toughness for pure opening mode, G_{Ic}, and for pure shear mode, G_{IIc}, are determined experimentally by the Double Cantilever Beam (DCB) test and by the Four-Point Bend End-Notched Flexure (4ENF) test, respectively, whereas the mixed-mode fracture toughness (G_c) is taken into account by a combined Mixed-Mode Bending (MMB) test. A curve fitting approach to the MMB test is proposed by Benzeggagh-Kenane (BK) [23] and can be used as a mixed-mode delamination propagation criterion expressed in Equation (2.2),

$$G_c = G_{Ic} + (G_{IIc} - G_{Ic})\left(\frac{G_{IIc}}{G_I + G_{II}}\right)^{\eta} \tag{2.2}$$

where G_I and G_{II} are the energy release rates for pure Mode I and Mode II, respectively, and the parameter, η, is a curve fitting factor. In the propagation part also, since G_{Ic} is smaller than G_{IIc} the effect of tensile loading promoting the Mode-I crack propagation controls the propagation stage. In this study, both the point-wise stress and delamination propagation analyses are combined in the framework of the CZM.

2.1.2 Cohesive Zone Model

The cohesive zone method (CZM) was initially introduced by Dugdale [21] and Barenblatt [20] in order to model the process zone which acts a transition zone between the traction-free and intact regions. CZM is employed as an interface constitutive model which consists of a relation between the surface tractions (t) and the relative displacements (δ) between the mating surfaces. The use of CZM in a finite element model allows simulating the crack initiation and propagation. In this study, the bi-linear form proposed by Geubelle and Baylor [24] is used (Figure 2.1).

The relationship between the traction (t) and relative surface displacement (δ) is given by;

$$t = \begin{cases} E_0\,\delta, & \delta \le \delta_0 \\ (1-d)E_0\,\delta, & \delta_0 < \delta < \delta_c \\ 0, & \delta \ge \delta_c \end{cases} \tag{2.3}$$

In equation (2.3), E_0 is the initial (penalty) stiffness, which maintains adequately stiff response of the crack free body prior to softening at the interface. δ_0 is the delamination onset displacement which is determined by Ye’s tri-axial model [22] for the mixed-mode delamination onset as the following Equation (2.4);

$$\delta_0 = \delta_{IIo}\delta_{Io}\sqrt{\frac{1+\beta^2}{{\delta_{IIo}}^2 + (\beta\delta_{Io})^2}} \tag{2.4}$$

where β=((δ$_I$))⁄((δ$_{II}$)). Since this study is conducted for plane stress assumptions, the effect of Mode-III is not taken into account.

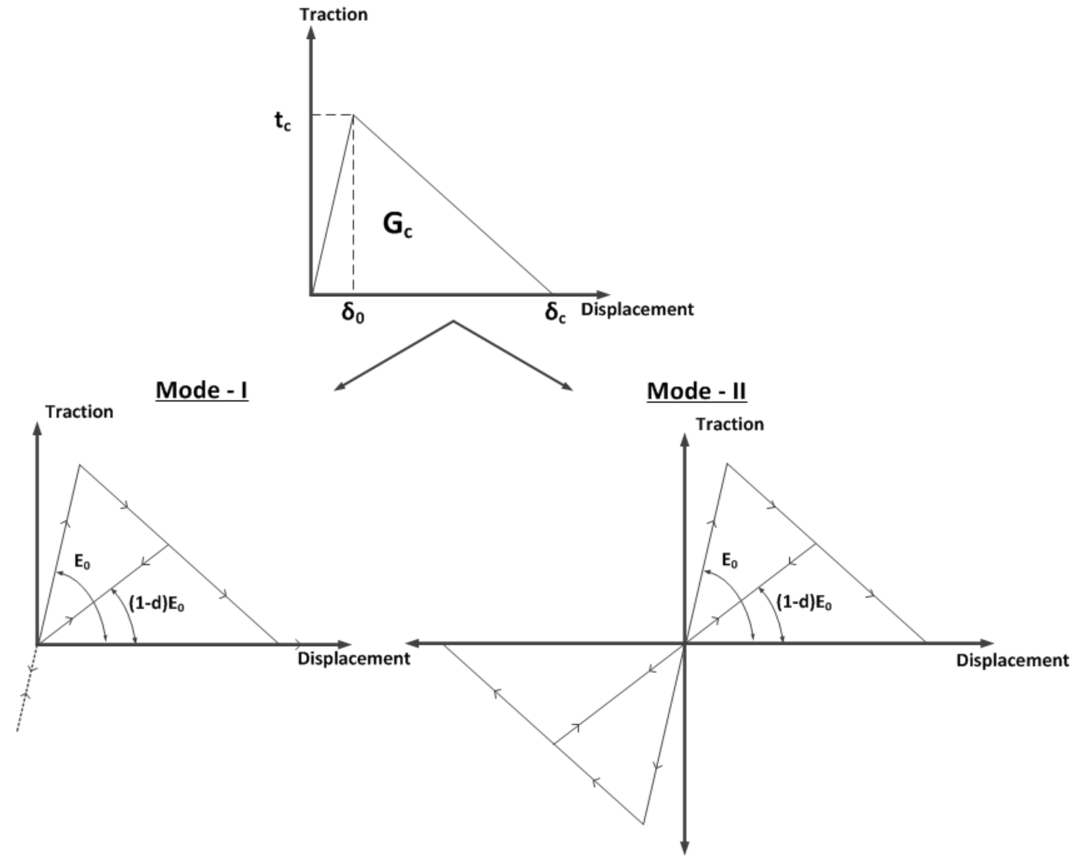

Figure 2.1 Relationship between interface traction and displacement according to bi-linear from of CZM proposed by Geubelle and Baylor [24]

The critical displacement (δ_c) corresponds to fully damaged interface. After the relative displacement is reached the critical displacement, the interface shows no resistance. The critical displacement can be related to the fracture toughness, since the area under traction-displacement curve is equal to energy release rate. According to mixed-mode fracture toughness criterion proposed by Benzeggagh and Kenane [23] the critical displacement is given by;

$$\delta_c = \frac{2}{\delta_o E_o}\left[G_{Ic} + (G_{IIc} - G_{Ic})\left(\frac{\beta^2}{1+\beta^2}\right)^{\eta}\right] \qquad (2.5)$$

where G_{Ic} , and G_{IIc} are the fracture toughness values in mode-I and mode-II respectively. The parameter, η, called B-K parameter, is the curve fitting value resulting from various experimental studies.

2.2 Experimental Framework

2.2.1 High Speed Imaging

In this study the high speed imaging equipment is required since crack initiation and propagation along the curved interface in composite laminates and polycarbonate plates is highly dynamic. For this purpose, Photron© Fastcam SA5 ultra high speed video system is used. The system has the ability to capture images at 1,000,000 frames per second with a resolution of 64x16 pixels. While working with ultra-high speed imaging system it is very important to provide required lighting. Two Dedoligth© DLHM4-300 tungsten light sources are used to illuminate specimens during experiments. Figure 2.2 illustrates the high speed camera system used in experiments.

2.2.2 Photoelasticity

Photoelasticity is an experimental method to determine the full field stress state in a material. This method is based on the property of birefringence seen on certain transparent materials. The birefringence materials have two refractive indices during a ray of light passing through them. Photoelastic materials show the birefringence property upon the application of stress. While light passes through a photoelastic material, its electromagnetic wave components gets resolved along the two principal stress directions and each of these components experiences different refractive indices due to the birefringence [25]. The stress state in the photoelastic material can be determined by analyzing the fringe pattern obtained from photoelasticity experiment.

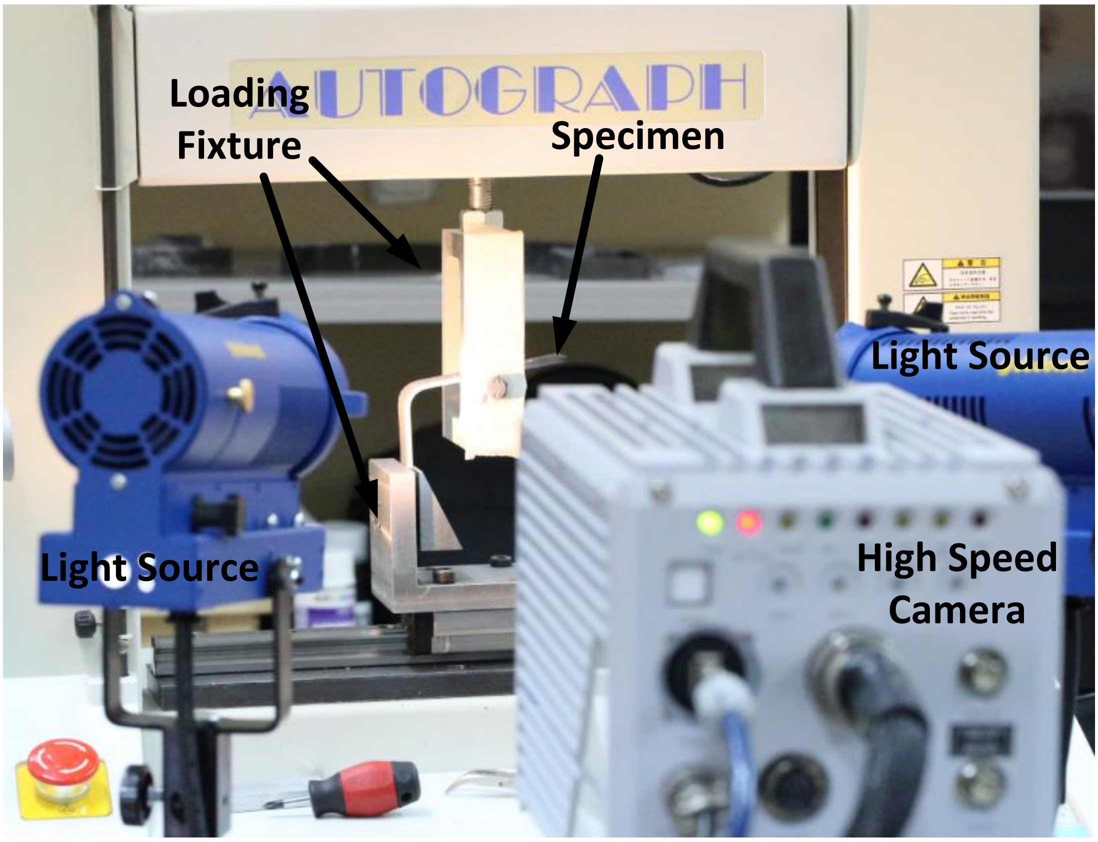

Figure 2.2 Ultra high speed imaging system and light sources

In this study, the full field technique of photoelasticity is employed to study the crack propagation along the curved interface of curved polycarbonate plates. The material is chosen as MAKROLON© polycarbonate which exhibits stress induced birefringence. Since photoelasticity provides full-field stress state and it is very sensitive for stress concentrations, the position of the crack tips are located by tracing the stress concentration along the curved interface. An overview of the photoelastic experimental setup is presented in Figure 2.3. The setup consists of monochromatic light source, diffuser plate, quarter wave plates, circular polarizer and analyzer, and Photron Fastcam SA5 high speed camera. The specimen and loading mechanism is placed between the polarizer and the analyzer plates and fringe patterns are captured using a Photron Fastcam SA5 High speed camera at 100,000-150,000 fps range.

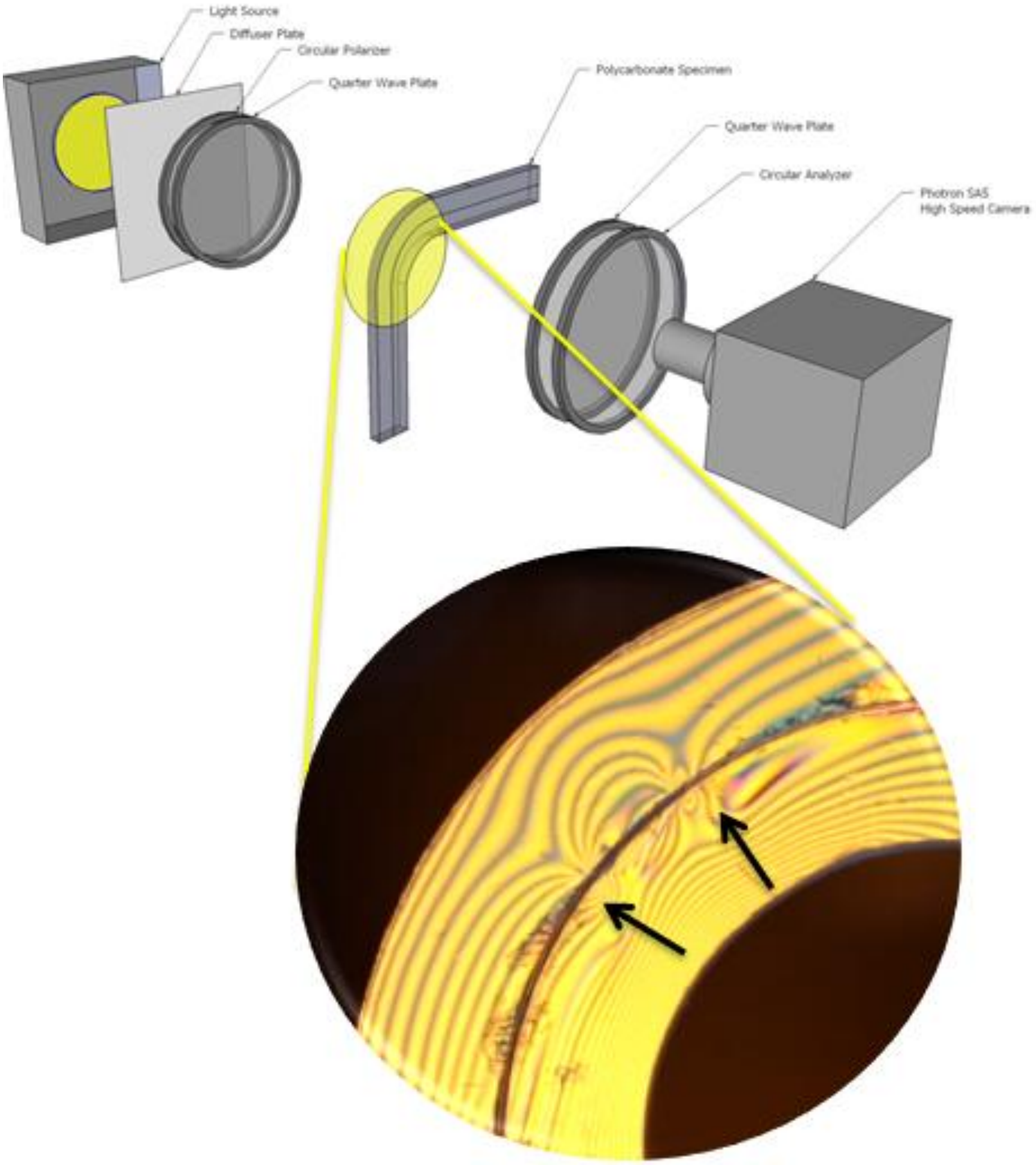

Figure 2.3 Photoelastic experimental setup and stress concentration in the crack tips.

CHAPTER 3

DYNAMIC FAILURE OF CURVED COMPOSITE BEAMS SUBJECTED TO QUASI-STATIC AXIAL LOADING

3.1 Introduction

In this chapter, finite element analysis with cohesive elements is used to investigate the effect of thickness and initial crack length on the delamination failure modes and delamination growth dynamics for unidirectional curved composite laminates subjected to loading parallel to one of the arms, namely shear loading (V). As in [10], delamination is allowed only in the center interface to isolate the phenomenon of dynamic crack growth occurring on a single weak interface. Transition of delamination failure mode is observed in which initial crack propagation at the corner is replaced by nucleation and growth of a secondary crack in the arm for a combination of larger thicknesses and smaller initial crack length. The crack tip speed is also observed to increase to that of the Rayleigh wave speed of the unidirectional composite laminate with thicker specimens and smaller initial crack lengths.

In the next sections, the finite element model and material analyzed are discussed. The results are presented for stress fringes, load-displacement behavior, and crack tip speeds for different thicknesses. This is followed by parametric studies for the effect of thickness and initial crack length on the delamination failure mode, maximum stress and maximum crack tip speeds.

3.2 Geometry and Material

The geometry and the dimensions of the unidirectional curved composite laminate are shown in Figure 3.1. The laminate thickness is varied from 3 to 6 mm, with two 10-mm long arms and an inner radius of 5 mm. The laminate is composed of 24 to 48 unidirectional plies of carbon fiber reinforced plastic with a ply thickness of 0.125 mm. The stacking direction is represented by the x1-axis that follows the laminate geometry and x3-axis is orthogonal to the direction of the plies as illustrated in Figure 3.1. An initial crack varying from 1 to 5 mm is inserted between the plies at the mid-line of the laminate at the middle of the curved region. The cohesive interface is defined on both sides of the initial crack. The location of the cohesive line at the middle of the laminate is justified by the fact that the maximum shear stress is attained at the right arm in the middle under parallel loading as shown in Gozluklu and Coker [10]. For the parametric studies, thickness is varied while the inner radius is kept constant and the crack location is kept at the center.

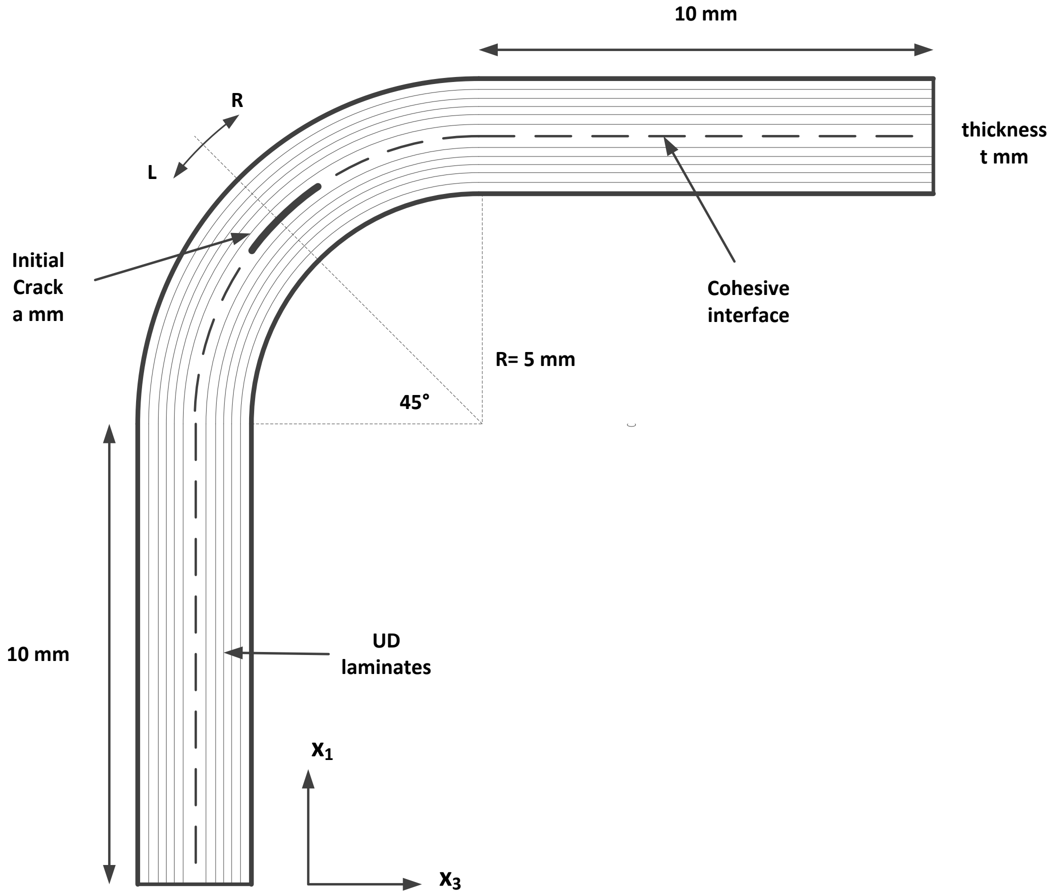

Figure 3.1 Geometry

The material and interface properties of CFRP are taken as the same as Gozluklu and Coker [10]. Table 3.1 gives the material properties and Table 3.2 gives the interface properties with subscripts I and II referring to Mode-I and Mode-II, respectively. The interface strengths are denoted by t_{ic} (i = I, II) and the fracture toughness values in each mode is denoted by G_{ic} (i = I, II). The curve fit factor, η and the penalty stiffness value, E_o for mixed mode energy relase rate calculation are also given in Table 3.2. The shear wave speed of the composite can be found from the material properties given in Table 1 by using $(G_{12}/\rho)^{1/2}$ where ρ is the density of the composite that is taken as 1600 kg/m^3. The shear wave speed of the CFRP laminate is calculated to be 1810 m/s and the Rayleigh wave speed is calculated to be 1740 m/s using calculation method explained in [14].

Table 3.1 Material properties for CFRP [10]

E_{11} (MPa)	E_{22} (MPa)	E_{33} (MPa)	ν_{12}	ν_{13}	ν_{23}	G_{12} (MPa)	G_{13} (MPa)	G_{23} (MPa)
138000	10000	10000	0.30	0.30	0.27	5240	5240	3930

Table 3.2 Interface properties [10]

t_{Ic} (MPa)	t_{IIc} (MPa)	G_{Ic} (N/mm)	G_{IIc} (N/mm)	B-K criterion constant (η)	Penalty Stiffness (MPa)
60	60	0.352	1.002	2.25	10^6

3.3 Finite Element Model and Boundary Conditions

The finite element model of the unidirectional curved composite laminate is shown in Figure 3.2. Mesh convergence and density analyses were conducted in [10], and the same values are used for this study. The mesh is uniform in the curved region and the arms, with elements having a height of 0.050 mm and a length of 0.025 mm that is also the length of the cohesive elements. Dynamic finite element analysis is carried out using ABAQUS/Explicit and the static analysis is carried out using ABAQUS/Standard. The same finite element model morphology is used for both analyses. However, the number of integration points in bulk elements is different between the two solvers due to the unavailability of element types in ABAQUS for the explicit solver [28]. Similar to the study of Gozluklu et. al. [10] the bulk element in explicit analysis is 4-node bilinear with single integration point at the centroid of the element having hourglass control (Element code in ABAQUS: CPE4R). On the other hand, the implicit solver uses full integration version where the integration points are located at the Gaussian integration points. Since there is no need to transfer internal variables in the bulk materials that are elastic, this does not cause a problem. The same cohesive elements are used for both analyses that are zero-thickness 4-node bilinear elements (COH2D4) with lumped integration scheme.

The boundary conditions are also shown in Figure 3.2. The curved laminate is clamped on the right edge, and the applied input load is a prescribed displacement, U, parallel to the lower arm. The shape of the displacement input starts with a smooth ramp and rises to its full value of 10 mm in 0.1s; if a smooth ramp is not used; harmonic oscillations [8] in the early stages of equilibrium curve occur. The stable time value used for explicit time integration is taken as $4.00\text{x}10^{-10}$ seconds, which is half of the stable time, calculated by ABAQUS [28].

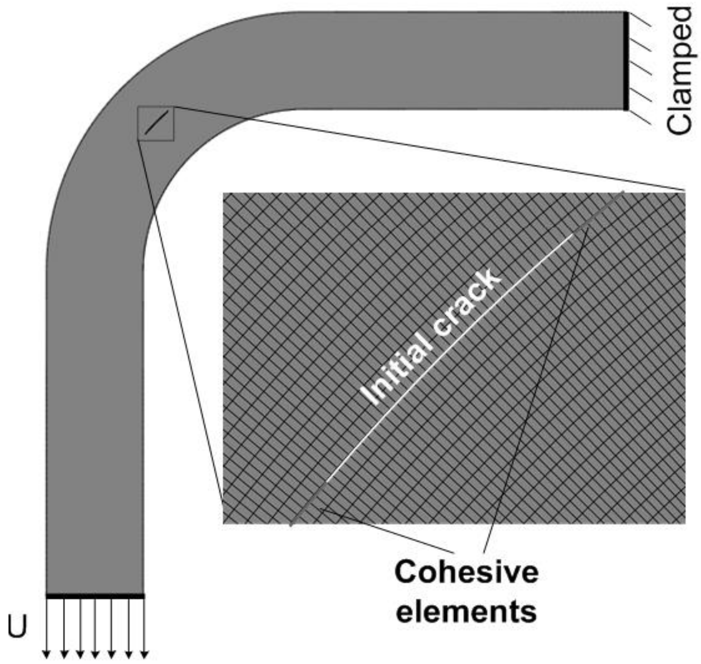

Figure 3.2 Finite element model and boundary conditions

3.4 Results

3.4.1 Thin Laminate: A Case for the Propagation of the Initial Crack at Moderate Speeds

Delamination process of a 3 mm thick curved laminate with a 1 mm initial crack located at the very middle of the curved region is simulated. The L-shaped laminate is loaded quasi-statically parallel to the lower arm, while the upper arm is clamped (Figure 3.2). The tip load versus tip displacement curve is given in Figure 3.3. Initially, the load rises linearly with displacement as the laminate deforms elastically until a value of 3.2 kN. After the load reaches this value, the initial crack starts propagating dynamically and the load reaches zero in a very short time period as the crack tip propagates to the end of the arm. The load displacement curve is not taken into consideration after the load reaches zero since contact between the plies is not modeled and spurious oscillations occur in the simulations. However the crack already completes its propagation before the load reaches zero. Therefore, the dynamic part of the crack propagation is simulated accurately, even though the simulations do not contain a contact model.

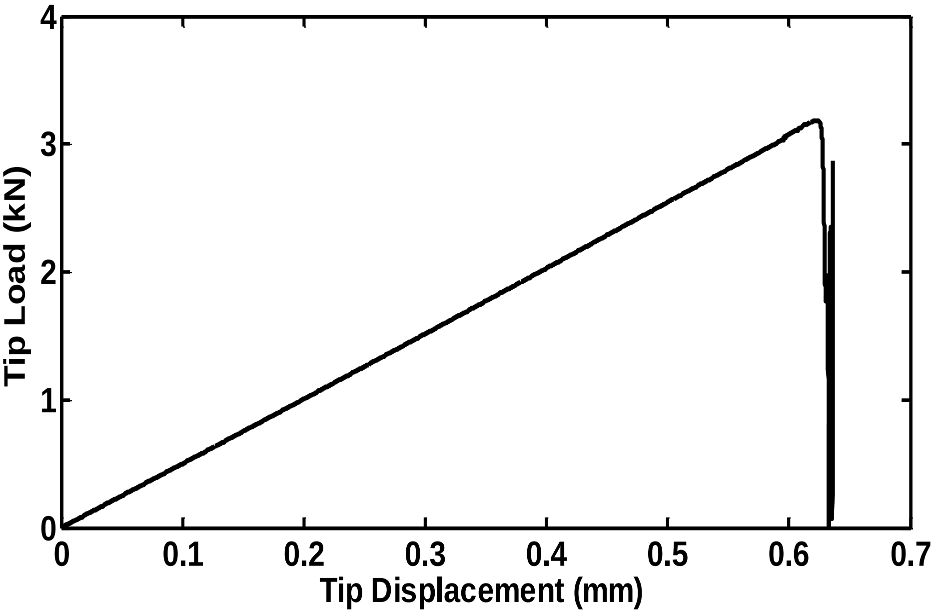

Figure 3.3 Load-displacement curve for a 3-mm thick laminate with an initial crack length of a= 1 mm.

The normal stress contours before and during the crack propagation are plotted at the load points (a), (b), (c), and (d) on the load-displacement curve in Figure 3.4. In the plots, light colors represent compressive stresses and dark colors represent tensile stresses. Point (a) corresponds to the state just before the crack starts propagating. Normal opening stresses due to bending reach their maximum value near the curvature in Figure 3.4 (a). At point (b), both ends of the crack propagate along the curved region and at (c) the crack tips travel along the arms. Finally, at point (d) both cracks have reached their maximum extent and are arrested.

In Figure 3.5, the left and right crack tip speeds are plotted with respect to the crack tip position from the initial crack. Both crack tips start propagating at the same speed of approximately 50 m/s through the curved region. During the transition of the cracks from the curved region to the arms, the right crack tip starts accelerating to 1250 m/s while the left crack tip continues traveling at much lower speed of less than 100 m/s during the whole process. Finally, the left crack is arrested at 7.5 mm whereas the right crack propagates almost to the end of the arm. As shown in Gozluklu et. al. [10], for loading parallel to the lower arm, the right crack tip propagates under shear stresses, whereas propagation of the left crack tip results from opening stresses. Our observations are consistent with the results of Coker et. al. [14] where they showed that interface cracks in composite materials can propagate at speeds close to the Rayleigh wave speed under shear dominated loading whereas mode-I cracks travel at much slower speeds

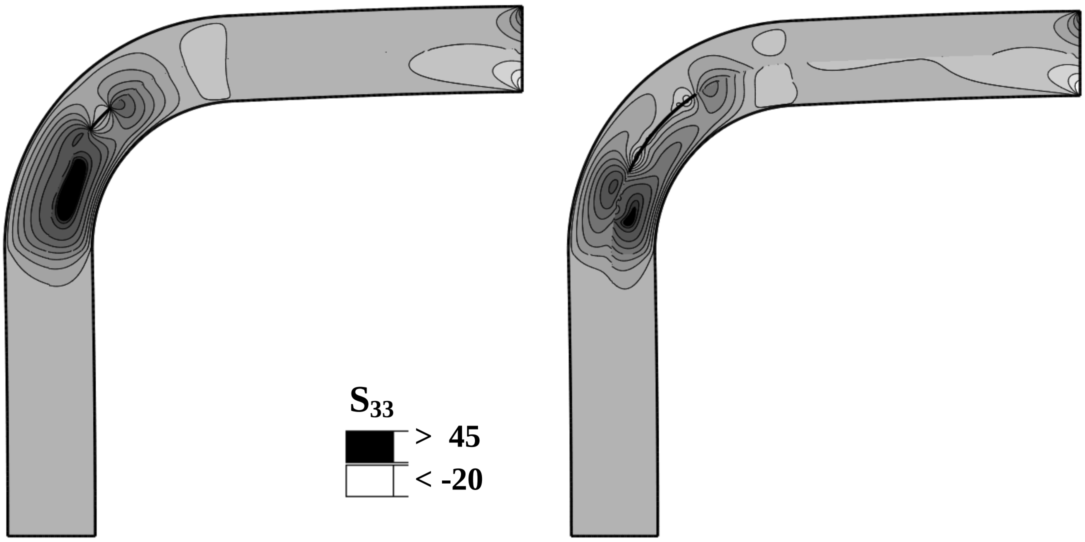

(a) t=- 270 μs, P=3.20 kN

(b) t=27 μs, P=3.08 kN

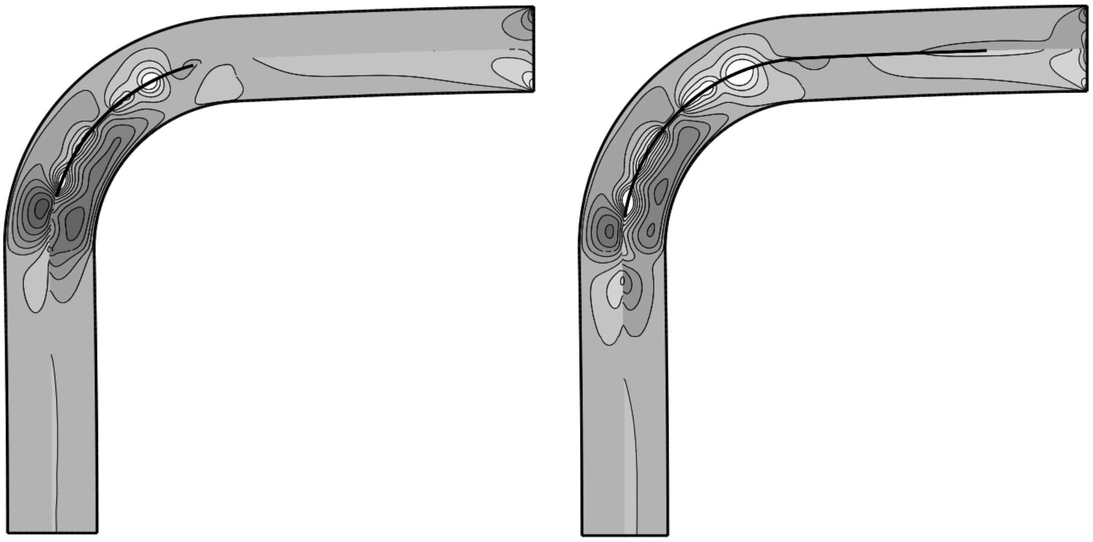

(c) t=50 μs, P=2.50 kN

(d) t=67 μs, P=2.08 kN

Figure 3.4 Snapshots of the normal (opening) stress contours for the 3-mm thick laminate with an initial crack length of a= 1 mm corresponding to points a, b, c, d on the load-displacement curve in Figure 3.3.

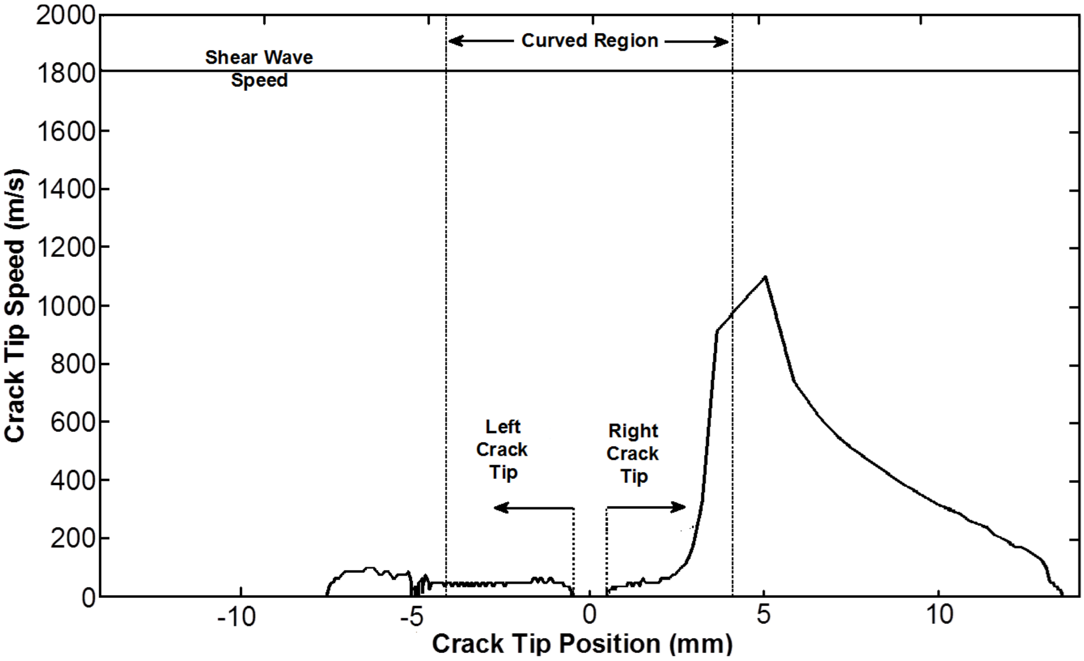

Figure 3.5 Crack tip speeds for the left and right crack tips for the 3-mm thick laminate with an initial crack length of a= 1 mm.

3.4.2 Thick Laminate: A Case for the Propagation of the Initial Crack at the Rayleigh Wave Speed

Delamination of a thicker 6 mm curved laminate with a 3 mm initial crack is simulated. In this case, when the tip load reaches 6.2 kN, the initial crack starts propagating rapidly, and failure occurs due to delamination resulting from propagation of the initial crack. Four snapshots of the radial opening stress contours during the failure process of the 6 mm thick curved laminate with a 3 mm initial crack are shown in Figure 3.6. The stress concentration at the crack tips before damage accrues prior to crack initiation at 130 μs is shown in Figure 3.6 (a). In Figure 3.6 (b), (c), and (d), the stress contours are shown at 6μs, 10μs, and 25μs after crack initiation, respectively. The right crack tip propagates along the curved region and into the upper arm whereas the left crack tip remains stationary. The maximum radial normal stress is near the inner curvature and decreases with the left crack tip stresses as the right crack tip grows. The left crack tip sees a compressive normal stress indicated by the white stress contours. The crack tip speed as a function of distance from the initial crack for both crack tips is plotted in Figure 3.7. The right crack tip speed reaches the Rayleigh wave speed of 1770 m/s at the end of the curved region and decelerates in the arm region to arrest at the end of the arm. This speed was calculated between two adjacent cohesive elements. On the other hand, the left crack tip travels at an average speed of 100 m/s under Mode-I loading for a short distance before arresting.

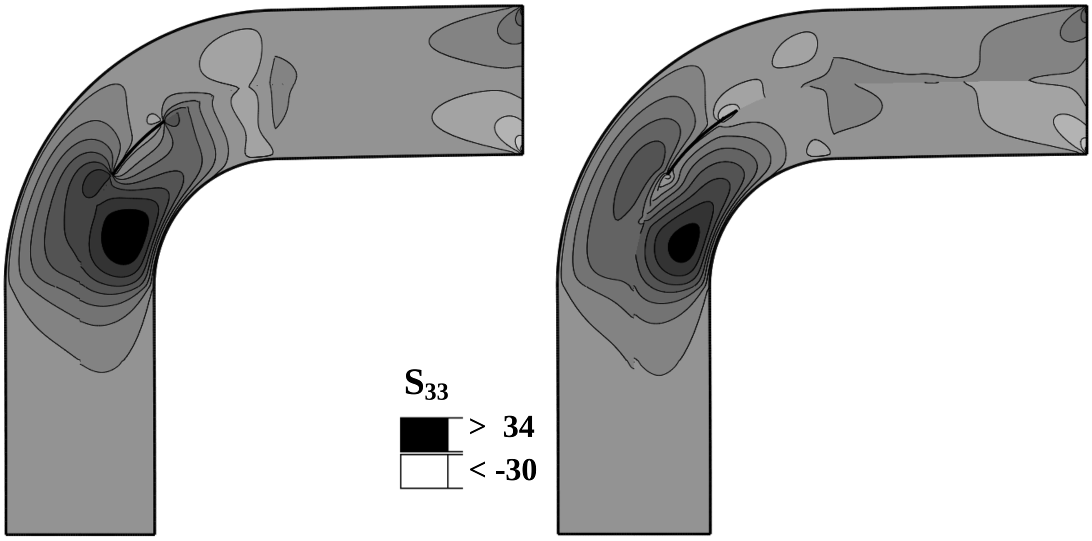

(a) t= -130 µs, P= 6.40 kN (b) t= 6 µs, P= 6.00 kN

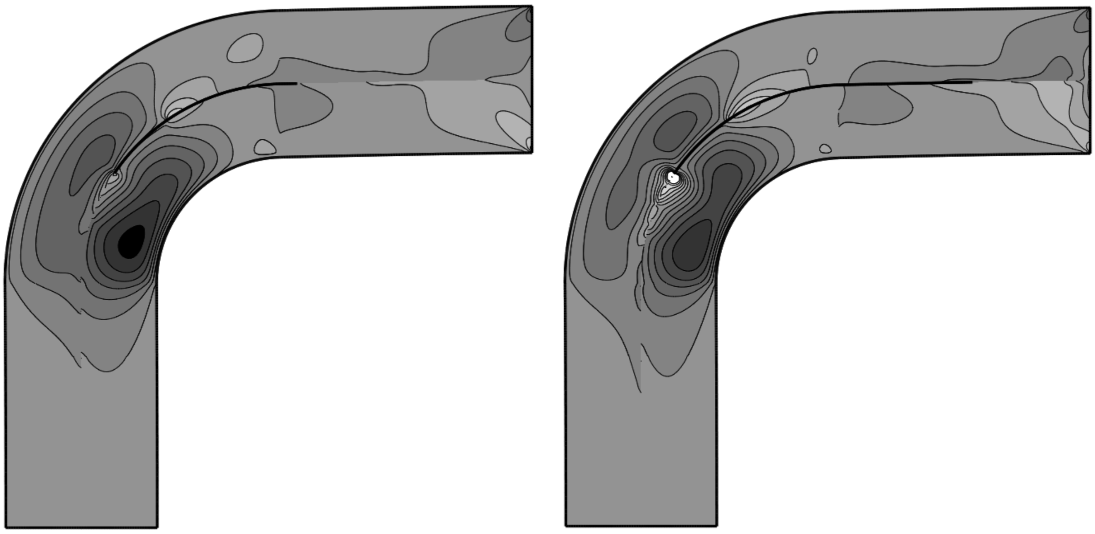

(c) t= 10 µs, P= 5.90 kN (d) t= 25 µs, P= 5.20 kN

Figure 3.6 Snapshots of the normal (opening) stress contours for the 6-mm thick laminate with an initial crack length of a= 3 mm at (a) t=-130 µs, (b) t= 6 µs, (c) t= 10 µs, (d) t= 25 µs with corresponding tip load values, P.

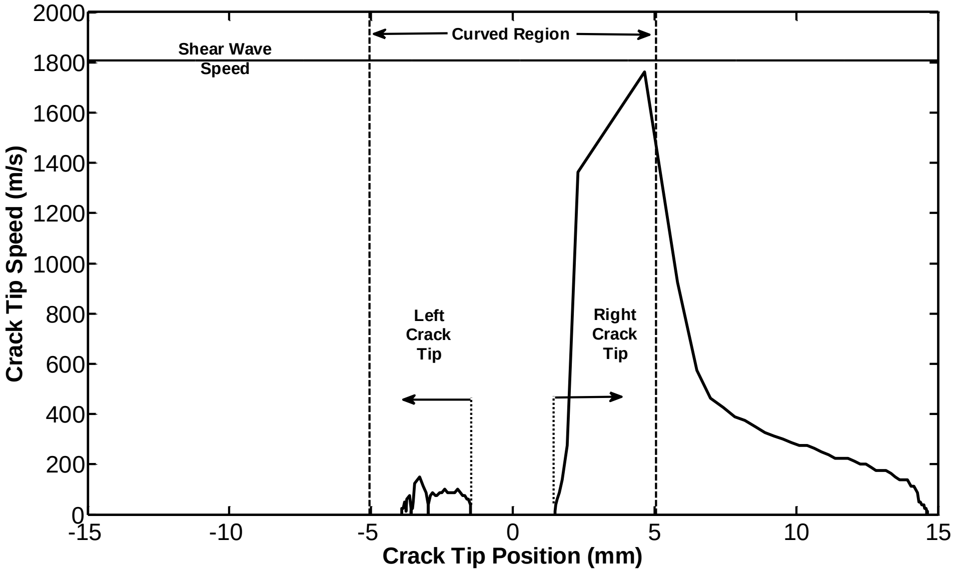

Figure 3.7 Crack tip speeds for the left and right crack tips of the 6-mm thick laminate with an initial crack length of a= 3 mm.

3.4.3 Thick Laminate: A Case for the Nucleation and Propagation of a Secondary Crack

The stress contours for the 6 mm thick curved laminate with a smaller initial crack length of 1-mm is shown in Figure 3.8. Figure 3.8 (a) shows the normal stress concentrations near the initial crack tips 100μs before the delamination failure process starts. During the loading, as the maximum load of 7 kN is reached, the shear stress concentration moves from the corner to the center of the horizontal arm. As shown in Figure 3.8 (b), a secondary crack nucleates in the center of the upper arm, relieving the stress near the initial crack tip. This occurs because both the shear stress and the damage parameter, d, reaches the critical value faster in the right arm then at the initial crack even though both of these parameters are initially higher at the tips of the initial crack as shown in Gozluklu et. al. [10]. Consequently, the secondary crack propagates in both directions (Figure 3.8 (b) and (c)). The left moving tip of the secondary crack finally coalesces with the initial crack as shown in Figure 3.8 (d).

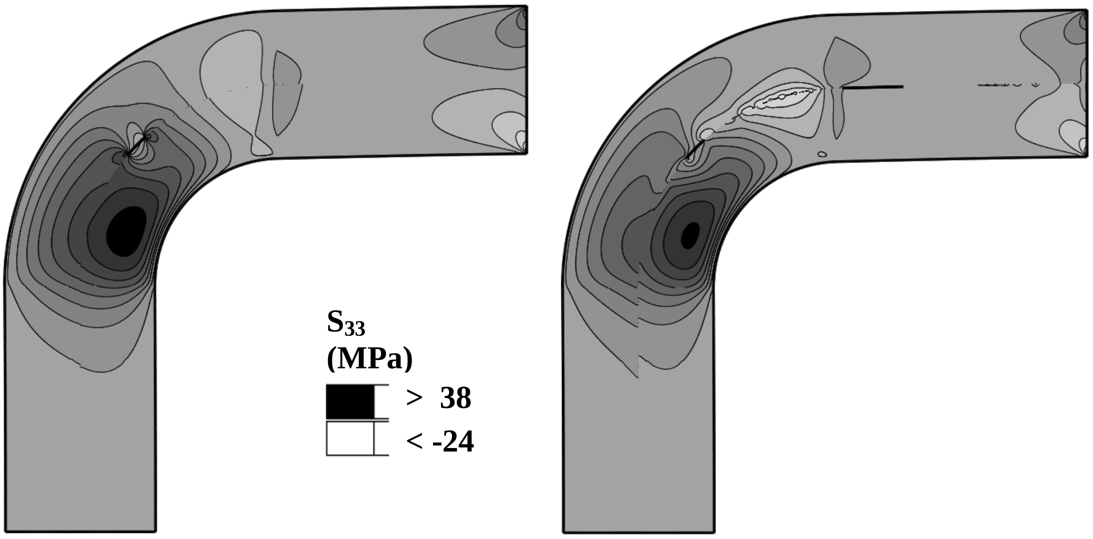

(a) t= -100 μs, P= 7.00 kN (b) t= 1 μs, P= 6.73 kN

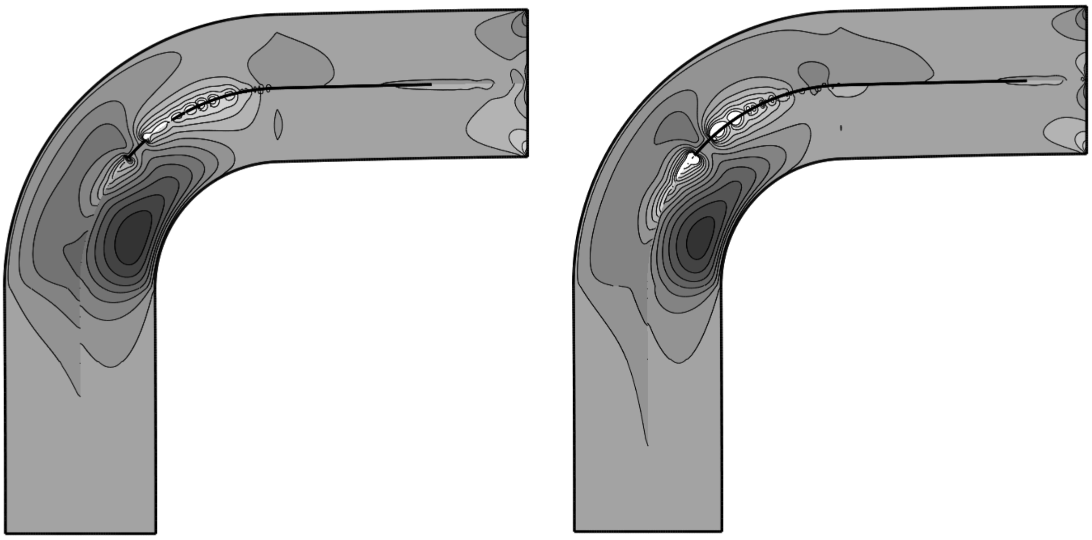

(c) t= 12 μs, P= 6.40 kN (d) t= 22 μs, P= 5.82 kN

Figure 3.8 Snapshots of the normal (opening) stress contours for the 6-mm thick laminate with an initial crack length of a= 1 mm at (a) t= -100 μs, (b) t= 1 μs, (c) t= 12 μs, (d) t= 22 μs with corresponding tip load values, P.

3.4.4 Map of Delamination Failure Modes

Finite element simulations for different initial crack lengths and laminate thicknesses were carried out. The observed delamination failure modes together with the maximum loads and maximum speeds were recorded. A summarizing schematic of the delamination failure modes of L-shaped composite laminates under parallel loading are shown in Figure 3.9. In all cases, the failure starts from an initial crack at the corner (initial state) and ends in a fully developed delamination in the horizontal arm (final state) as shown in Figure 3.9. However failure process itself occurs in three different modes in between the initial and final states. The first failure mode is the propagation of the initial crack, which is the expected failure mode in design applications (Type 1). In this case, both the maximum load and the maximum crack tip speed increases with thickness. Generally, these structures are strengthened by adding more plies to increase the thickness. However, as the thickness is increased, a second failure mode is observed in which a new crack is nucleated in the arm and propagates throughout (Type 2). In the third mode, both the initial crack and a secondary nucleating crack propagate simultaneously. These three modes of failure are observed in curved composite laminates depending on the thickness and the initial crack length combinations as discussed next.

3.4.5 Maximum Tip Loading and Initial Crack Length

Simulations for initial crack length changing from 0 to 8 mm and laminate thickness changing from 3 to 6 mm were carried out. Maximum tip load as a function of initial crack length is shown in Figure 3.10. The maximum load is seen to decrease with increasing initial crack length as expected. Circles represent the cases in which the failure mode is in the form of the initial crack propagating (Type 1). In this case, Triangles represent the failure mode case in which a secondary crack is formed and propagates to join with the initial crack (Type 2). Where there is overlapping triangles and circles, both propagation modes are observed (Type 3). As the initial crack length is decreased, the failure mode changes to a secondary crack nucleation mode. Below a certain critical initial crack length, the maximum load is independent of the crack length for each thickness. This critical crack length is a linear function of the thickness. As the thickness is increased, the initial crack length for the transition increases, from an initial crack length of 1-mm for the 3-mm thick laminate to initial crack length of 2-mm for the 6-mm thick laminate.

Figure 3.10 is replotted in Figure 3.11 in terms of maximum applied stress (calculated by dividing the maximum load by the thickness) as a function of crack length normalized with respect to thickness, a/t. Below a value of a/t=1, the curves collapse into a narrow band of a sigmoid curve. The curves increase with decreasing a/t reaching a maximum value around 1.15 MPa at a/t=0.4. Although the maximum stress is expected to further increase with decreasing a/t, it remains constant at 1.15 MPa. This critical a/t value is also the point at which transition from secondary crack growth region to initial crack growth region occurs and is found to be independent of thickness. Thus, for all thicknesses modeled in this paper, the applied stress required to initiate a secondary crack is found to be a constant. On the other hand, the applied stress required to propagate a corner initial crack (type 1) decreases almost linearly with increasing a/t which is the expected case.

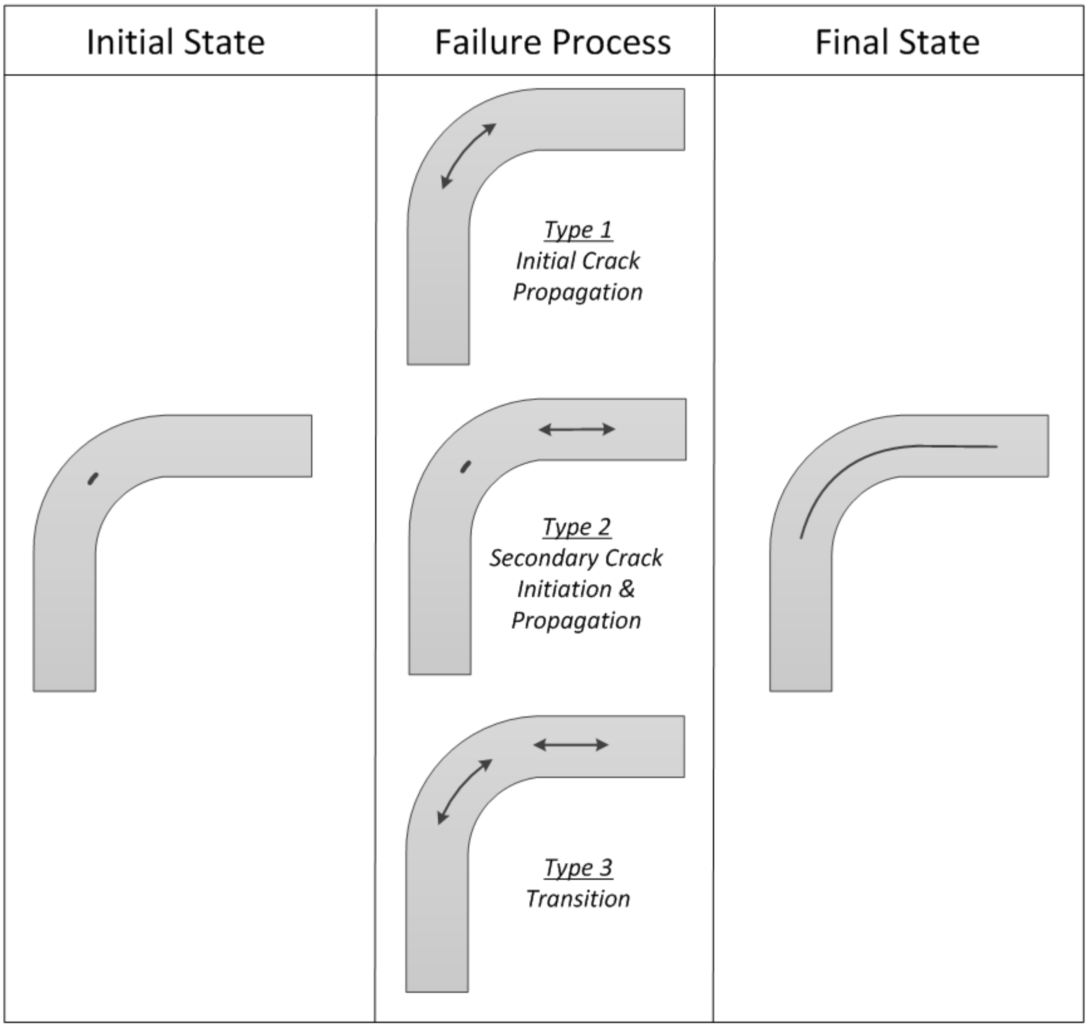

Figure 3.9 The failure map that summarizes the failure modes of the curved composite laminates subjected to quasi-static axial loading.

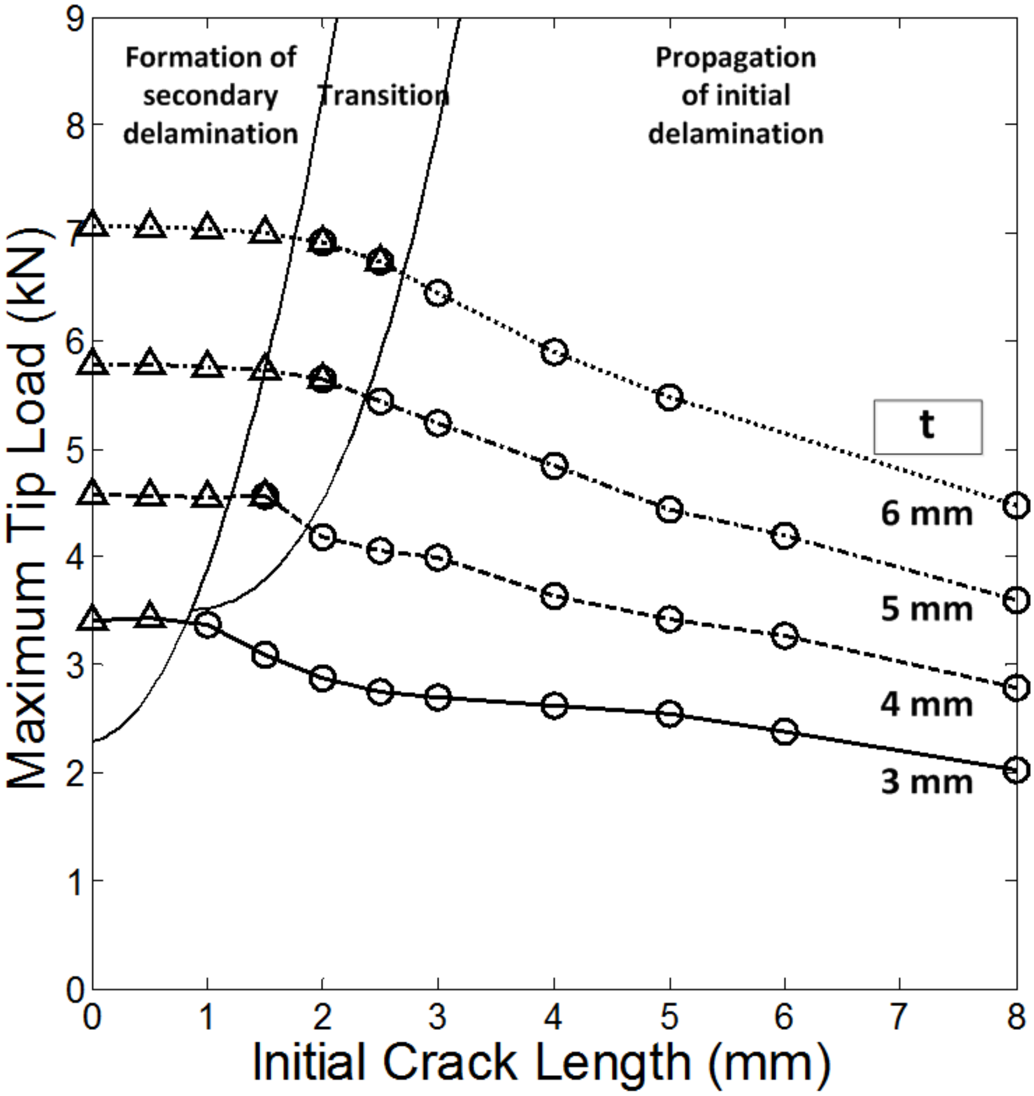

Figure 3.10 Maximum failure load as a function of initial crack length for different thicknesses ranging from 3-mm to 6-mm.

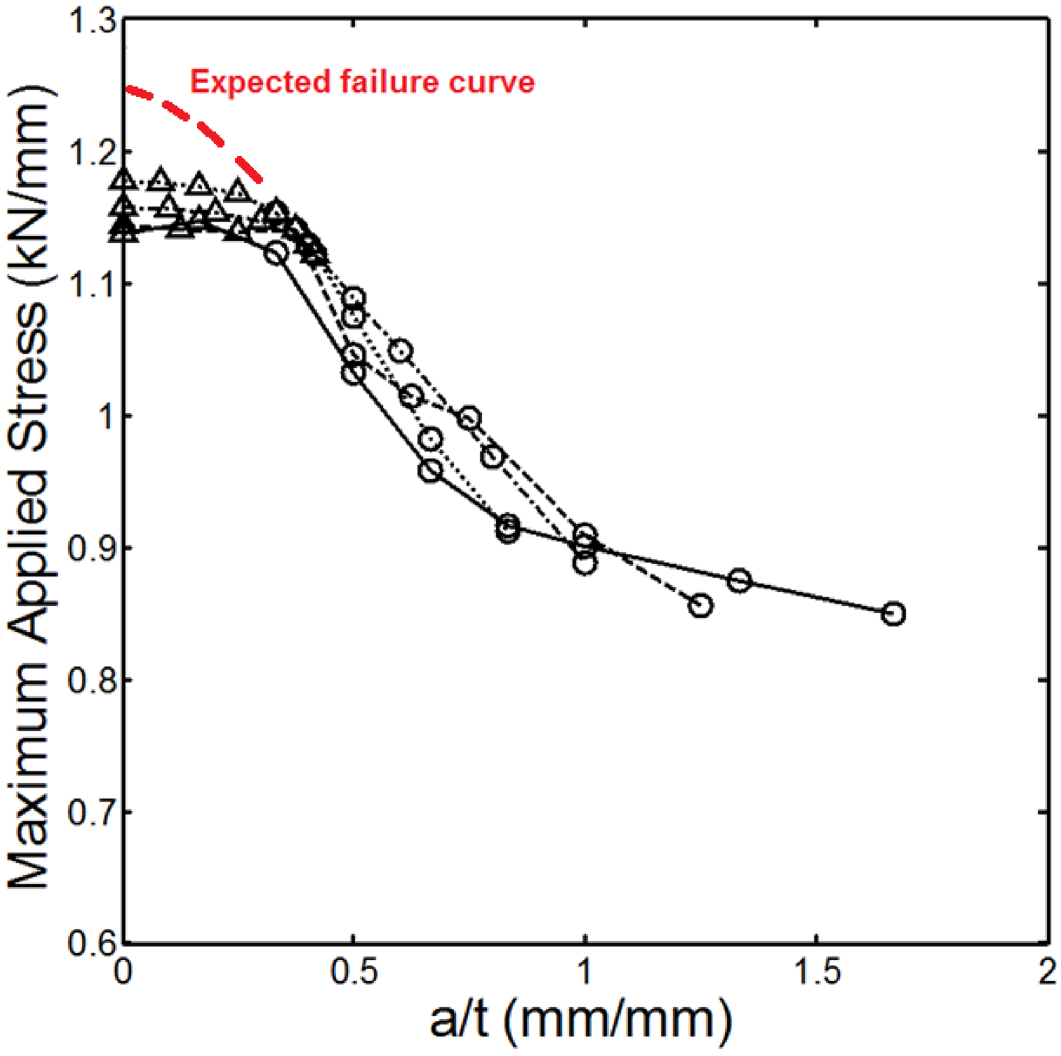

Figure 3.11 Maximum failure stress as a function of normalized initial crack length (a/t) for different thicknesses ranging from 3-mm to 6-mm.

3.4.6 Maximum Crack Tip Speeds for Initial Crack Propagation

The crack tip speed as a function of thickness is shown in Figure 3.12 for a fixed initial crack length of 3-mm which gives only Type-1 failure mode. For the cohesive law values used in this paper, the secondary crack mode initiates for all initial crack lengths in specimens thicker than 6mm. Left crack tip speed does not change significantly with thickness. However, the right crack tip speed increases exponentially to the Rayleigh wave speed of the material (1760 m/s) with thickness. As mentioned before, the maximum crack tip speed is always observed in the right crack tip which experiences shear dominated loading.

In Figure 3.13 (a), the maximum crack tip speed for the right crack as a function of the initial crack length is shown. Only cases (thickness and initial crack length) where failure occurs by the propagation of the initial crack are included. For all thicknesses, the maximum crack tip speed increases with decreasing initial crack length. In Figure 3.13 (b), the maximum crack tip speed normalized with respect to shear wave speed is replotted as a function of a/t^2 for different specimen thicknesses. As it can be seen, all plots collapse on a single curve in the new coordinate system. For all thicknesses, as a/t^2 decreases, the normalized crack tip speed increases and asymptotically approaches the shear wave speed of the composite laminate. This speed is not surpassed as the failure mode changes to that of a secondary crack mode for values lower than $a/t^2=0.1$.

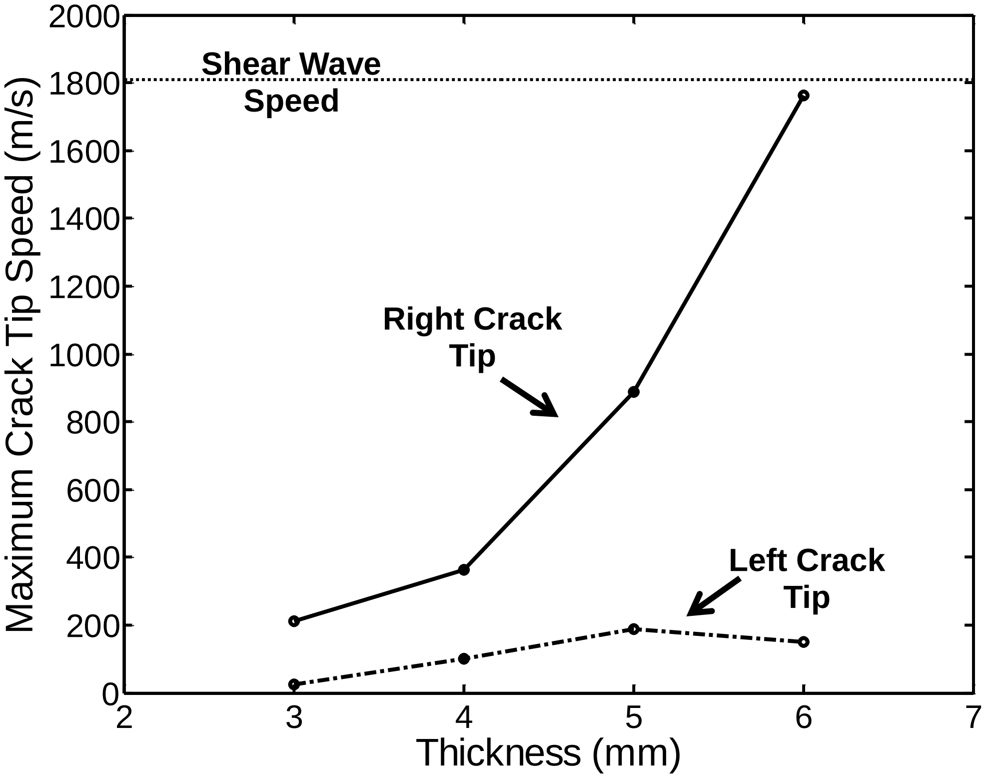

Figure 3.12 Maximum crack tip speeds for the left and right crack tips for laminate specimen thicknesses from 3-mm to 6-mm with an initial crack length of 3-mm.

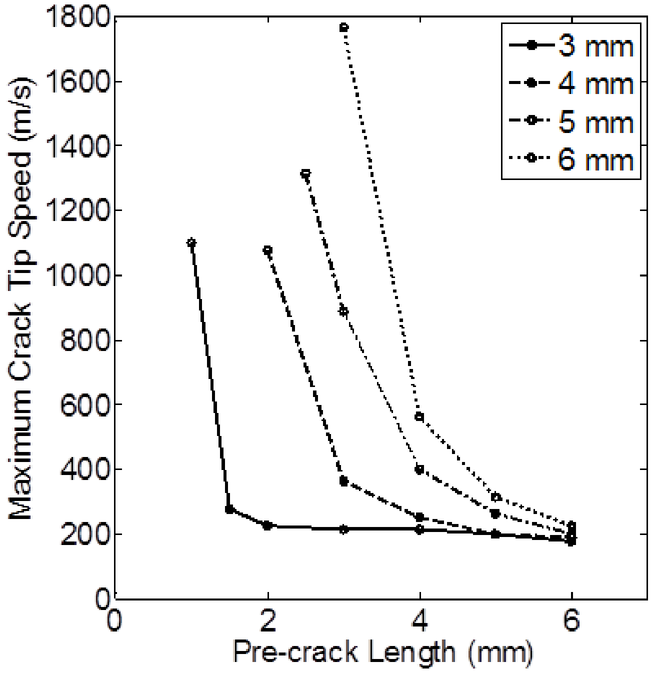

(a)

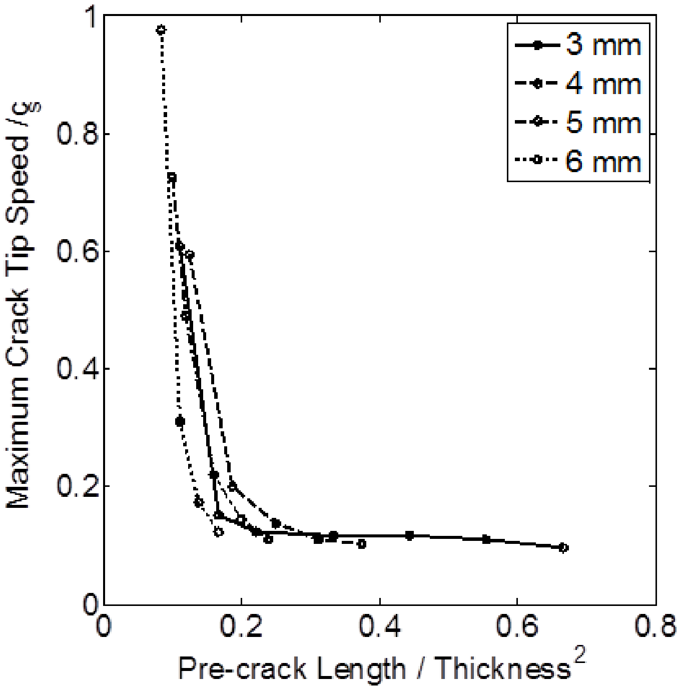

(b)

Figure 3.13 (a) Maximum crack tip speed with initial crack length for different thicknesses, (b) Maximum crack tip speed normalized with shear wave speed versus pre-crack size normalized by t^2 for thicknesses of 3-mm to 6-mm.

3.5 Conclusions

Finite element analysis in conjunction with cohesive elements is used to model the dynamic delamination of curved composite laminates subjected to axial loading. A sequential analysis method in ABAQUS® is used successfully in which explicit analysis follows static implicit analysis just before crack initiation. The cohesive zone model is a bilinear traction-displacement law and Ye's [22] criterion is used for crack nucleation. An initial crack is placed in the midline of the laminate at the center of curved region. The following conclusions are reached:

- Dynamic crack growth occurs under combined Mode-I and Mode-II loading.
- There are two distinct failure mechanisms for curved laminates under quasi-static axial loading. The first failure mechanism is the growth of the initial crack. The second failure mode is the formation and propagation of a secondary crack near the center of the clamped arm.
- Failure mechanism changes from corner crack growth to the secondary crack formation with thickness and initial crack length.
- All delamination failure under quasi-static axial loading is unstable for both failure mechanisms. Axial loading results in shear stresses together with compressive normal stresses at one crack tip.
- For initial crack propagation, the maximum load per thickness is a function of the normalized initial crack length and is found to be independent of the thickness for a/t < 0.4. The failure mechanism change occurs at a critical normalized crack length of a/t=0.4 for the material bulk and interface properties used in this study. This may indicate an inherent damage tolerance feature of curved composite laminates.
- For secondary crack nucleation, the tip load is independent of the initial crack length. The tip load per thickness is also independent of thickness.
- Shear dominated loading at the crack tip leads to very fast crack tip speeds reaching the Rayleigh wave speed of the laminate for thicker materials. This is the first observation of highly dynamic crack growth in curved composite laminates close to the shear wave speed of 1800 m/s. The Rayleigh wave speed is never surpassed due to the transition to secondary crack mode.

Below a normalized critical crack length of 0.4, the existence of the initial crack does not affect the strength since a secondary crack is formed. In other words, the strength cannot be increased once the secondary crack begins to be nucleated in the arm as shown in Figure 3.11. Therefore, we can state that small cracks less than a/t=0.4 that enable the formation of a secondary crack is inherently tolerated by the structure. This tolerance can be defined to be damage tolerance of corners. Such small cracks could be formed during manufacturing. Therefore, it is important to know that there might be no requirement to have a defect-free curved composite laminate since small corner cracks do not affect the strength. Thus, knowing that the secondary failure initiates at the arm, the effect of the initial crack length can be disregarded for small initial cracks during the assessment of structural safety. On the other hand, in planar structures, there is no known inherent damage tolerance capacity as a result of the geometrical features similar to the curved laminate case. From the design point of view, this leads to less conservative design since maximum load for crack initiation at the bend is higher than that required for secondary crack formation. Thus the existence of a delamination failure mode transition will have significance for strength calculations and industrial applications of curved composite laminates.

CHAPTER 4

DYNAMIC FAILURE OF CURVED COMPOSITE BEAMS SUBJECTED TO QUASI-STATIC SHEAR LOADING

4.1 Introduction

In this chapter, experimental study and observations on dynamic failure of unidirectional curved composite laminates under shear loading are presented. In previous studies [3, 4, 5, 6, and 7], although the existence of unstable crack growth in the curved composite laminates is presented, initiation and growth steps of the crack are not clearly showed experimentally. In this study, the use of high speed imaging techniques enables to capture whole dynamic process during initiation and growth of the crack on the curved region. Hence this observation gives opportunity to measure the crack propagation speed along the curved interface of unidirectional curved composite laminates under shear loading. In addition, even though the effect of initial crack length existing on curved region on the crack growth stability is analyzed numerically by Wimmer et. al. [5], this effect is not investigated experimentally. In this chapter, the effect of initial crack length, which is intentionally placed in the curved region of the curved composite laminate, on the stability of crack growth is also investigated experimentally.

4.2 Experimental Framework

4.2.1 Material and Specimen Geometry

Manufacturing of curved unidirectional composite specimens is carried out using hand lay-up technique. Right angled male tool is used for manufacturing process. Before the lay-up process the tool is cleaned using Loctite Frekote 770-NC release agent to prepare the tool for lay-up process. HexPly® AS4/8552 UD carbon prepregs having 0.18 mm cured thickness are laid up using right angled male tool. The specimens with thicknesses of 3 and 5 mm consist of 17 and 28 plies respectively. The ply-up orientation is arranged as [0°] for all layers. Teflon tape with thickness of 0.8 mm is placed at mid-layer of the specimens in order to mimic initial crack on the curved region (Figure 4.1 (a) and (b)). Table 4.1 shows the mechanical properties of the AS4/8552 lamina.

Table 4.1 AS4/8552 Lamina Properties

E_{11} (GPa)	E_{22} (GPa)	E_{33} (GPa)	$\nu_{12}=\nu_{13}=\nu_{23}$	G_{12} (GPa)	G_{13} (GPa)	G_{23} (GPa)
135	8.5	8.5	0.29	4.2	4.2	4.2

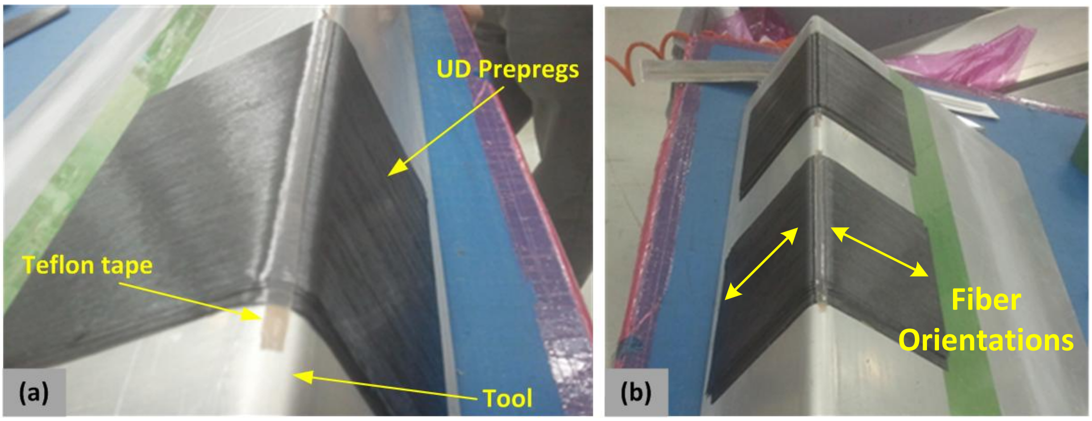

Figure 4.1 (a) Right angled tool for manufacturing, unidirectional pre-pregs, and Teflon tape used to mimic corner delamination, (b) overview of the specimens after lay-up is completed

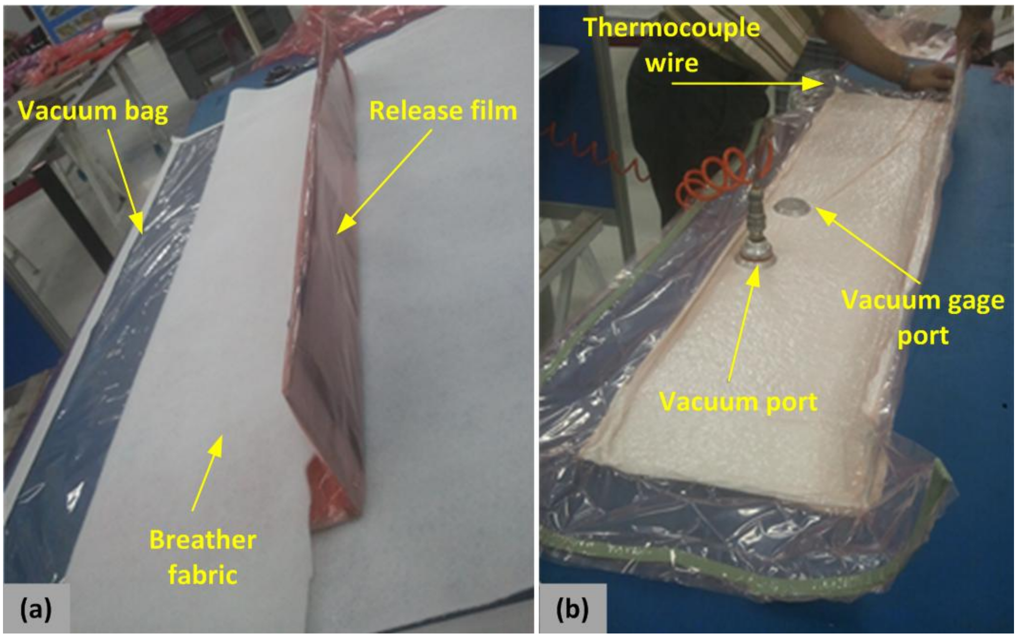

Figure 4.2 (a) Vacuum bagging process: use of vacuum bag, breather fabric, and release film, (b) After vacuum bagging process: use of vacuum port, vacuum gage port, and thermocouple wire.

When the lay-up process is finished, the mold with specimens is wrapped with release film, breather fabric, and vacuum bag respectively (Figure 4.2 (a)). Vacuum and thermocouple ports are inserted into vacuum bag before the bag sealant tape is closed. The bag is vacuumed to 21 mm-Hg and it is ready for curing process (Figure 4.2 (b)). The thermocouple wire and vacuum gage port are used during curing process to measure and control the temperature and pressure respectively.

Specimens in the vacuum bag are sent to autoclave for curing process. The autoclave is pressurized to 6.9 bar at the room temperature, then the temperature is increased to 180 °C with rate of 0.5-3.0 °C/min at the constant pressure. The specimens are cured in autoclave for 180 minutes at the temperature of 180 °C and pressure of 6.9 bar. Finally the temperature is decreased to room temperature with the rate of 0.5-3.0 °C/min, while the pressure is decreased gradually. The temperature and pressure change during whole curing process is shown in Figure 4.3. The total curing time is approximately 10 hours.

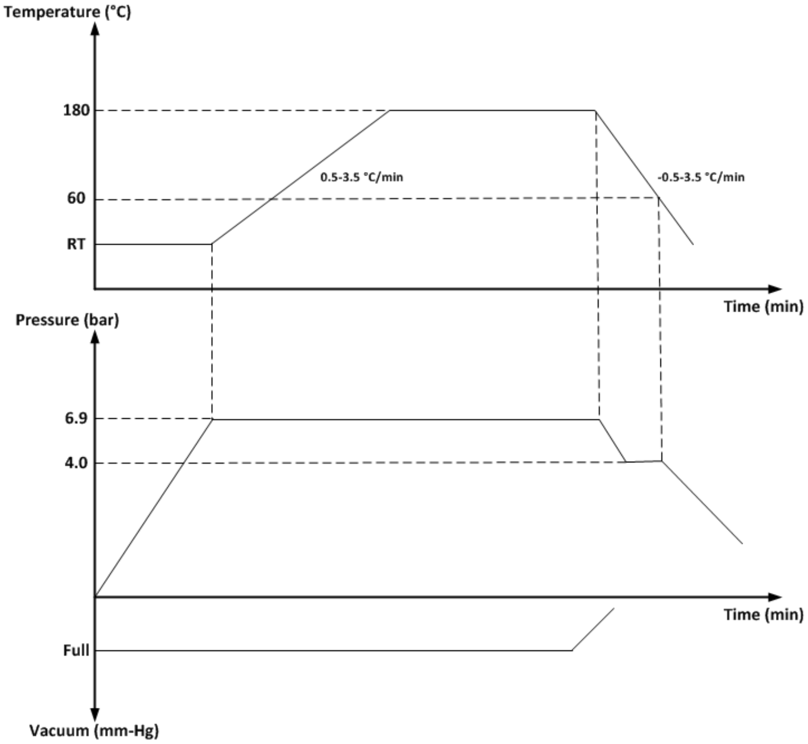

Figure 4.3 Temperature and pressure treatment in autoclave process

After autoclave process the cured curved composite laminates are cut into specimen dimensions shown in Figure 4.4 (a) using a diamond saw blade. The fiber orientation within the specimen is shown in the micrograph of the specimen for two different sections (Figure 4.4 (b)). Before the experiments one side of the specimens are painted with white paint as shown in order to clearly observe delamination initiation and growth.

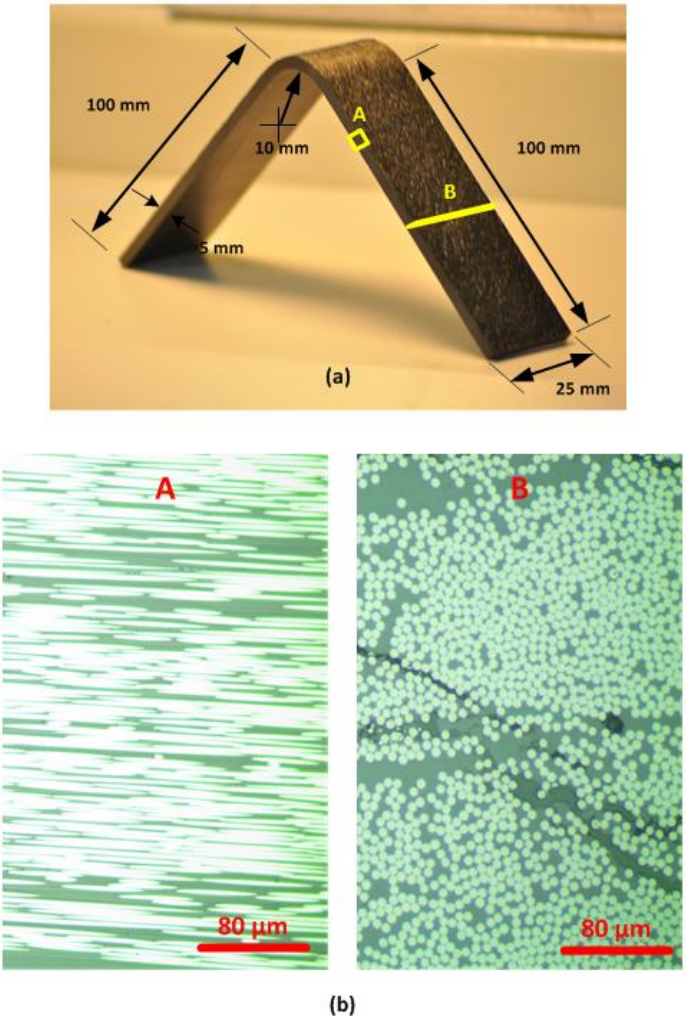

Figure 4.4 (a) Specimen geometry for 5 mm thick curved beam, (b) micrograph of the specimen for A and B sections.

4.2.2 Loading Fixture and Procedure

Unlike the loading fixtures used in the literature, a unique loading fixture is proposed to apply pure shear loading (V) to one of the arms of the specimen. Figure 4.5 show the schematic view of the loading fixture. The loading fixture has a sliding part in the lower arm which enables to remove axial reaction force at the upper arm of the specimen. In addition, the upper arm is free to rotate around z-axis in order to get rid of moment reaction at the upper arm.

The experiments are conducted using Shimadzu Autograph AGS-J series 10kN screw-driven tensile-compression testing machine. Testing machine is controlled remotely using a computer. All tests are performed at a cross-head speed of 4 mm/min at the room temperature while the machine load and upper fixture displacement are measured. The quasi-static shear loading is introduced to the upper of the specimen using proposed loading fixture. The application point of loading and the clamping distance are given in Figure 4.5.

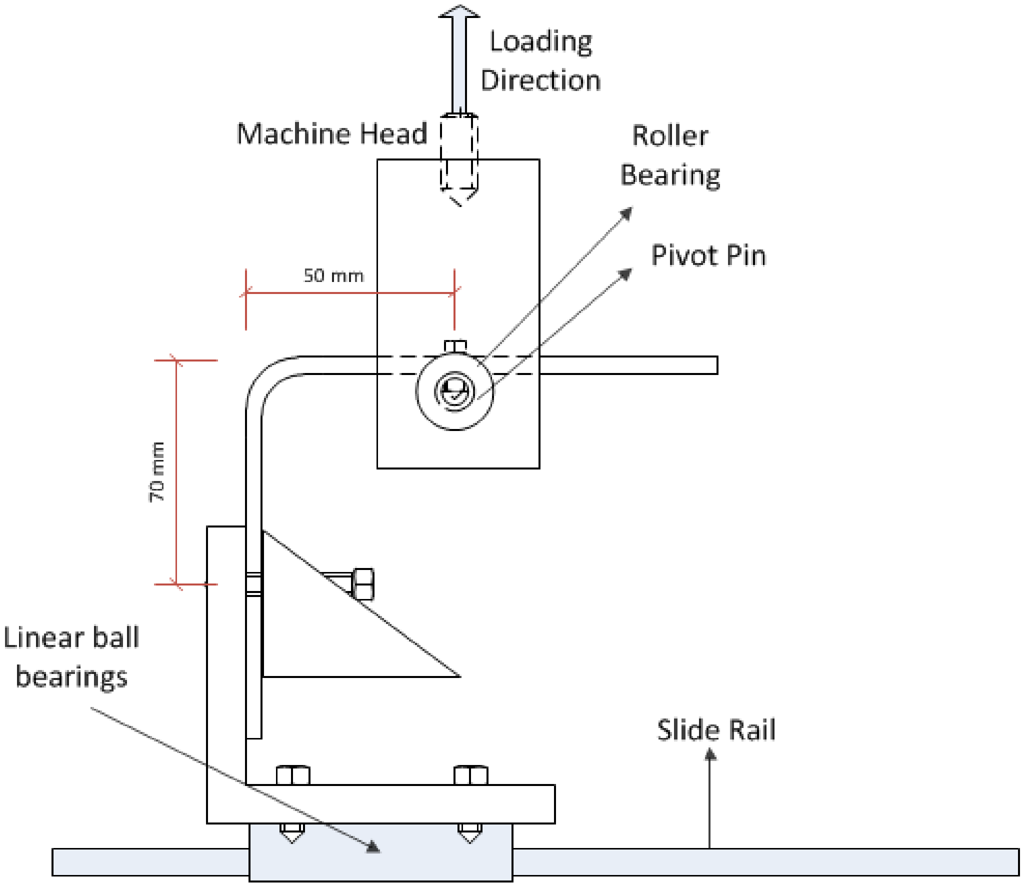

Figure 4.5 Loading fixture for curved composite laminates

4.3 Results

4.3.1 The Effect of Initial Crack Length on the Crack Growth Stability

Experiments on 3 mm, 6 mm, 9 mm, and 12 mm pre-cracked specimens with thicknesses of 3 and 5 mm were conducted. The two stability regimes depending on the initial crack length were observed in the load displacement curves obtained for 3 mm and 5 mm thicknesses (Figure 4.6 and Figure 4.7). For both specimen thicknesses, a large and sudden load drop in the load displacement curves is observed for 3 mm, and 6 mm pre-craked specimens. Whole crack propagations process is completed during this sudden load drop in a very short time interval. This indicates that crack growth is dynamic and unstable for smaller pre-cracked specimen. On the other hand, small load drop with a stiffness change in the load dipalacement curves is obserevd for 9 mm and 12 mm pre-cracked specimens. Each small load drops correspond to a small crack growth. Thus crack can complete its propation after a couple of small load drops. This implies that crack growth is quasi-static and stable for smalle pre-cracked specimens.

4.3.2 Crack Propagation Speed

Unstable and dynamic crack initiation and propagation is captured by Photron Fastcam SA5 high speed camera. Figure 4.7 shows the initiation and propagation of crack observed in a specimen having no initial crack. The pictures are captured at the 700,000 fps and there is a time interval of 1.42 μs between each frame. Crack dynamically initiates very near the mid-layer of the specimen and propagates along the same interface.

The pictures captured by high speed camera are analyzed by image processing and the crack tip position is obtained for each frame. The crack tip speed is calculated numerically with central differentiation method using crack tip positions. The crack tip speed as a function of time is shown in Figure 4.8. It shown that crack sub-sonically propagates and crack propagation speed is in the order of the shear wave speed.

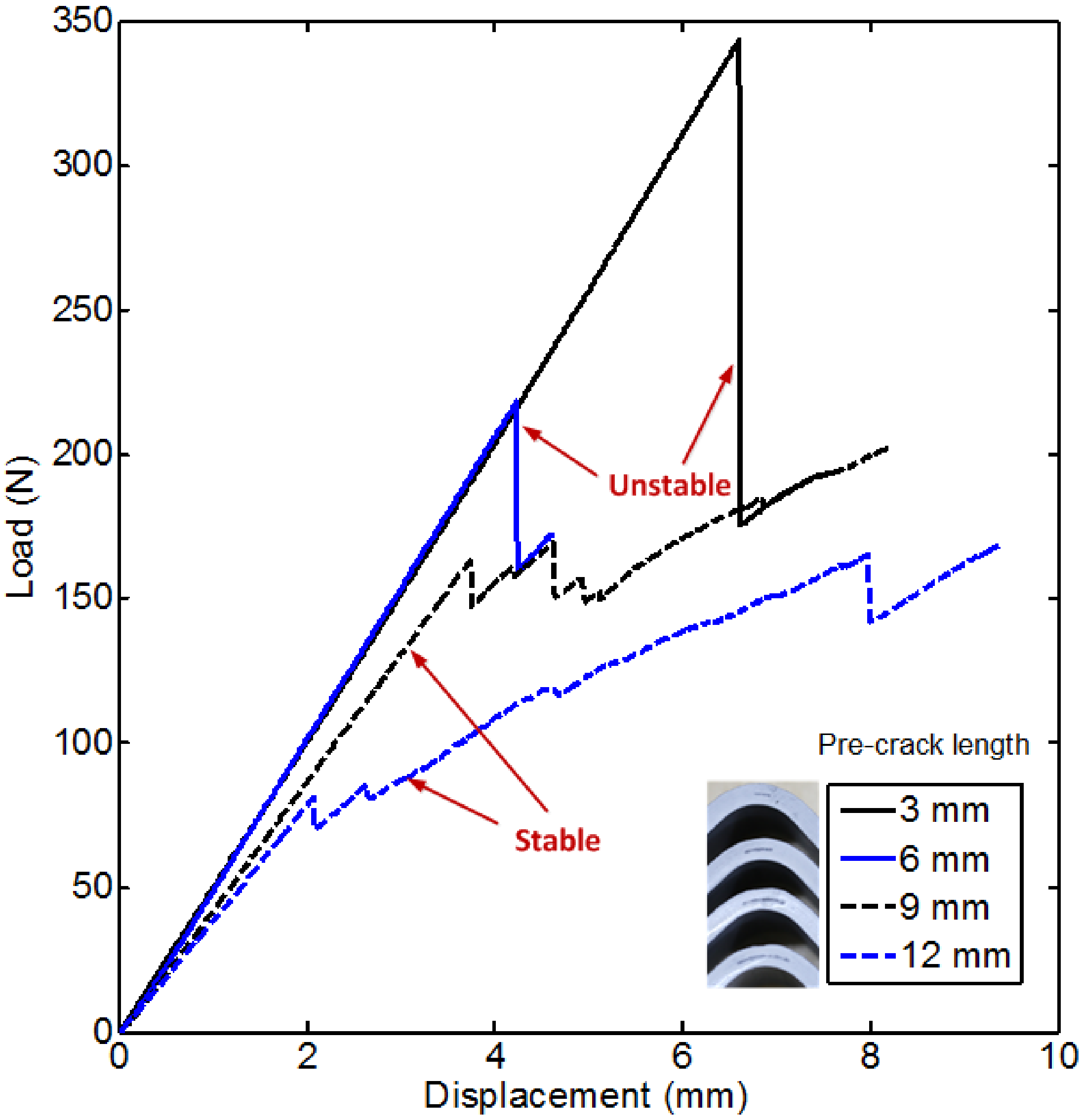

Figure 4.6 Load displacement curves for 3 mm, 6 mm, 9mm, and 12 mm pre-cracked specimens with a thickness of 3 mm.

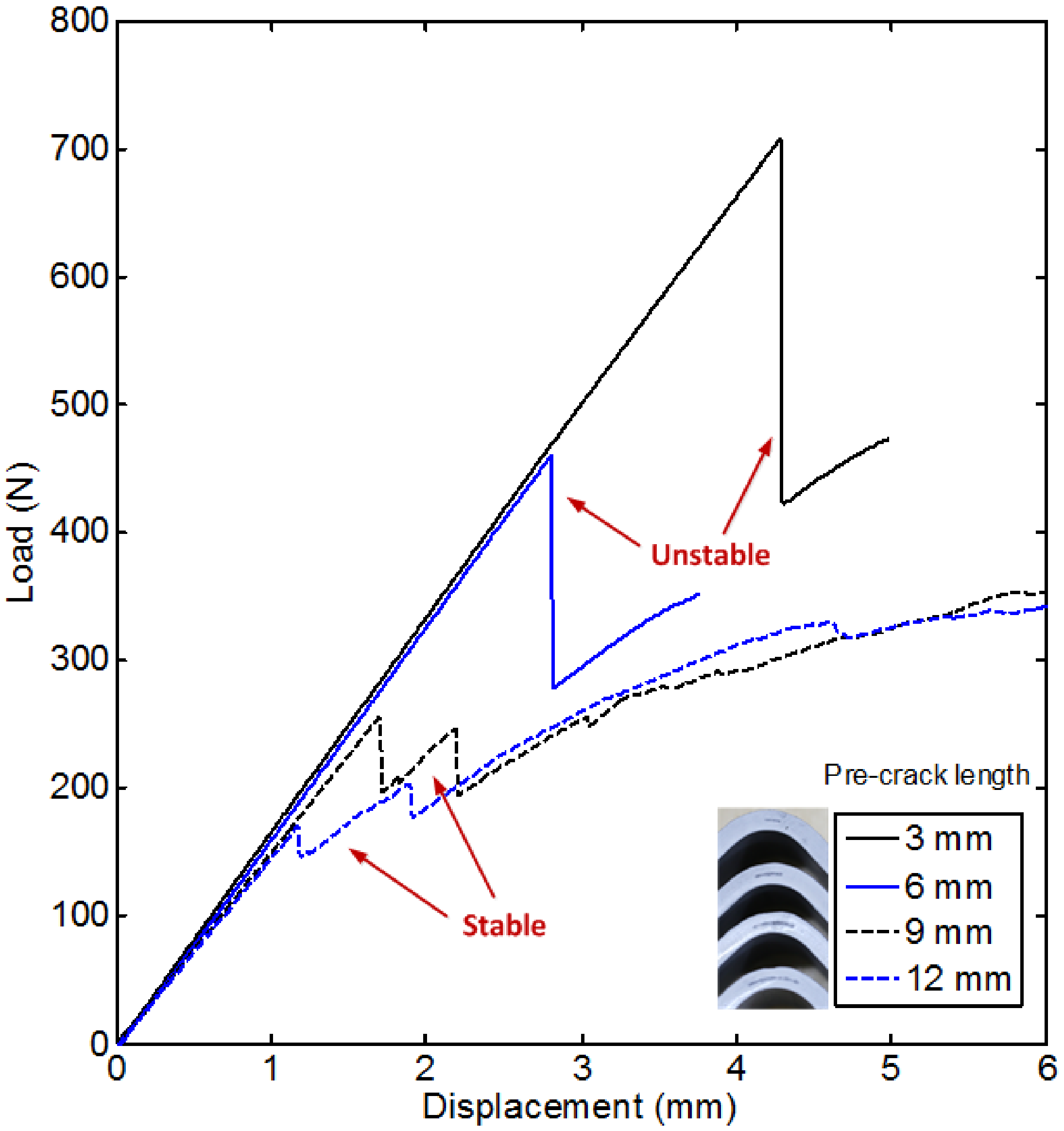

Figure 4.7 Load displacement curves for 3 mm, 6 mm, 9mm, and 12 mm pre-cracked specimens with a thickness of 5 mm

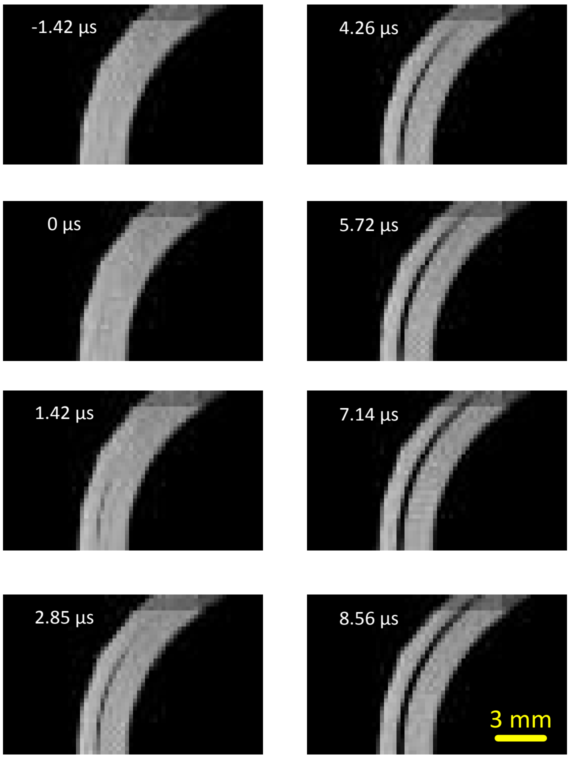

Figure 4.8 Crack propagation captured by Photron Fastcam SA5 high speed camera

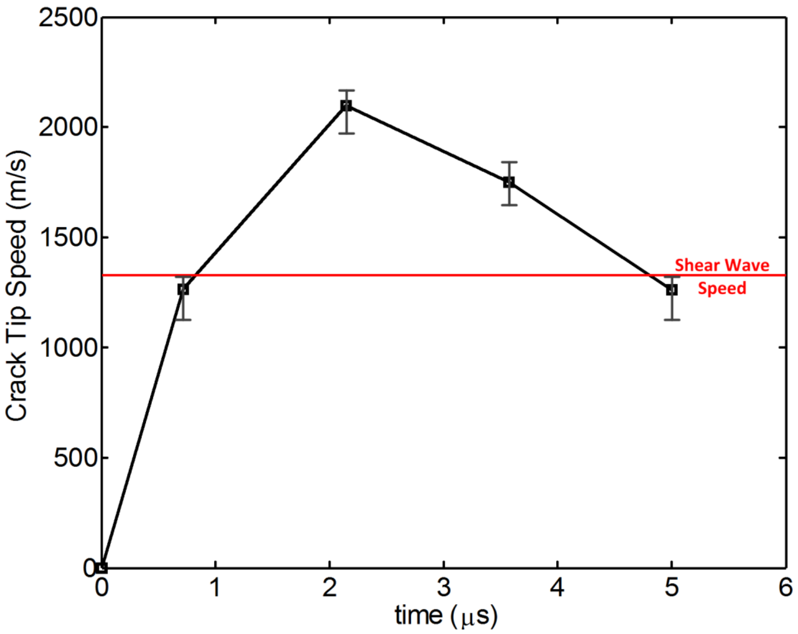

Figure 4.9 Crack propagation speed calculated using pictures captured by high speed camera

4.4 Conclusions

In this chapter, the behavior of dynamic delamination in unidirectional curved composite laminates under quasi-static shear loading is experimentally investigated. Curved composite laminate specimens are manufactured and tested under shear loading. A unique loading fixture is designed and manufactured to apply pure shear loading to the specimens. Unidirectional curved composite laminate specimens having initial crack in different lengths are manufactured. Dynamic delamination is captured using Photron Fastcam SA5 ultra high speed imaging system. The following conclusions are reached:

- Crack dynamically initiates near the mid-layer of the curved composite specimen and propagates along the same interface.
- Crack growth speed is in the order of the shear wave speed of the material.
- Crack growth in curved composite laminates under shear loading can become stable depending on the initial crack length.
- Smaller pre-crack lengths result in unstable crack growth.
- Larger pre-crack lengths result in stable crack growth.

CHAPTER 5

DYNAMIC FAILURE OF CURVED INTERAFCES IN POLYCARBONATE BEAMS SUBJECTED TO QUASI-STATIC SHEAR LOADING

5.1 Introduction

In this chapter, the dynamic delamination in curved unidirectional composite laminates is investigated using a simple model specimen which is formed by bonding two curved polycarbonate plates based on the premise that composite delamination mechanics can be reduced to interface failure between two materials with a weak interface [14, 15]. The model specimen has a bonded interface to mimic the interface between unidirectional composite laminates (Figure 5.1). The fracture behavior of the interface, which represents the delamination in unidirectional composite laminates, is investigated computational and experimentally. In computational study, debonding at the curved interface of bonded polycarbonate plates is modeled using dynamic (explicit) finite element analysis in conjunction with cohesive zone methods. Finite element analysis conducting in ABAQUS® with cohesive elements allows the modeling of crack initiation and growth. In experimental investigation, a unique testing fixture with a sliding platform is designed to create a pure vertical displacement to one of the arms. In addition, the use of polycarbonate material allows the use of photoelasticity to probe the interface fracture and stress state in real time. Photron Fastcam SA5 ultra high speed camera is used to capture dynamic unstable crack growth during experiments. The analysis compares favorably with experiments in terms of load displacement plots and stress contours where stable and unstable crack growths are observed for large and small pre-cracks, respectively.

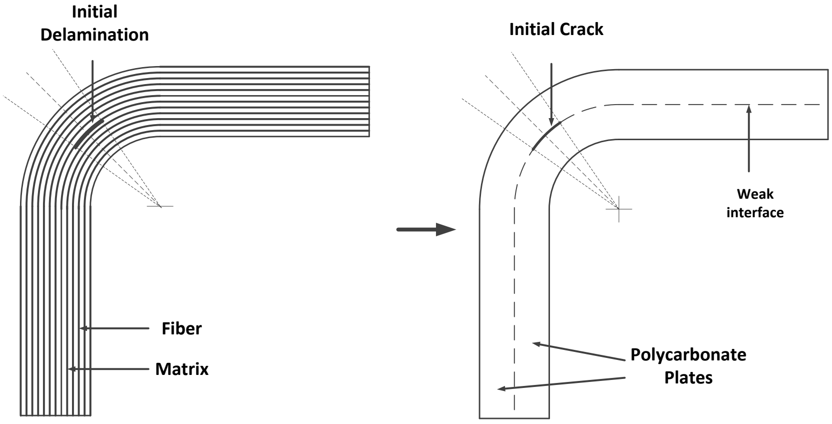

Figure 5.1 Modeling of delamination in unidirectional curved composite laminate as crack growth along curved interface of bonded polycarbonates (model specimen assumption)

5.2 Computational Framework

5.2.1 Material and Geometry

The geometry, dimensions of specimen, and boundary conditions used in finite element analysis is shown in Figure 5.2. The model specimen consisting of two curved bonded polycarbonate plates has width of 30 mm and thickness of 10 mm, with two arms of 90 mm and 60 mm in length and the inner radius at the curved region is 30 mm. The bonding between curved polycarbonate plates is modeled by cohesive interface located at the midline of the specimen. The pre-crack in length of 14 mm, 33 mm, 50mm, and 60 mm is located at the center of curved region. Table 5.1 and Table 5.2 show the bulk material and interface properties used in the finite element analysis, respectively.

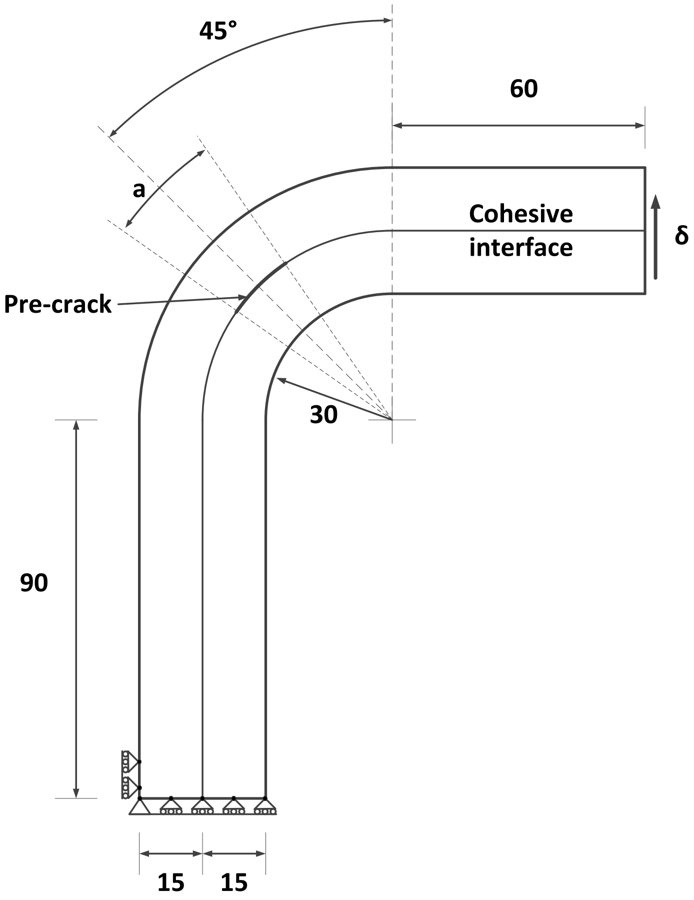

Figure 5.2 Geometry, dimensions of specimen, and boundary conditions used in finite element analysis

Table 5.1 Material Properties for Polycarbonate Plates

ρ (kg/m^3)	E (GPa)	μ (GPa)	ν
1200	2.40	0.93	0.28

Table 5.2 Interface Properties used in FEA

t_{Ic} (MPa)	t_{IIc} (MPa)	G_{Ic} (J/m^2)	G_{IIc} (J/m^2)	B-K criterion constant (η)	Penalty Stiffness (MPa)
11	22	200	600	2.25	10^8

5.2.2 Plane Stress Assumption

3-D finite element analysis for solid curved beam was conducted in order to decide whether plane stress or plane strain assumption is valid for the given geometry. Finite element analysis is conducted using ABAQUS® [28]. Figure 5.3 (a) shows the three dimensional meshed finite element model and boundary conditions. While the lower arm of the geometry is clamped, displacement input in y-direction is applied to the upper arm. Figure 5.3 (b) shows the y-displacement field for deformed body. Figure 5.4 shows the load displacement curves obtained from three dimensional model and two dimensional models using the plane stress and plane strain assumptions. It is obviously shown that plane stress assumption gives relatively closer solution to the three dimensonal model compared to plane strain assumption.

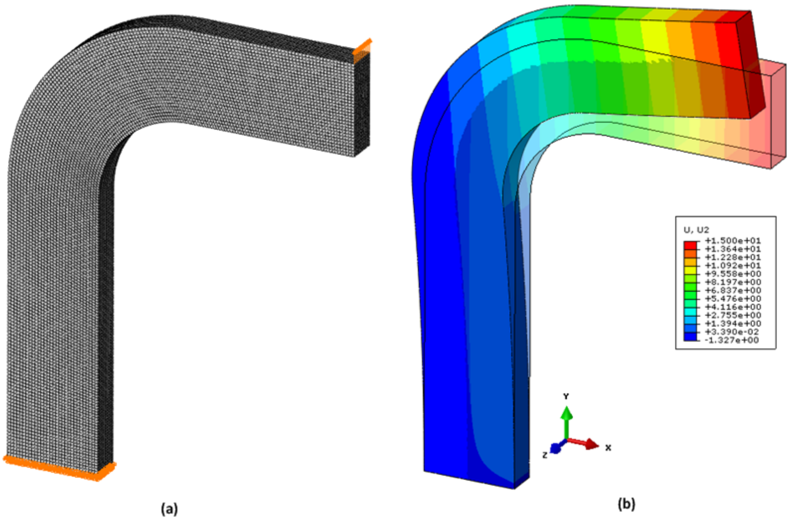

Figure 5.3 3-D finite element model: (a) geometry, mesh and boundary conditions, (b) y-displacement field on the deformed shaped.

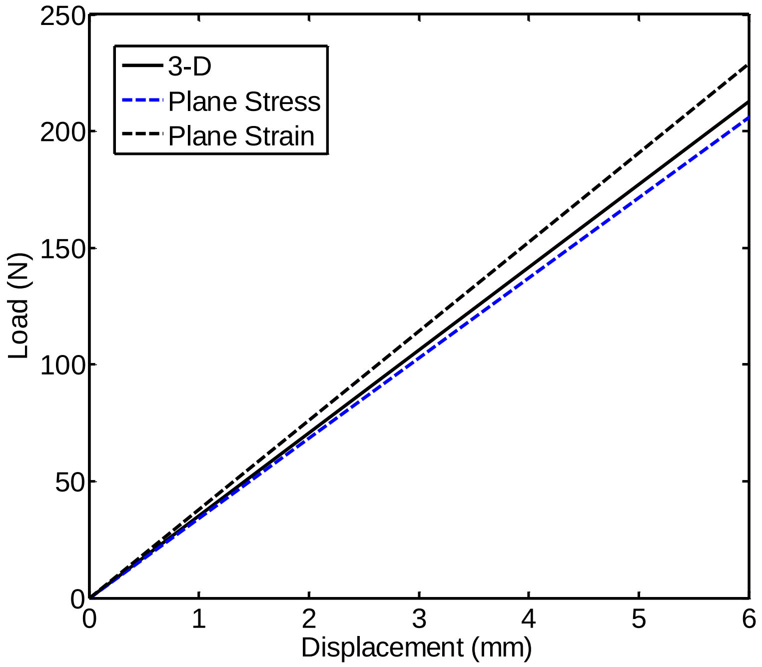

Figure 5.4 Comparison of plane strain and stress assumptions with 3-D FEA

5.2.3 Finite Element Model

The finite element model of curved polycarbonate specimen uses 2-D plane stress elements. The same FEA procedure, mesh density and convergence used in [10] were employed in this study. Finite element model consists of fine and coarse mesh regions shown as in Figure 5.5 (b). The mesh is uniform with each element a height (radial length) of 0.30 mm and a width of 0.10 mm for fine mesh area covering the field around the initial crack. The length of each cohesive element determined using a method proposed by Turon et. al [26] is also 0.10 mm for fine mesh area. On the other hand, the mesh is uniform with each element a height (radial length) of 0.30 mm and a width of 0.70 mm for coarse mesh areas which are on the far filed of initial crack. The displacement input is applied perpendicular to the upper arm (y-direction) at the rightmost nodes while the lower arm is clamped at nethermost nodes (Figure 5.5 (a)). The shape of the displacement input starts with a smooth ramp and rises to its full value of 10 mm in 0.1s; if a smooth ramp is not used; harmonic oscillations [27] in the early stages of equilibrium curve occur. The stable time value used for explicit time integration is taken as $4.00\text{x}10^{-10}$ seconds, which is half of the stable time, calculated by ABAQUS [28].

Sequential finite element analysis in ABAQUS, implicit analysis followed by explicit analysis, used by Gozluklu and Coker [10] is conducted for the sake of efficient computational analysis. The explicit simulations are carried out for the dynamic crack growth part following implicit FEA simulations for the elastic loading part just before crack initiates. The dynamic analysis is carried out using ABAQUS/Explicit and the static analysis is carried out using ABAQUS/Standard. The same finite element model and element types are used for both analyses.

The bulk material and cohesive zone properties are given in Table 5.1 and 5.2 respectively. The interface properties are fine-tuned according to failure load obtained in the experiment of 14 mm pre-cracked specimen.

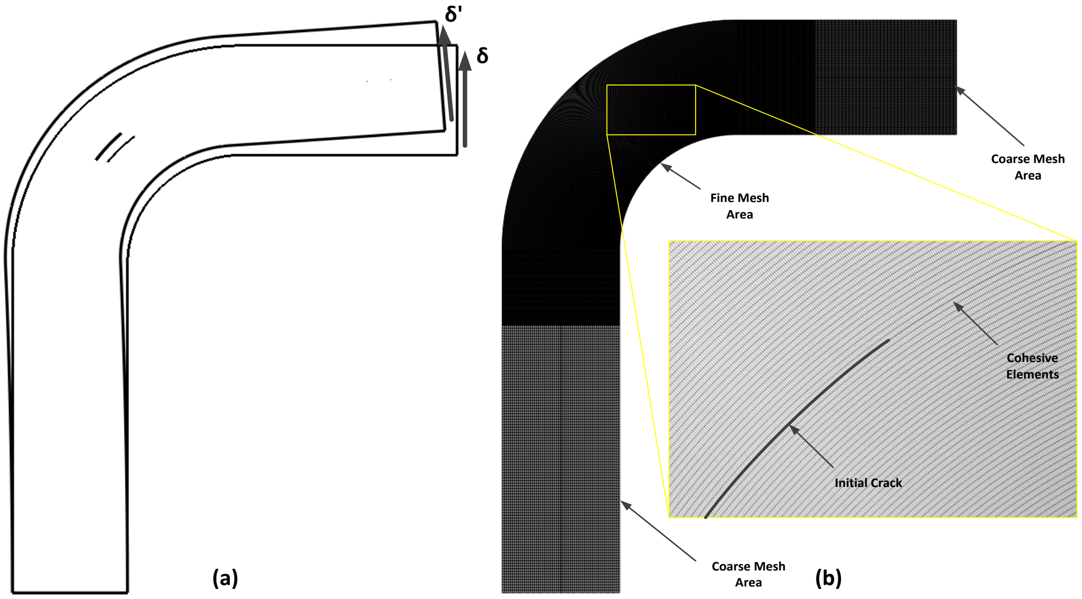

Figure 5.5 (a) Application of pure shear (V) loading in FEA, (b) Mesh used in FEA

5.3 Experimental Framework

5.3.1 Specimen Preparation

The geometry of the specimen is shown in Figure 5.6. The specimen has two arms of 100 mm in length and curved region with an inner radius of 30 mm. The specimen consists of two curved polycarbonate plates having thickness of 10 mm and width of 15 mm. Each part of the specimen is cut from 10 mm thick MAKROLON® polycarbonate plate using water jet cutter. The water jet cutting process is shown in Figure 5.7. After water jet cutting process bonding surfaces of the parts are sanded using 120 grit sand paper in order to obtain smooth bonding surface. Two curved polycarbonate plates are bonded to each other using Devcon© 33345 S-33 High Strength epoxy. The bond is cured for at least 24 hours at room temperature. During bonding process non-adhesive Teflon tape with thickness of 0.5 mm is used in order to create an initial crack at the curved region.

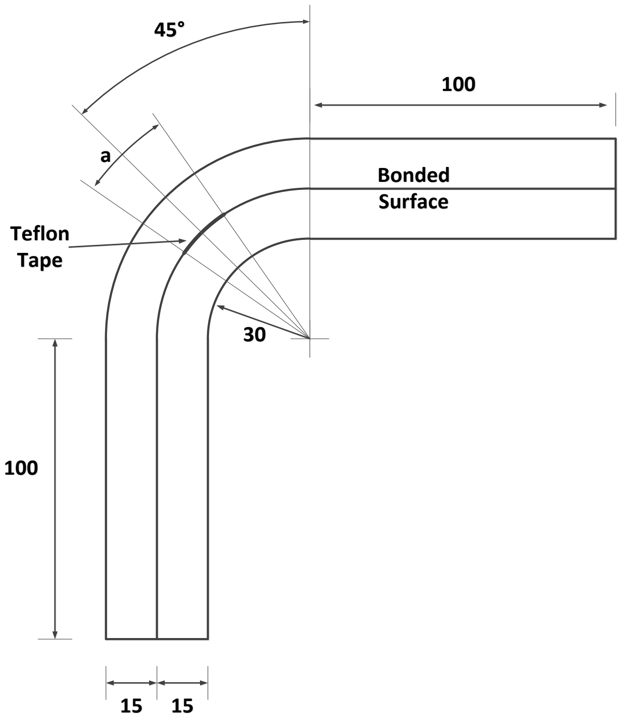

Figure 5.6 Specimen geometry (all dimensions are in mm)

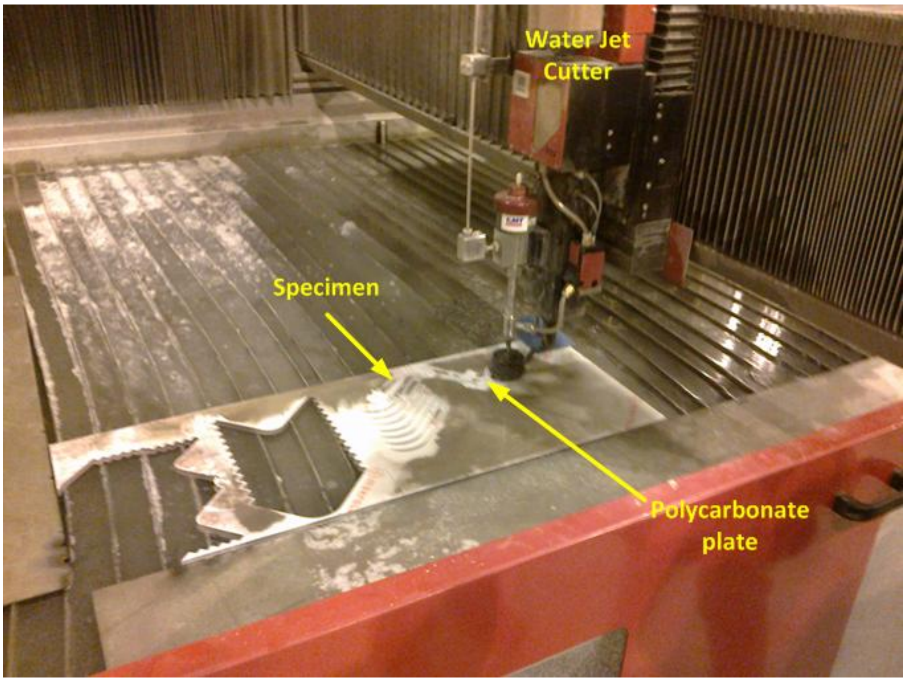

Figure 5.7 Water jet cutting process

5.3.2 Loading Procedure and Fixture Design

An overview of the experimental test setup is shown in Figure 5.8. The experiments are conducted using Shimadzu Autograph AGS-J series 10kN screw-driven tensile-compression testing machine. Testing machine is controlled remotely using a computer. All tests are performed at a cross-head speed of 3 mm/min at the room temperature while the machine load and upper fixture displacement are measured. The load is introduced perpendicular to the upper arm of the specimen using designed loading fixture. The application point of loading and the clamping distance are the same as that used in the finite element analysis shown as Figure 5.2. The major experimental challenge has been to apply the exact same boundary conditions used in the finite element analysis so that an accurate comparison can be made. In this case, a purely vertical load to the upper arm is required with no horizontal component and no moment. For this purpose, three different loading fixtures shown in Figure 5.9 were proposed to mimic the loading conditions simulated in the finite element model.

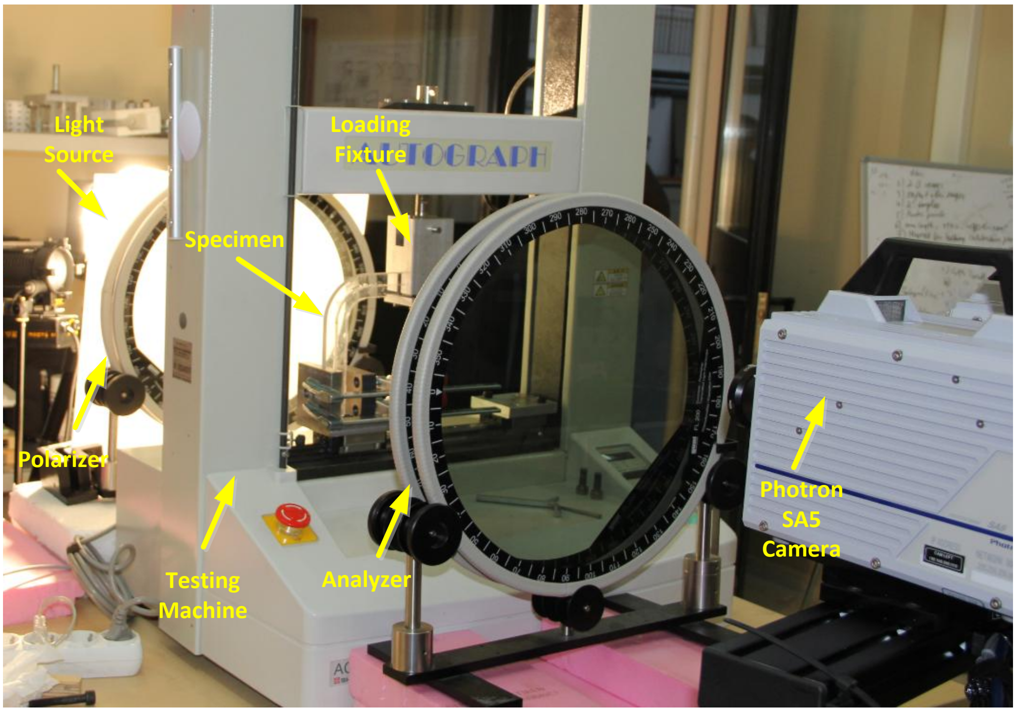

Figure 5.8 Overview of experimental setup

Fixture #1 is designed so that the lower arm of the specimen is clamped while the perpendicular loading is applied to the upper arm with a line contact. The use of simple contact at the upper arm enables moment free boundary condition at the upper arm. Fixture

#2, which is similar to the loading fixtures used in the composite experiment in the literature [4,5], is designed very similar to the first fixture, in which a pivot pin, which is free to rotate due to the roller bearings, is used for contact at the specimen arm. In these two fixtures, the loading application point changes as the arm rotates. Fixture #3 is designed so that the lower arm of the specimen is clamped on a slider platform to give a degree of freedom along the x-axis that removes the reaction force along the x-axis at the upper arm. The upper part of the fixture #3 is clamped to the specimen using bolts and the clamped part is free to rotate in order to remove reaction moment at the upper arm. This fixture applies a loading perpendicular to the upper arm of the specimens.

The load-displacement curves obtained from finite element analysis for a curved polycarbonate plate without interface are compared with that of the three fixtures in Figure 5.10. The slopes for the first two fixtures are nonlinear and lower than that for the finite element model. In addition, there are small drops in the loads for the first fixture attributed to stick-slip behavior at the contact point. Softening behavior is observed for the first two fixtures because the application point of the perpendicular loading is moving away from the original point, causing nonlinear behavior. However, for the third fixture, the stiffness is linear and follows that of the finite element model. There is no softening of the load displacement curve. Just as in the finite element model, the free movement of the platform prevents application of a horizontal force as the upper arm rotates. Thus fixture #3 gives the boundary conditions represented in the finite element model accurately, which is a perpendicular displacement applied to the upper arm.

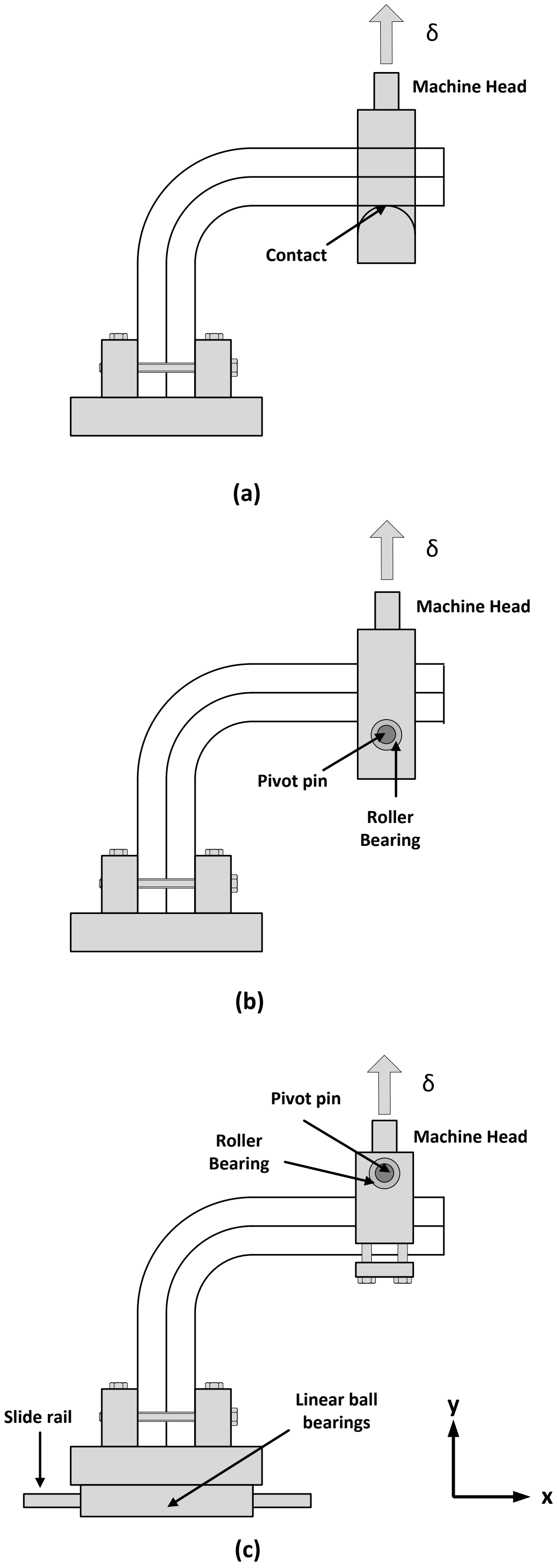

Figure 5.9 Proposed and used loading fixtures to simulate the loading perpendicular to the upper arm of the L-shaped specimens, (a) Fixture #1, (b) Fixture #2, (c) Fixture #3.

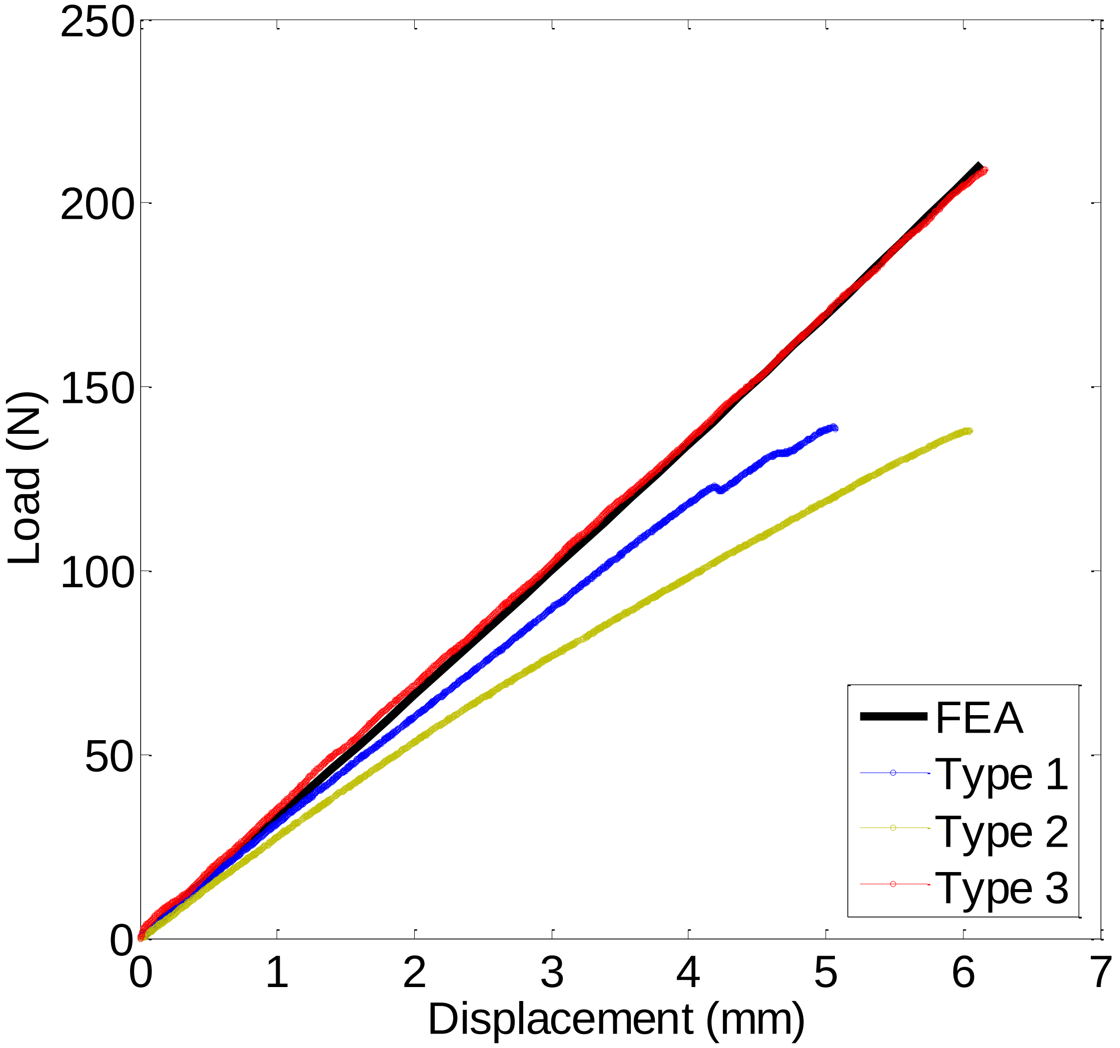

Figure 5.10 Comparison of fixtures with the finite element analysis in terms of stiffness.

5.4 Results

5.4.1 The Effect of Initial Crack Length on the Crack Growth Stability

Simulations were carried out for 14 mm, 33 mm, 50 mm, and 60 mm pre-crack lengths that were inserted on the interface at the curved region. The load displacement plots are shown in Figure 5.11 for all cases. In all cases, the initial stiffness and the maximum load decrease with increasing pre-crack length as expected. For relatively smaller pre-crack lengths, 14 mm and 33 mm, the specimen deforms linearly until 370 N and 180 N respectively, after which the crack starts propagating unstably toward the end of the arms resulting in the sudden decrease of the load. In the simulations, explicit analysis leads to large fluctuations in the load due to dynamic instability for these cases. For the relatively larger pre-crack lengths of 50 mm and 60 mm, a small decrease in the load occurs when crack initiates at 110 N and 80 N respectively. For these cases, the load continues to increase during stable crack propagation albeit with a lower stiffness.

The experiments were conducted for the same specimen geometries. The load displacement plots are shown in Figure 5.12 showing similar tendencies as the simulations for the effect of initial crack length. As before, in all cases, the stiffness and loads decrease with increasing initial crack length. For 14 mm pre-cracked specimen after an elastic increase of the load with a stiffness of 37 N/mm, a sudden decrease in load occurs at 360 N. The load instantaneously decreases to 100 N after which it monotonically increases with a lower stiffness of 19 N/mm. Similarly for 33 mm pre-cracked specimen after an elastic increase of the load with a stiffness of 35 N/mm, a sudden decrease in load occurs at 220 N. The load instantaneously decreases to 70 N after which it monotonically increases with a lower stiffness of 17 N/mm. For the 50 mm pre-cracked specimen, the load increases elastically with a stiffness of 30 N/mm until crack propagation starts at 100 N where a slight decrease in load is recorded. After this point the load continues to increase at a reduced stiffness of 22 N/mm with intermittent drops in load which represent discrete stable crack growth. Similarly, for the 60 mm pre-cracked specimen, the load increases elastically with a stiffness of 26 N/mm, until discrete intermittent crack growth starts at 65 N with corresponding decreases in load. After this point the load continues to increase at a reduced stiffness of 21 N/mm with intermittent drops in load which represent discrete stable crack growth.

The load displacement behavior is found to be qualitatively and quantitatively similar between the simulations and experiments. Two discernible features can be observed from the load-displacement results. For the cases with small pre-cracks ($a<40$mm), a sudden drop in the load occurs in which the crack propagates to its limits in the arms after which the load increases with the reduced stiffness. For the cases with large pre-cracks ($a>40$mm), a stable crack growth occurs with intermittent change in crack length.

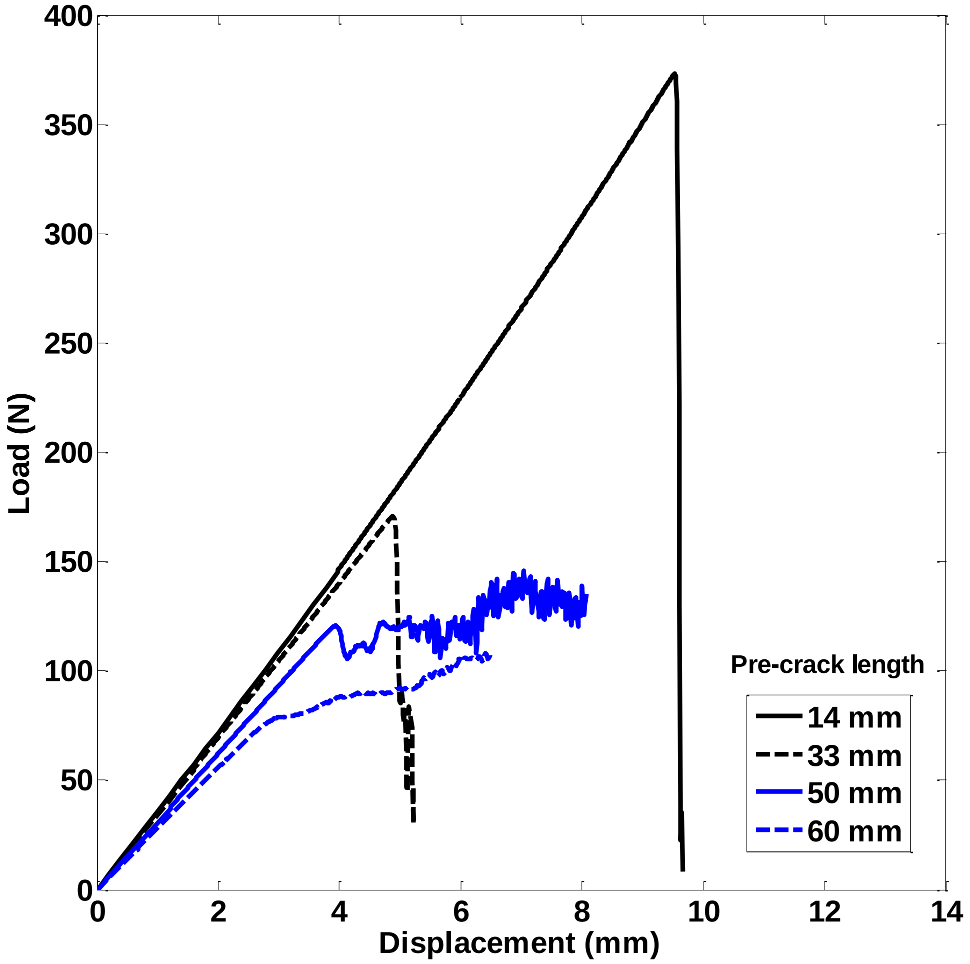

Figure 5.11 Load-displacement plots obtained from finite element analysis of 14 mm, 33 mm, 50 mm, and 60mm pre-cracked L-shaped specimens.

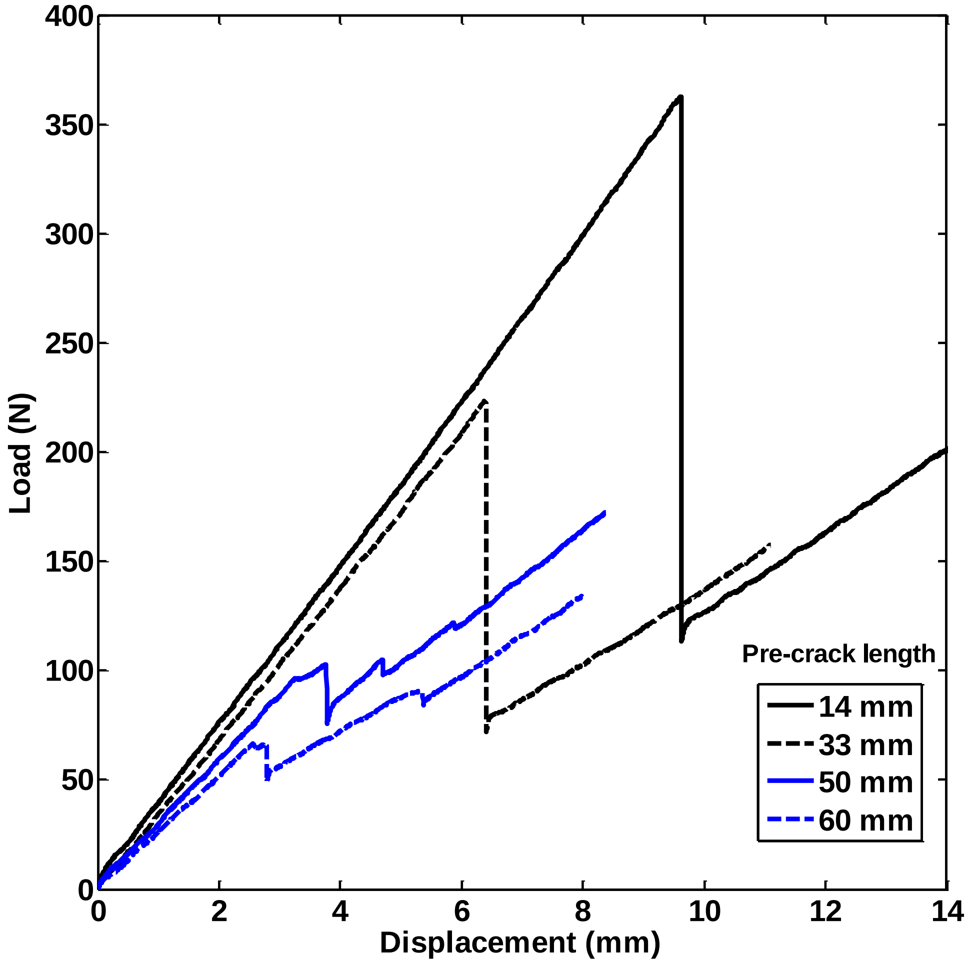

Figure 5.12 Load-displacement plots obtained from experiments of 14 mm, 33 mm, 50 mm and 60 mm pre-cracked L-shaped specimens.

Compliance and energy release rate values can be calculated for different crack lengths from the experimental load-displacement curves in order to analyze stability behavior depending on the initial crack length. The compliance for different crack lengths is calculated from the initial slope of the load-displacement curve by,

$$C = \frac{\delta}{P} \tag{5.1}$$

For displacement loading case, the energy release rate is calculated from the change in compliance with crack length by

$$G = \frac{1}{2t} \cdot \frac{\Delta C}{\Delta a} \cdot \left(\frac{\delta}{C}\right)^2 \tag{5.2}$$

The change in compliance and energy release rate with respect to crack length is shown in Figure 5.13 (a) and (b), respectively. As can be seen in Figure 5.13 (b), below a crack length of around 50 mm, the slope of the energy release rate is positive ($\partial G/\partial a>0$) which implies unstable crack growth and is negative ($\partial G/\partial a<0$) for larger crack lengths, which implies stable crack growth. This is consistent with the experimental and computational results and gives a reasonable explanation to the effect of initial crack length on the crack growth stability.

5.4.2 Stable Crack Growth

Figure 5.14 illustrates the load displacement curves obtained from finite element analysis (blue line) and experiment (black line), maximum shear stress contours obtained from finite element analysis, and isochromatic stress fringe pattern obtained from photoelasticity experiments. These results were obtained for the specimen with a 60 mm initial crack. The load displacement curves obtained from finite element analysis and experiments are in good agreement in terms of stiffness and maximum failure load. In addition the stress fields are in good agreement between the simulations and the experiments. As shown in the load displacement curve, small load drops with a stiffness change is observed for quasi-static stable crack growth in both finite element analysis and the experiment. The each small load drop corresponds to a small change in crack position.

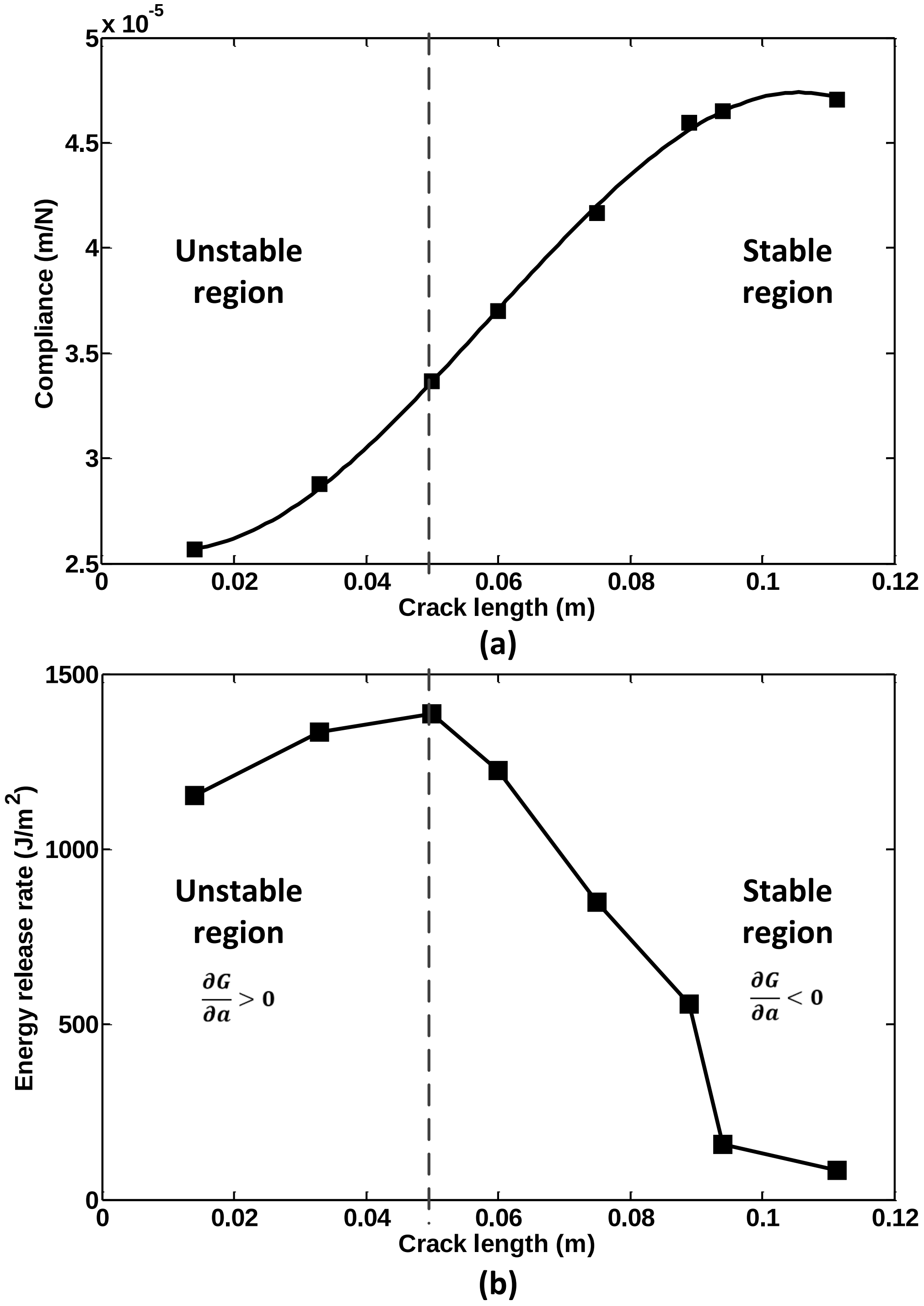

Figure 5.13 Change in (a) compliance and (b) energy release rate with respect to pre-crack lengths (Energy release rate is computed for δ=0.010 m)

5.4.3 Unstable Crack Growth

Figure 5.15 shows the load displacement curves obtained from finite element analysis (blue line) and experiment (black line), maximum shear stress contours obtained from finite element analysis, and isochromatic stress fringe pattern obtained from photoelasticity experiments. These results are obtained for the specimen with a 14 mm initial crack. The load displacement curves obtained from finite element analysis and experiments are in good agreement in terms of stiffness and maximum failure load. In addition the stress fields are in good agreement between the simulations and the experiments. As shown in the load displacement curve, sudden large load drop is observed for dynamic unstable crack growth in both finite element analysis and the experiment. Crack dynamically travels towards arms of the specimen during this sudden load drop. The nature of the stress fringe patterns reveal opening mode crack growth in this geometry under perpendicular loading.

5.4.4 Crack Propagation Speed

The crack propagation is captured by Photron Fastcam ultra high speed system for unstable dynamic crack growth of 14 mm pre-cracked specimen. Figure 5.16 shows isochromatic fringe pattern obtained from photoelasticity experiment during crack propagation. The crack tip positions along the curved interface are marked by arrows. It is shown that right crack tip reaches at the end of the curved region within a very short time interval of 60 μs.

The right crack tip speed is calculated by analyzing pictures captured by high speed camera are using image processing technique and the crack tip position is obtained for each frame. The crack tip speed is calculated numerically with central differentiation method using crack tip positions. The crack tip speed as a function of time is shown in Figure 5.17. It shown that crack sub-sonically propagates and crack propagation speed is in the order of the shear wave speed. This result is very similar to the result obtained for crack propagation speed of curved composite laminates in Chapter 4.

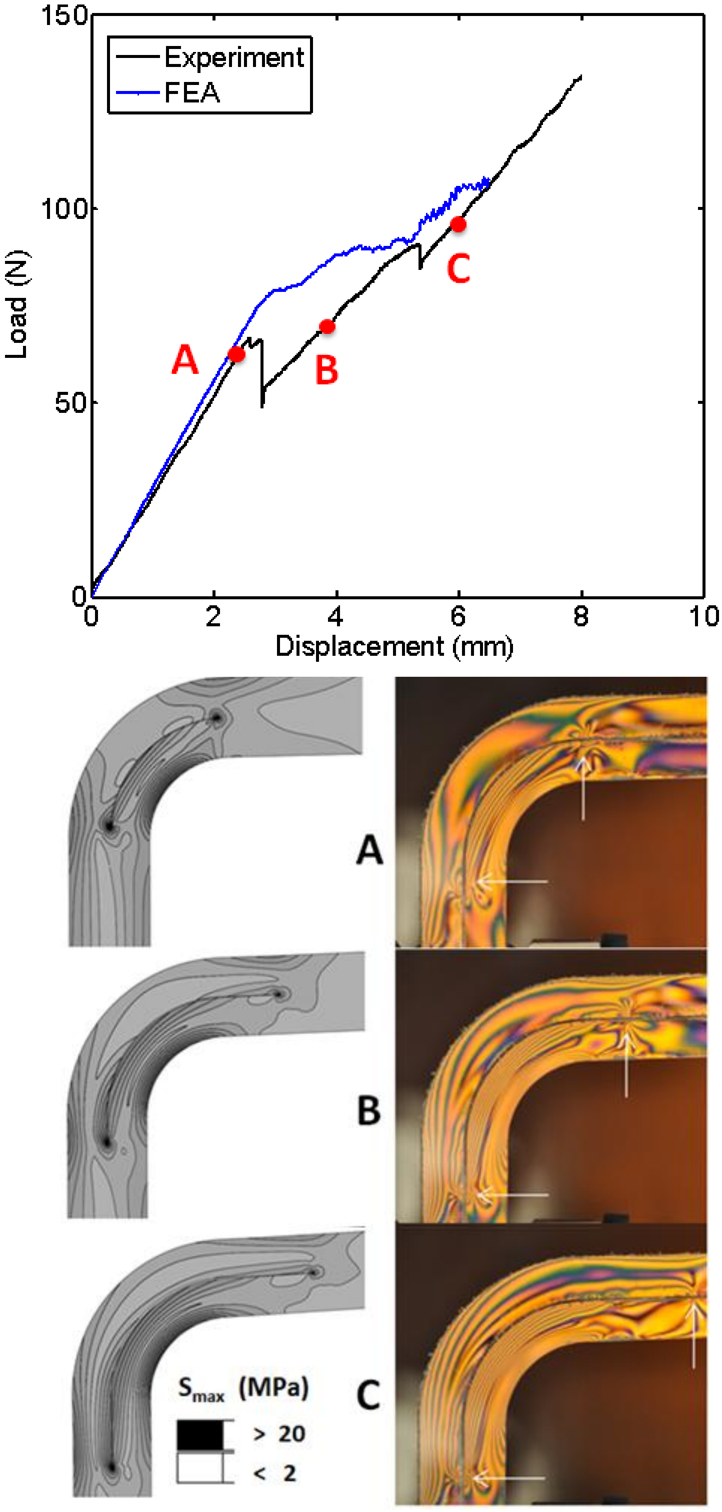

Figure 5.14 Load-displacement curve, maximum shear stress contours obtained from FEA and photoelastic experiments for stable crack growth in 60 mm pre-cracked specimen

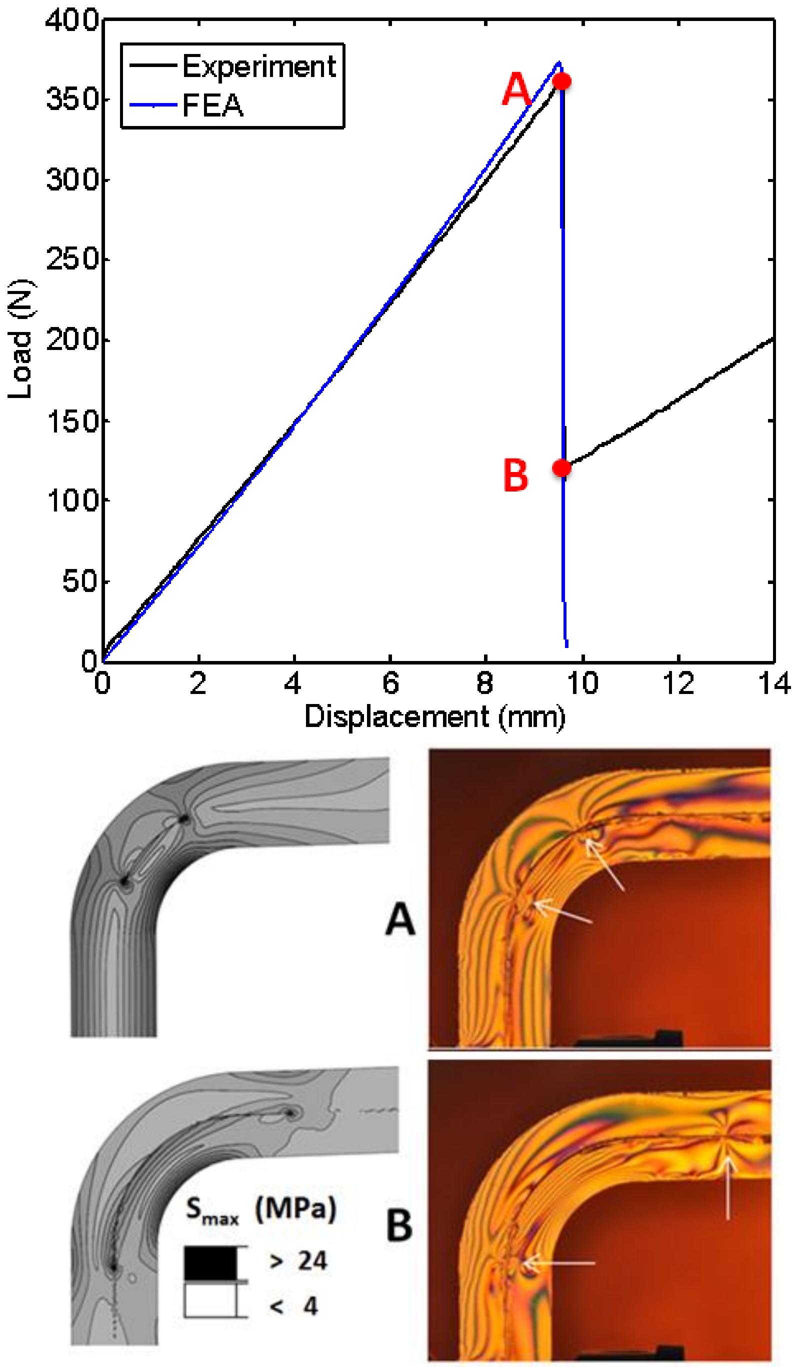

Figure 5.15 Load-displacement curve, maximum shear stress contours obtained from FEA and photoelastic experiments for unstable crack growth in 14 mm pre-cracked specimen

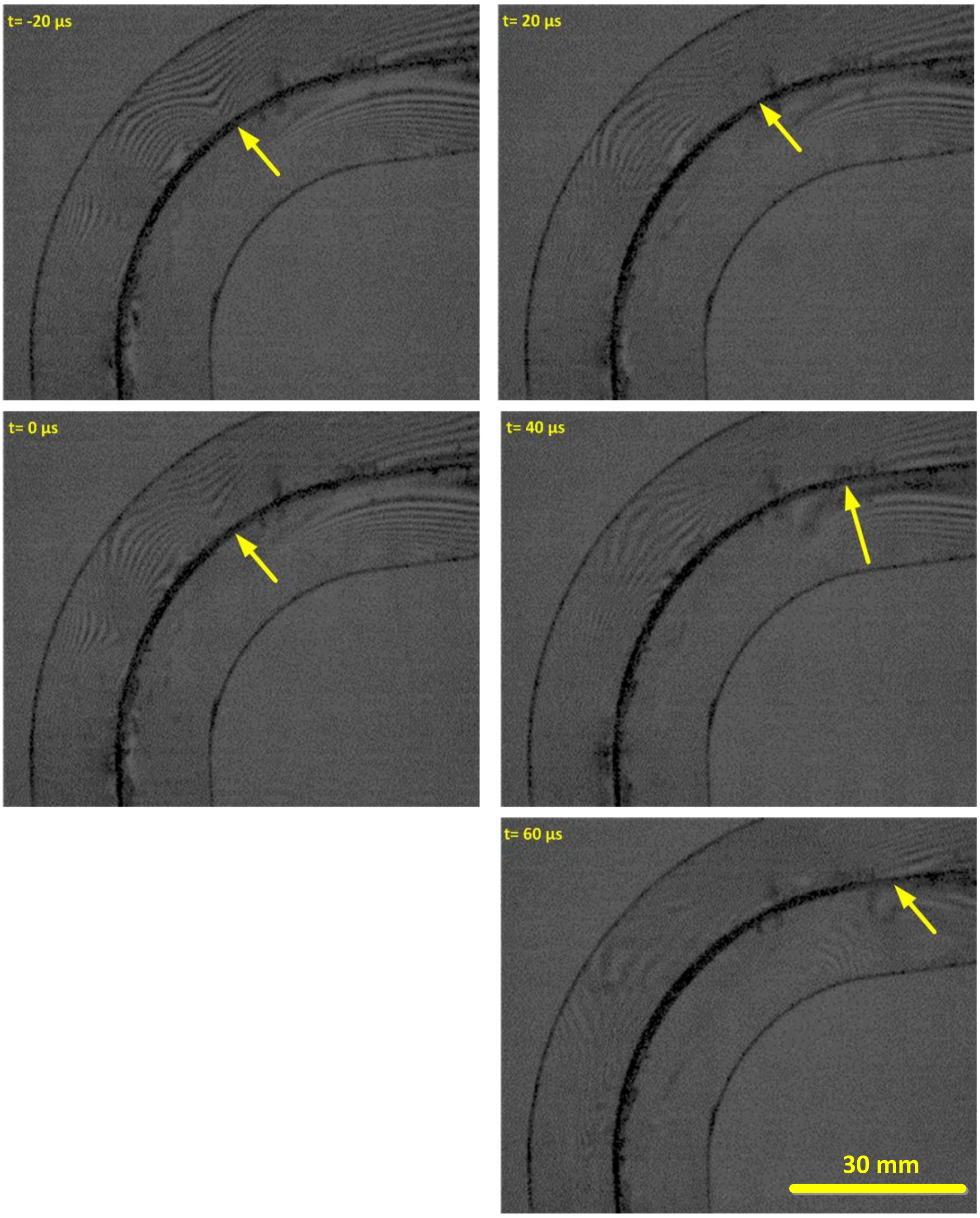

Figure 5.16 Isochromatic fringe pattern pictures captured by Photron Fastcam SA5 high speed camera during dynamic crack growth in 14 mm pre-cracked specimen

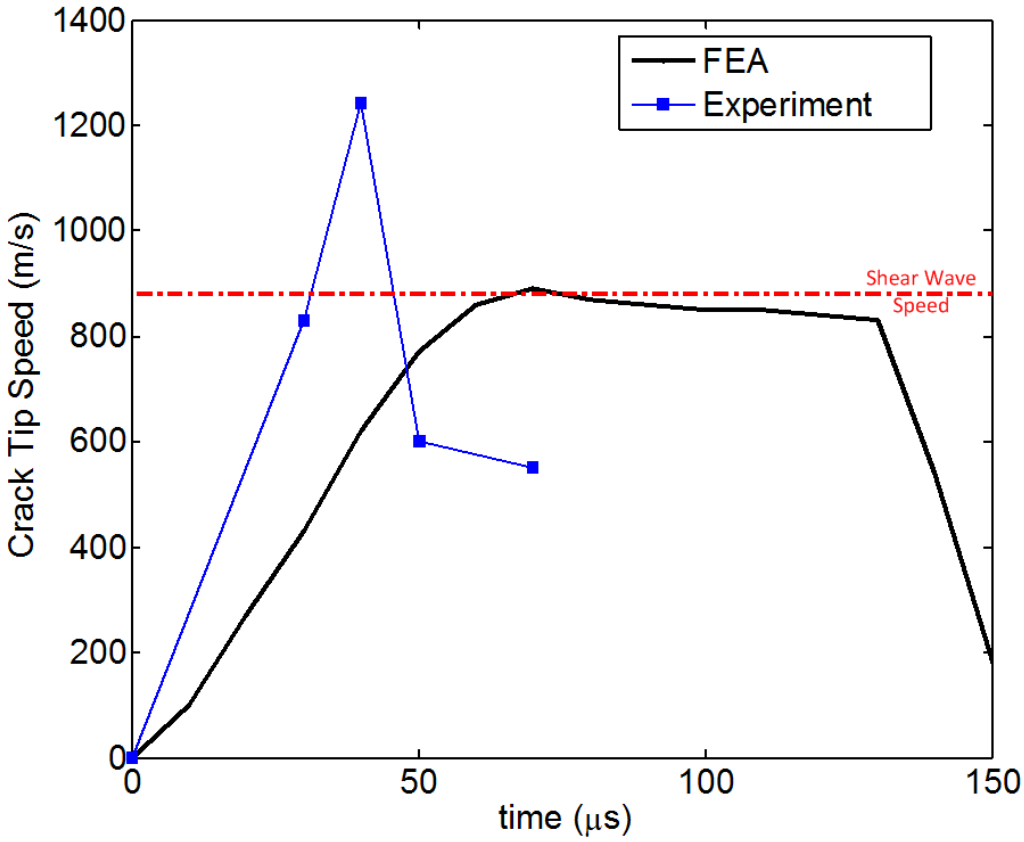

Figure 5.17 Crack propagation speed obtained from FEA (black solid line) and experiments (red stars)/ Blue horizontal line shows the shear wave speed.

5.5 Conclusions

Experiments and computational simulations were carried out for bonded curved polycarbonate plate subjected to shear loading. 14 mm, 33 mm, 50 mm, and 60 mm pre-cracks were inserted at the interface of the curved region in order to investigate the effect of pre-crack length on the stability of the crack growth. Experimental debonding results compare favorably with finite element analysis using cohesive elements. The following conclusions were reached:

- A testing fixture was designed with a sliding platform that allows for shear loading consistent with the finite element displacement boundary condition.
- Cohesive zone method was successful in modeling stable/unstable crack growth observed in the experiments in terms of stress contours and crack propagation.
- In both simulations and experiments unstable dynamic crack growth was observed for relatively small crack (14 mm and 33 mm) pre-cracked specimens, whereas stable

quasi-static crack growth was observed for large (50 mm and 60 mm) pre-cracked specimens.

- Energy release rate calculations show that stable crack growth occurs for initial crack larger than 50 mm and unstable crack growth occurs for smaller initial cracks.
- Crack propagation speed can reach the shear wave speed for unstable dynamic crack growth.
- Similar stable and unstable crack growth regimes are observed in unidirectional curved composite laminates.

CHAPTER 6

CONCLUSION

6.1 Summary and Conclusions

In this study, crack growth along curved weak interfaces is investigated experimentally and computationally. First, delamination of curved composite laminates subjected to axial load is studied computationally. Delamination in curved laminates is modeled using explicit finite element analysis in conjunction with cohesive zone method. It is observed that delamination is highly dynamic and that as the initial crack grows, the crack tip speed reaches the Rayleigh wave speed of the composite material with increasing laminate thickness and decreasing initial crack length. A second observation is that a secondary delamination in the arm region nucleates depending on the initial crack length and laminate thickness. Second, delamination of curved composite laminates subjected to shear loading is studied experimentally. Dynamic delamination growth is captured using high speed camera. It is observed that crack growth speed reachs the shear wave speed and an increase in the length of initial crack changes the crack growth from unstable to stable. Finally, crack growth along curved interface in polycarbonate beams subjected to shear loading is studied experimentally and computationally. In experiments, the full-field technique of photoelasticity is used in order to visualize isochromatic fringe pattern around the crack tip. In computational study, debonding at the curved interface is modeled using dynamic (explicit) finite element analysis in conjunction with cohesive zone methods. Stable and unstable crack growth regimes, depending on the initial crack length, are identified in agreement with energy release rate calculations. It is also observed that crack propagation speed can reach the shear wave speed.

Although each section has its own conclusions, the followings are overall conclusions covering whole of the study:

- Dynamic crack growth in curved composite laminates occurs under combined mode I and Mode II for axial loading, whereas it is under mode I for shear loading.
- All crack growth in curved composite laminates under axial loading is found to be unstable regardless of the initial crack length and thickness, however crack growth along curved interfaces in composite laminates and polycarbonate plates under shear loading can be stable depending on the initial crack length.
- Considering crack growth along curved interfaces in composite laminates and polycarbonate plates under shear loading, it is unstable dynamic crack growth for a specimen with a small initial crack, whereas it is stable quasi-static crack growth for a specimen with a large initial crack.
- Two distinct failure mechanisms were observed for curved composite laminates under axial loading. The first failure mechanism is the growth of the initial crack.

The second failure mode is the formation and propagation of a secondary crack near the center of the clamped arm.

- Crack propagation speed for unstable dynamic crack growth were found to be in the order of the shear wave speed independent of loading for both curved composite laminates and curved polycarbonate.

6.2 Future Work

The following items can be considered as a previous work:

- The experimental study can be conducted to observe the same two distinct failure mechanism discussed in Chapter 3. The effect of initial crack length and thickness on the failure mechanism can be showed experimentally for unidirectional curved composite laminates under quasi-static axial loading.
- The finite element analyses can be conducted for different cohesive zone model such as Xu and Needleman cohesive zone model.
- The effect of thickness on the crack growth stability and speed can be studied using assumption of model material, material with a weak interface.
- The same study conducted in Chapter 5 can be repeated for quasi-static axial loading.

REFERENCES

[1] Vanttinen, A., Strength prediction of composite rib foot corner, Helsinki University of Technology, 2008.

[2] Lekhnitskii, S.G., Anisotropic Plates. New York, NY: Gordon and Breach Publishers, 1968, 95–101.

[3] Martin, R.H. and Jackson, W.C., Damage prediction in cross-plied curved composite laminates, NASA Technical Memorandum 104089, USAAVSCOM Technical Report 91-B-009, 1991.

[4] Martin, R.H., Delamination failure in a unidirectional curved composite laminate, Composite Material Testing and Design 1992;10:365–83.

[5] Wimmer, G., Kitzmüller, W., Pinter, G., Wettermann, T., Pettermann, H.E., Computational and experimental investigation of delamination in L-shaped laminated composite components, Engineering Fracture Mechanics, 2009;76:2810–20.

[6] Wimmer, G. and Pettermann, H.E., A semi-analytical model for the simulation of delamination in laminated composites, Composite Science and Technology 2008; 68:2332–9.

[7] Wimmer, G., Schuecker, C., Pettermann, H.E., Numerical simulation of delamination in laminated composite components – a combination of a strength criterion and fracture mechanics, Composites Part B 2009;40:158–65.

[8] Sridharan, S., Delamination behaviour of composites, CRC Press LLC, 2008.

[9] Bolotin,V.V., Delaminations in composite structures: its origin, buckling, growth and stability, Composites: Part B 1996; 27B: 129-145.

[10] Gozluklu, B. and Coker, D., Modeling of the dynamic delamination of L-shaped unidirectional laminated composites, Composite Structures 2012; 94: 1430–1442.

[11] Hao, W., Ge, D., Ma, Y., Yao, X., and Shi, Y., Experimental investigation on deformation and strength of carbon/epoxy laminated curved beams, Polymer Testing, 2012; 31: 520-526.

[12] Lu, T.J., Xia, Z.C., Hutchinson, J.W., Delamination of beams under transverse shear and bending, Materials Science and Engineering 1994; A188: 103-112

[13] Feih, S., Shercliff, H.R., Composite failure prediction of single-L joint structures under bending, Composites: Part A 2005; 36: 381-395.

[14] Coker, D. and Rosakis, A.J., Experimental observations of intersonic crack growth in asymmetrically loaded unidirectional composite plates, Philosophical Magazine A 2011; 81-3: 571-595

[15] Rosakis, A.J., Samudrala, O., Coker, D., Cracks faster than the shear wave speed, Science 1999; 284:1337-1340.

[16] Griffith, A.A., The Phenomena of rupture and flow in solids, Philosophical Transactions of the Royal Society of London 1921; 221: 163-198

[17] Schreurs, P.J.G., Fracture Mechanics Lecture Notes, Eindhoven University of Technology, Department of Mechanical Engineering, September 6, 2012.

[18] Irwin, G.R. and Kies, J.A., Critical energy rate analysis of fracture, Welding Journal 1954; 33: 193-198.

[19] Barenblatt, G.I., Equilibrium cracks formed on a brittle fracture, Advanced Applied Mechanics 1959:127-1, 47-50.

[20] Barenblatt, G.I., Mathematical theory of equilibrium cracks in brittle failure, Advanced Applied Mechanics 1962:7.

[21] Dugdale, D.S., Yielding of steel sheets containing slits, Journal of the Mechanics and Physics of Solids 1960; 8:100–4.

[22] Ye, L., Role of matrix resin in delamination onset and growth in composite laminates, Composite Science and Technology 1988; 33:257–77.

[23] Benzeggagh, M.L. and Kenane, M., Measurement of mixed-mode delamination fracture toughness of unidirectional glass/epoxy composites with mixed mode bending apparatus, Composite Science and Technology 1996;56:439–49.

[24] Geubelle, P.H. and Baylor, J., Impact-induced delamination of laminated composites: a 2D simulation, Composites Part B 1999;29(5):589–602.

[25] Dally, J.W. and. Riley, W.F, Experimental stress analysis, 3rd edition, McGraw-Hill Inc., 1991.

[26] Turon, A., Davila, C.G., Camanho, P.P., Costa, J., An Engineering Solution for Mesh Size Effects in the Simulation of Delamination Using Cohesive Zone Models, Engineering Fracture Mechanics 2007;74:1665–1682.

[27] Pinho, S.T., Iannucci, L., Robinson, P., Formulation and implementation of decohesion elements in an explicit finite element code, Composites Part A 2006;37:778–89.

[28] ABAQUS User Manual, Pawtucket (RI); Hibbitt, Karlsson& Sorensen Inc., 2009.